Technische Universität München

Fakultät für Chemie

Propane dehydrogenation on highly active and selective Ga/BEA and ethanol conversion to butadiene on zincosilicate BEA

Lingli Ni

Vollständiger Abdruck der von der Fakultät für Chemie der Technischen Universität München zur Erlangung des akademischen Grades eines

Doktors der Naturwissenschaften (Dr. rer. nat.)

genehmigten Dissertation.

Vorsitzender: Prof. Dr.-Ing. Kai-Olaf M. Hinrichsen

Prüfer der Dissertation: 1. Prof. Dr. Johannes A. Lercher

2. Prof. Dr. Roland A. Fischer

Die Dissertation wurde am 18.01.2022 bei der Technischen Universität München eingereicht und durch die Fakultät für Chemie am 24.02.2022 angenommen.

It is the most distant course that comes nearest to thyself,

and that training is the most intricate which leads to the utter simplicity of a tune.

Rabindranath Tagore, Gitanjali

Acknowledgments

It has been a long, tough but treasurable time to go through the whole doctoral study. I am very lucky to have so many people who helped and supported me during the time, without whom I would not have been here.

First of all, I would like to thank Prof. Dr. Johannes A. Lercher for offering me the valuable opportunity to pursue my doctorate research in this group. Special thanks for his priceless guidance, encouragement, inspiration, and valuable discussions. When I got lost in the difficulties, he always pointed a way out of the chaos and dragged me back to the right track. I am astonished by his passion for science, rigorous attitude to work, expertise in research and it inspires me in both my research and personal life.

I would like to express my earnest gratitude to the Chinese Scholarship Council (CSC), for its consistent financial support in living expenses during the past four years.

I furthermore would like to show my sincere appreciation to my supervisors, Dr. Ricardo Bermejo De Val and Dr. Yue Liu. Doing research is always dealing with tough problems. I have gained a lot from the fruitful and helpful discussions with them and I appreciated their patience, understanding, and support, which have helped me a lot throughout the whole study.

I am also grateful to all former and current senior scientists in TC II, Apl. Prof. Dr. Andreas Jentys, Dr. Hui Shi, Dr. Eszter Baráth, Dr. Maricruz Sanchez-Sanchez, Dr. Erika Ember, Dr. Rachit Khare, Dr. Ruixue Zhao. Thank all of you for your input in science as well as in consultation. In particular, Dr. Hui Shi for invaluable discussions to help me go over the threshold in the middle of my study. Dr. Rachit Khare for the revisions of my manuscript and dissertation. Dr. Ruixue Zhao for helping me with the lab instruments and helpful discussions.

I would like to thank all the staff members at TC II, Steffi Seibold, Bettina Federmann, Kateryna Kryvko, Andreas Marx for their tremendous technical and administrative support during the daily work time; and Martin Neukamm, Muhammad Iqbal, and Franz-Xaver Hecht for their help on the measurements of my samples and reparation of my setup.

I would also like to thank my students Jinwei Wu, Omar Mohammad and Atidzhe Syunetchieva and all current and former colleagues at TC II. Especially thanks to Dr. Manuel Wagenhofer, Dr. Wanqiu Luo, Ferdinand Vogelgsang for their help on the rebuild of my setup at the startup; and Dr. Guanhua Cheng, Lei Tao, Dr. Xi Chen, Martina Aigner, Dr. Iris Kaming Yu, Fuli Deng, Dr. Larisha Yanira Cisneros Reyes, Verena Höpfl, Niklas Pfriem, Dr. Wei Zhang, Dr. Yong

Wang for their encouragements and help in both work and life; and Dr. Yuanshuai Liu, Dr. Jie Zhang, Dr. Yang Zhang, Hongwen Chen, Dr. Takaaki Ikuno, Dr. Martin Baumgärtl, Teresa Schachtl, Laura Löbbert, Dr. Madita Einemann, Insu Lee, Lara Milakovic, Roland Weindl, Alexander Wellmann, Jakub Pazdera, Mirjam Wenig, Fhillip Fischer, Amen Shahpal, Simon Krebs, Lennart Wahl, Christoph Gross, Florian Zahn, Dr. Andreas Ehrmaier, Dr. Felix M. Kirchberger, Dr. Daniel Melzer, Dr. Manuel Weber-Stockbauer and Dr. Karen Resende for all their help and supports in daily work in the CRC.

At last, I would like to express my deepest gratitude to my best friends, my families, my boyfriend, and his families who went with me through the ups and downs during the time. They bring me so much joy in life and give me the driving force to move forward. I am grateful for their unconditional understanding, encouragement, and support.

Lingli Ni

December 2021

Abstract

Zincosilicate BEA supported catalysts were prepared and used on propane dehydrogenation and ethanol conversion to 1,3-butadiene. Ga/BEA was highly active and selective in propane dehydrogenation. The rate determining step was found to be shifted as a function of propane pressure and a kinetic model of the catalytic cycle was established. The reaction pathway of ethanol conversion to 1,3-butadiene was demonstrated to be an Aldol condensation pathway on Zn-BEA and 1,3-butadiene productivity was significantly improved with the addition of Y on Zn-BEA.

Zusammenfassung

Katalysatoren mit Zinkosilikat-BEA als Träger wurden hergestellt und für die Propandehydrierung und die Umwandlung von Ethanol in 1,3-Butadien verwendet. Ga/BEA war bei der Dehydrierung von Propan hochaktiv und selektiv. Es wurde festgestellt, dass der geschwindigkeitsbestimmende Schritt in Abhängigkeit vom Propandruck verschoben ist, und es konnte ein kinetisches Modell des katalytischen Zyklus erstellt werden. Der Reaktionsweg der Ethanolumwandlung in 1,3-Butadien erwies sich als Aldolkondensationsweg auf Zn-BEA, und die Butadienproduktivität wurde durch die Zugabe von Y auf Zn-BEA erheblich verbessert.

Abbreviations

BEA	Zeolite in BEA topology
MFI	Zeolite in MFI topology
mr	Member ring
EX	Extra-framework
IR	Infrared spectroscopy
EXAFS	Extended X-ray-absorption fine-structure
BAS	Brønsted acid site
TPD	Temperature program desorption
LAS	Lewis acid site
SiOH	silanol group
PDH	Propane dehydrogenation
AcH	Acetaldehyde
1,3-BD	1,3-Butadiene
DEE	Diethyl ether
DRIFTS	Diffuse reflectance infrared Fourier transform spectroscopy
TPSR	Temperature-programmed surface reaction
MPVO	Meerwein-Ponndorf-Verley-Oppenauer
XRD	X-ray diffraction analysis
BET	Brunauer, Emmett and Teller
HS	Hydrothermal synthesis
TEAOH	Tetraethylammonium hydroxide
TPAOH	Tetrapropylammonium hydroxide
wt.%	Weight percentage %
Py-LAS	Pyridine interacting with Lewis acid site
PyH^+	Pyridinium ion

Py-H	H-bonded pyridine
Py-B/LAS	Pyridine interacting with both Brønsted and Lewis acid site
WHSV	Weight hourly space velocity
TOS	Time on stream
GC	Gas chromatography
FID	Flame ionization detector
K_a^0	Adsorption constant
k_1	Reaction rate constant of the first C-H bond cleavage
k_4	Reaction rate constant of H_2 desorption
N	Number of active sites
r	Reaction rate
KIE	Kinetic isotope effect
RDS	Rate determining step
θ_i	Coverage of sites i
TOF	Turnover frequency
E_a	Activation energy

Table of Contents

Chapter 1

1. General introduction

1.1 Zeolite

1.1.1 Composition and structure of zeolites

Zeolites are inorganic microporous crystalline materials, composed of TO_4 tetrahedra with O atoms linked to the neighboring T-atoms, and form well-defined channels and cavities of molecular dimensions (Figure 1.1). Traditionally, silicon and aluminum are used as the T-atoms (as called aluminosilicates for these zeolites), whereas, other elements, such as Ti, Ga, Zn, Fe, B, P, and transition elements, etc. have also been incorporated into the zeolite framework.[1]

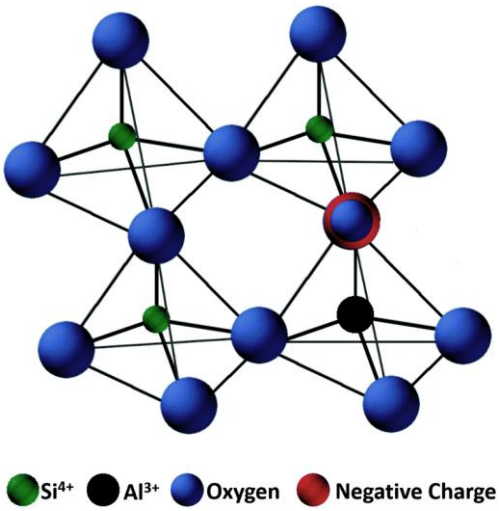

Figure 1.1 Idealized structure of zeolite framework of tetrahedral $[SiO_4]^{4-}$ with a substitution of Si by Al generating a negative charge. Adapted with permission from ref. [2]. Copyright (2002) Elsevier.

With different chemical compositions and synthesis methods, zeolites have a variety of topologies and features. For example, the channel systems may run with one, two, or three directions, leading to one-, two-, or three-dimensional pore structures, respectively depending on the interconnection and spatial disposition of the zeolite structure.[3] There are currently 259 framework structures that have been listed according to the Structure Commission of the International Zeolite Association.[4] The different topologies result in different pore dimensions, pore sizes, cages, pockets, and other structural features. According to the structure topology, zeolites can be classified based on framework type codes, such as BEA, MFI, MOR, CHA, and so on (Figure 1.2). The number of T-atoms forming the largest opening giving access to the channels or cages of zeolite structure can be 8, 10, 12, and more than 12, therefore zeolites are also referred to as small (8 member rings, mr), medium (10 mr), large (12 mr), and extra-large (>12 mr) pore zeolites.[3]

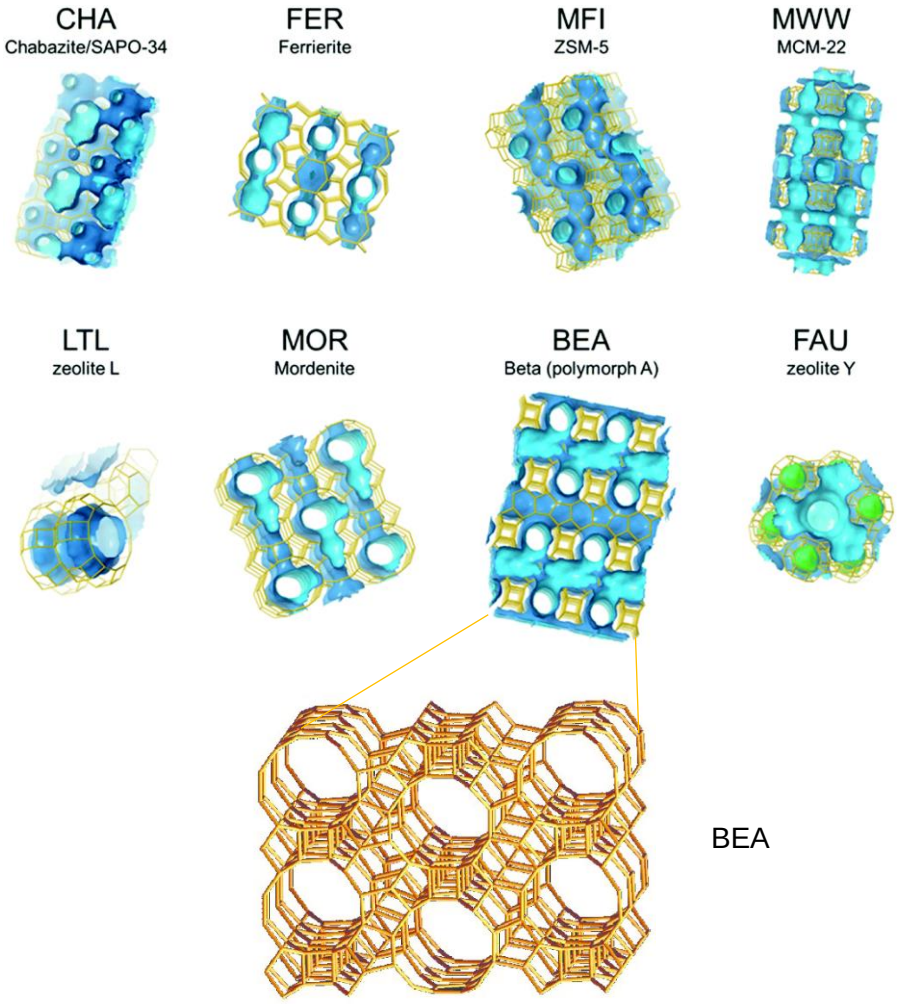

Figure 1.2 Typical zeolite structure with different topologies. Adapted with permission from ref. [3]. Copyright (2021) Royal Society of Chemistry.

Due to the high thermal stability, well-determined topology, high microporosity, high internal surface area, and notable adsorption and shape-selective properties, zeolites are among the most critical materials for various industrial applications including catalysis, ion exchange, gas separation, and so on.[5] In the particular case of heterogeneous catalysis, which has been the driving force for a rational approach to zeolite synthesis, the study focuses on the discovery of new structures and alternatives for zeolite materials. Among various zeolites, zeolite BEA was first reported by Mobil Oil in 1967.[6] Its structure was determined in 1988 [7, 8] and it was the first example of a three-dimensional and large-pore zeolite with 12 mr (of size 6.6×6.7 $Å^2$ along the a and b axis, and 5.6×5.6 $Å^2$ along the c axis).[9] Currently, zeolite BEA has found industrial use as well as being the subject of many scientific studies.

1.1.2 Acid sites in zeolite

A completely siliceous zeolite, primarily composed of SiO_4 units, is stoichiometrically SiO_2 which is electrically neutral. When the tetrahedrally coordinated tetravalent framework Si atom is substituted with a trivalent element, for example, Al^{3+}, it results in a negative charge in the lattice which requires the presence of an extra-framework (EX) counter-cation to keep the overall framework neutral (Figure 1.1).[10] When this counter-ion is a proton that is bonded to a framework oxygen atom that in turn is bonded to one Al and one Si atom, the zeolite presents Brønsted acidity. The Brønsted acid sites (BAS) are the so-called bridging hydroxyl groups (Scheme 1.1a).[11] For the zeolites with different substituted framework atoms at T position (T = B, Ga, Ti, Fe, P, In, *etc.*), the Brønsted acid strength of the zeolites varies greatly.[12] For example, the acid strength with a predicted trend of [B] < [Fe] < [Ga] < [Al] was discovered for the corresponding substituted zeolites with experimental (*e.g.*, ammonia temperature program desorption (TPD), Infrared spectroscopy (IR), and catalytic activity) and computational measurements.[13, 14] When Zn is incorporated into the zeolite framework, referred to zincosillicate, we expect that theoretically a Zn^{2+} substituting a tetrahedrally coordinated framework Si would generate two negative charges in the lattice, which in turn would lead to two BAS with two protons to compensate the charges. However, no BAS but only Lewis acid sites (LAS) were observed on zincosilicates Zn-BEA by IR spectroscopy of adsorbed pyridine.[15]

Other than the bridging hydroxyl groups in zeolites, the silanol groups (SiOH) are the second most important type of hydroxyl groups. The SiOH groups located on the external surface of zeolites are called the terminal/free silanol groups (Scheme 1.1b) while the ones in the internal pores are called internal silanols. Some of these silanol groups show weak Brønsted acidity.[16]

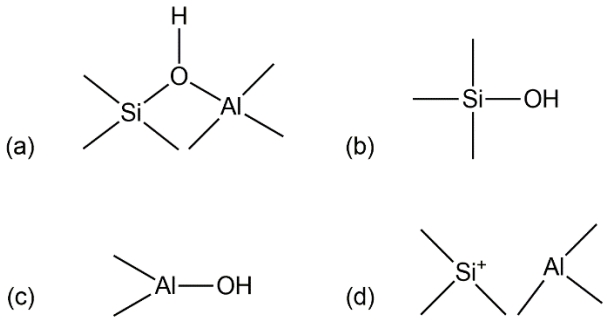

Scheme 1.1 Schematic representation of different types of hydroxyl groups and acid sites in zeolites. Adapted with permission from ref. [11]. Copyright (2011) John Wiley and Sons.

LAS in zeolites are important for their catalytic activities too. They mainly originate from two ways in the zeolite: (1) when the negative framework charges are balanced by EX metal cations,

which can be incorporated via ion exchange, it usually forms LAS; (2) some Al atoms are not tetrahedrally coordinated into the zeolite framework, leading to the EX aluminum (EX-Al) species and framework defects, which generate LAS (Scheme 1.1c, d).[11] The EX-Al and defects can be formed via dealumination of the zeolite framework via calcination, hydrothermal treatment, treatment with strong acids and so on. It has been reported that the LAS accompanied by vicinity bridging OH groups can form superacidic BAS.[17, 18] Zincosilicate CHA is known to have two different types of LAS, the "closed" and "open" sites in metal substituted zeolites (Scheme 1.2).[19, 20] The closed site represents the two negative charges generating from a bare Zn^{2+} cation (Scheme 1.2a) and compensated by two monovalent metal cations, while the open site is a mono cation ion-exchangeable site (Scheme 1.2b).[21, 22] The Zn-BEA was also reported to have different types of LAS (Scheme 1.3), and the structure of these LAS was examined by extended X-ray absorption fine structure (EXAFS) and IR spectroscopy of adsorbed pyridine/acetonitrile.[15]

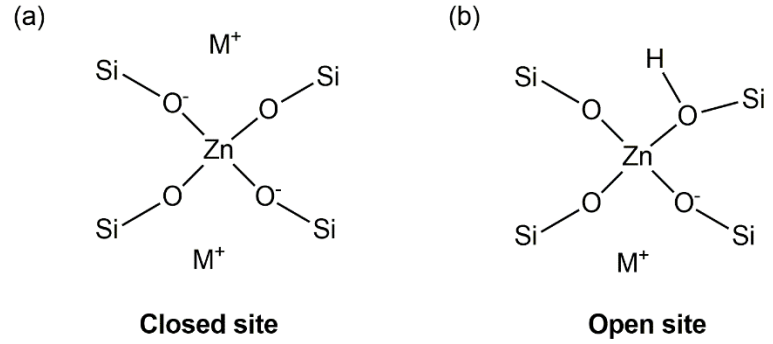

Scheme 1.2 Structures of two different Zn sites in zincosilicate CHA. Adapted with permission from ref. [22]. Copyright (2018) John Wiley and Sons.

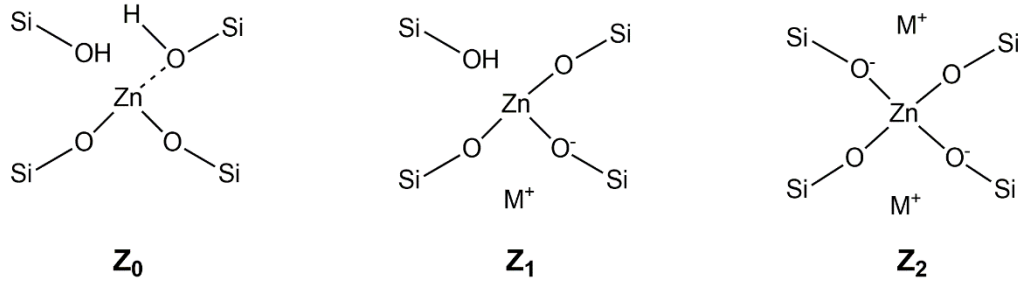

Scheme 1.3 Structure of three different Zn sites in zincosilicate BEA.[15]

In general, zeolites have been applied in a large number of academic and industrial fields with their Brønsted or Lewis acid characteristics, particularly in heterogeneous catalysis.

1.1.3 Application of zincosilicate in catalysis

To obtain suitable zeolite catalysts with proper acidic, basic, or bifunctional properties, the parent material plays an important role in tailoring catalysts in the right manner for the envisaged reaction. In the case of acidic zeolites, the parent material can significantly influence (1) the chemical nature of acid sites, *i.e.*, BAS and LAS; (2) their respective concentration or density; (3) their strength and strength distribution; and (4) accessibility of these acid sites at various locations, for example, on the external surface or inside the micropores.[12, 23] These properties are all highly related to their catalytic activity. The substitution of T-sites with Zn in zeolite frameworks has been studied for more than a quarter of a century.[24-28] Among the 259 types of zeolite frameworks known so far, 37 types that include Zn in the framework structure have been studied.[4, 23] They can be prepared by hydrothermal synthesis or post-synthesis treatments.[29] The substitution of Zn for the T-sites has some advantages over the introduction of Zn via ion exchange or impregnation. For example, the Zn will not be removed from the framework easily. The micropore blockage due to Zn cations located at the pore opening can also be reduced. The unique Zn sites with different properties from Al sites provide improvements on the catalytic activity in different fields.[23]

The large pore Zn-BEA (denoted CIT-6) was used on propane dehydrogenation.[30] A Pt-modified Zn-MFI was also found to reduce coking compared with Pt-modified H-ZSM-5 in propene aromatization.[31] Furthermore, several zincosilicates (*i.e.*, CIT-6, VPI-8, Zn-MFI, and Zn-MCM-41) were prepared to catalyze the Diels-Alder cycloaddition-dehydration reactions of ethene and methyl 5-(methoxymethyl)furan-2-carboxylate which can be derived quantitatively by partial oxidation of biomass-based 5-hydroxymethylfurfural. Zn-BEA was found to be the most selective catalyst.[15] Similar Diels-Alder cycloaddition-dehydration reactions (*e.g.*, direct production of dimethyl terephthalate from ethene and the dimethyl ester of furan-2,5-dicarboxylic acid) were not accessible with framework Sn-, Ti- or Zr-based LAS previously, demonstrating the superior activity of Zn sites in zincosilicates.[15]

Meanwhile, the superior selectivity and capacity of zincosilicate for stabilizing divalent cations such as Co^{2+}, Cu^{2+}, Fe^{2+}, and Ni^{2+} for catalytic applications have also been discovered.[22, 32] Aluminosilicate zeolites, in order to stabilize the active monomeric site of divalent metals, require two Al^{3+} within proximity (*e.g.*, Al paired configuration) because the substitution of one framework Si^{4+} atom with one Al^{3+} atom only generates one negative charge in the lattice.[22] The isolated (unpaired) framework Al^{3+} sites remain as BAS (when counterbalanced by protons), even after ion exchange with divalent metals, and hence cause side reactions and

catalyst deactivation.[15] In contrast, zincosilicate-like zeolite materials are promising platforms to stabilize divalent cations, taking advantage of two charge imbalance generated per Zn atom in the framework and they contain few BAS.[15] A zincosilicate in CHA topology was first synthesized by Koike *et al.* and it possessed a remarkably higher ion exchange ability for Ni^{2+}, compared to that of aluminosilicate and zincoaluminosilicate analogs.[33] Davis *et al.* also prepared Ni^{2+} exchanged zincosilicate in other topologies (*i.e.*, Ni-Zn-BEA and Ni-Zn-MCM-41) and used them for oligomerization of propene to higher molecular weight liquid hydrocarbons (C_{3n}, *i.e.*, C_6 and C_9) for blending into gasoline and distillate transportation fuel streams.[21] Compared with two Ni-containing aluminosilicates (Ni-HiAl-BEA and Ni-USY), zincosilicates demonstrated higher average selectivity to target products, as both of the aluminosilicate materials catalyzed cracking reactions, forming unwanted side products. The mesoporous zincosilicate Ni-Zn-MCM-41 showed the best ~99% selectivity to C_{3n} products. Furthermore, Pt^{2+} was ion-exchanged on Zn-MFI and encapsulated bimetallic $PtZn_x$ nanoclusters were formed via controlled demetallation and alloying with the framework Zn. An excellent shape selectivity and substrate specificity of the material was proved on the selective production of *p*-chloroaniline from the competitive hydrogenation of p-chloronitrobenzene and 1,3-dimethyl-5-nitrobenzene.[34]

Until now, the discovery of the structure and nature of the active sites in zincosilicate and the exploration of more sustainable synthesis routes for important chemicals with zncosilicates are the main challenges. In this work, Zn-BEA is used as the parent support for most catalysts, and Ga or Y sites were added via incipient wetness impregnation followed by other treatments to produce the final catalysts.

1.2 Propane dehydrogenation

Propene is a key commodity chemical used for the production of polypropylene, acrolein, acrylonitrile, oxy alcohols, and other chemical intermediates.[32, 35] Propane dehydrogenation (PDH) is an important method to obtain exclusively one particular alkene instead of a mixture of products from steam cracking and fluid catalytic cracking of naphtha, light diesel, and other oil byproducts, which are the most common methods for obtaining alkenes.[35] It is of current and future interest due to the increasing availability of the raw material (*i.e.*, propane) from shale gas. PDH produces propene and H_2 as the main products (Scheme 1.4). As a highly endothermic reaction with a standard enthalpy change (ΔH^0_{298K}) of 124.3 kJ·mol^{-1}, a considerably large amount of energy input is required for the forward reaction. Indeed, higher reaction temperatures (typically >823 K) and lower propane pressures ($p_{C_3H_8}$) are usually applied to achieve high conversions (>50%).[35] However, unwanted C-C bond cleavage reactions are also favored by most zeolite catalysts under these conditions, producing methane and ethene as the byproducts. Ethane is another byproduct formed via hydrogenation of ethene or direct hydrogenolysis of propane.[36] Propene is more reactive than propane, and it easily undergoes multistep secondary reactions including oligomerization, cyclization and aromatization on the same catalysts.[37, 38] As a result, the byproducts typically include methane, ethene, ethane, C_4-C_6 hydrocarbons, and aromatics.

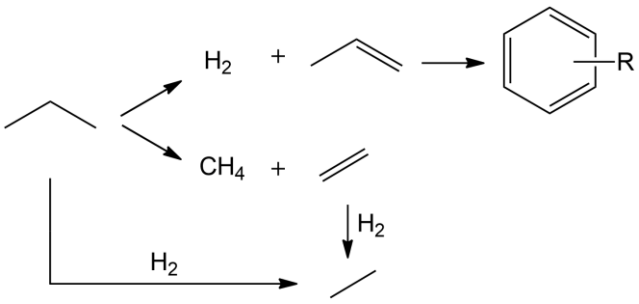

Scheme 1.4 Simplified reaction pathways of propane to propene and byproducts.

To date, several representative processes for traditional propane dehydrogenation have been commercialized.[39, 40]

1.2.1 Conventional route of propane dehydrogenation

Several emerging representative processes for propane dehydrogenation, like Catofin, Oleflex, FBD-4, PDH, STAR, ADHO, FCDh, and K-PRO^{TM} technologies have been industrialized in recent years.[35, 36] The simplified diagrams of these processes are shown in Figure 1.3 [36, 41] and the catalytic data are summarized in Table 1.1. Among them, the Catofin and Oleflex

processes are the two most widely applied PDH technologies. The commercial catalysts used for PDH are mostly Pt- and Cr-based catalysts. Catofin and FBD-4 processes use Cr-based catalysts, while the Oleflex, PDH, STAR and FCDh use Pt-based catalysts.[35] Apart from them, the catalysts of ADHO and K-PRO^{TM} contain neither Cr nor Pt.[36]

In the Catofin process,[42, 43] the K(Na)-CrO_x/Al_2O_3 catalyst (>18 wt.% CrO_x) has been used owing to the low price and high catalytic activity. Around 87% selectivity towards propene can be achieved at 40% conversion of alkanes with stable dehydrogenation performance (2-3 years lifetime). The system has low requirements on raw material indexes and fast load lifting speed after each feeding. However, in addition to the toxicity and environmental hostility, the low efficiency and large energy consumption are the disadvantageous. For another Cr-based catalyst, the FBD-4 process uses a basic metal-doped CrO_x/Al_2O_3 catalyst.[44] The propane conversion and propene selectivity are similar to that of the Catofin process (up to 45% conversion and 80% selectivity). However, unlike the Catofin process, the catalyst has to be transported to the regeneration tower (973 K) to remove the carbon deposit on the surface and then transferred back to the reaction tower for the next propane dehydrogenation cycle.

For Pt-based catalysts, the Honeywell UOP Oleflex process was commercialized in 1990.[45] It converts the propane-rich liquefied petroleum gas feedstock into chemical- or polymer-grade propene products with fully recyclable Pt-based alumina catalyst, which has low production cost, high returns on investment and low environmental footprints. For the “PDH” process by Linde and BASF Companies,[46] the latest catalyst focuses on Pt-Sn catalyst with more than 90% propene selectivity under isothermal operation. The catalyst lifetime can exceed 2 years due to the reduced coke accumulation. The STAR catalyst (Pt-Sn on Zn-Ca aluminate) is based on zinc and calcium aluminate support and exhibits excellent dehydrogenation performance with 35% propene selectivity at >80% conversion.[47] It is considered to be the only propane/butane dehydrogenation technology that can take advantage of oxidative dehydrogenation. Dow Chemical Company uses a fluidized catalytic dehydrogenation (FCDh) technology with shale gas as the feedstock.[48] Approximately 93% propene selectivity was achieved at ~45% propane conversion over K-promoted $PtGa/Al_2O_3$ catalyst. The simplicity of this system has largely achieved over 20% capital saving versus other commercial technologies.[36]

In 2016, a non-toxic, non-corrosive and non-noble metal oxide catalyst was reported by the China University of Petroleum for propane/butane dehydrogenation, which has been successfully industrialized in Shandong Hengyuan Petrochemical Company Limited.[49] The

process (ADHO technology) is operated with a highly efficient circulating fluidized bed reactor, and the catalyst has to be regenerated for continuous dehydrogenation reaction. At the end of 2018, the new propane dehydrogenation process, K-PRO^{TM}, was reported with the use of another novel catalyst free of noble metals and Cr. The technology is based on the commercially proven KBR Catalytic Olefins Technology (K-COT^{TM}) and the catalyst can be reused for 4-6 years.[36]

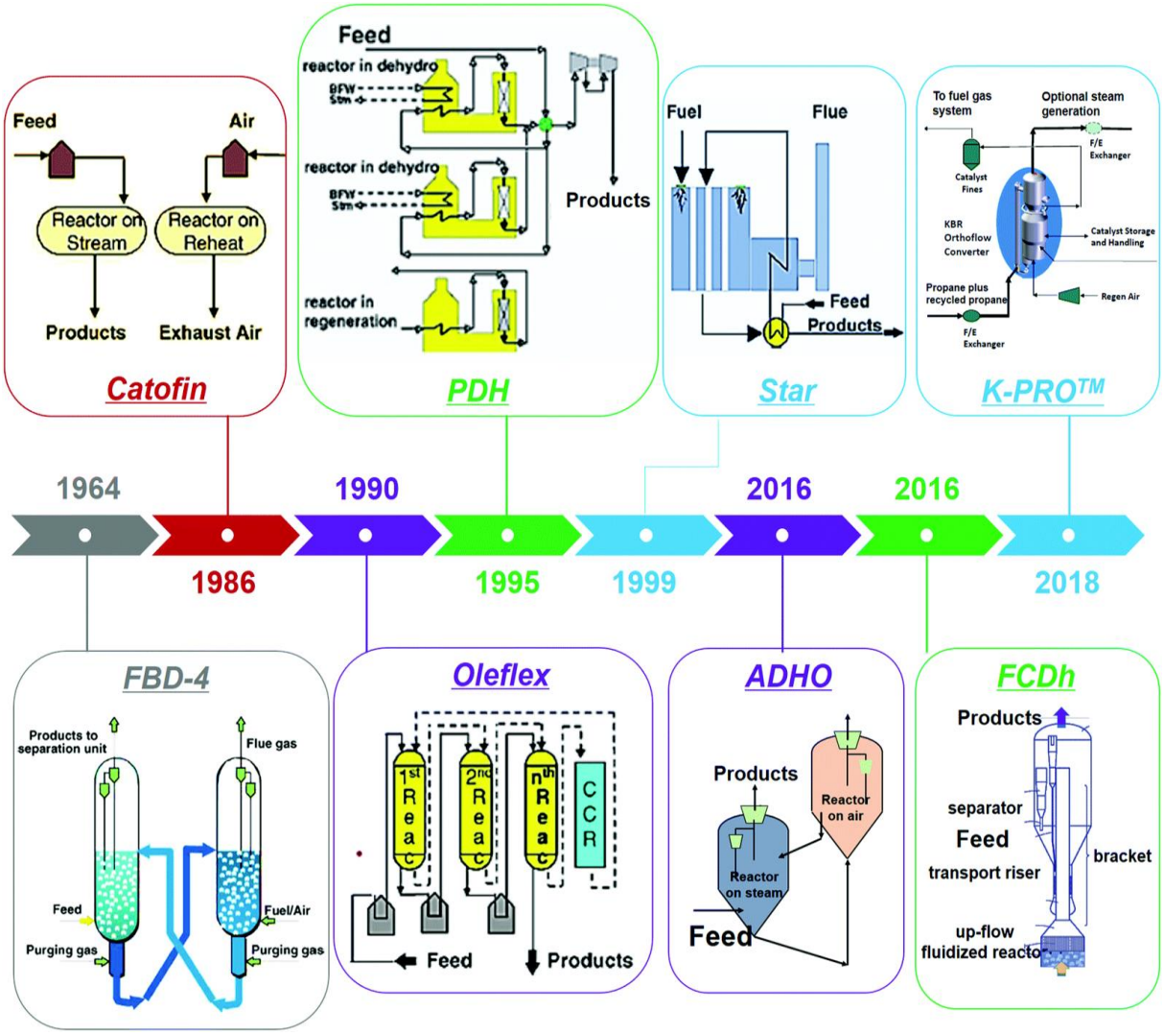

Figure 1.3 The representative technologies of propane dehydrogenation to propene. Adapted with permission from ref. [36]. Copyright (2021) Royal Society of Chemistry.

All the catalysts in Table 1.1 exhibit excellent propane dehydrogenation activity with above 80% propene selectivity, however, most of them have a high tendency to coking and sintering (particularly Pt-based catalysts), leading to fast deactivation. The frequent regeneration also leads to large energy consumption and high operating cost. The economical and/or environmental issues caused by Pt- and Cr-based catalysts have not yet been solved.

Table 1.1 Summary of the catalytic data of representative propane dehydrogenation technologies. Adapted with permission from ref. [36]. Copyright (2021) Royal Society of Chemistry.

Technology	FBD-4	Catofin	Oleflex	PDH	STAR	ADHO	FCDh	K-PRO™
Developer	Snamprogetti-Yarsintez	ABB Lummus	UOP	Linde-BASF	Phillips	China University of Petroleum	Dow Chemical Company	KBR
Time	1964	1986	1990	1995	1999	2016	2016	2018
Reactor	Fluidized bed	Horizontal fixed bed	Moving bed	Tubular fixed bed	Tubular fixed bed	Fluidized bed	Up-flow fluidized bed	Fluidized bed (riser)
Catalyst	CrO_x/Al_2O_3	$K(Na)\text{-}CrO_x/Al_2O_3$	K(Na)-Pt-Sn/ Al_2O_3	$Pt\text{-}Sn/ZrO_2$	$Pt\text{-}Sn/ZnAl_2O_4$/ $CaO\text{-}Al_2O_3$	Refractory mixed oxides	Pt-Ga-K/ $Si\text{-}Al_2O_3$	Non-Pt, non-Cr
T [K]	823-873	833-923	798-978	823-923	753-893	773-923	~873	~873
P [bar]	1.1-1.5	0.2-0.5	1-3	>1	5-6	--	1	1.5
WHSV [h^{-1}]	--	<1	4-13	--	0.5-10	1-10	--	--
Dilute gas	None	None	Cyclic H_2	None	Stream	None	N2	--
Operating period	Continuous regeneration	15-25 min	Continuous operation, 5-10 days	Reaction 6 h, regeneration 3 h	Reaction 6 h, regeneration 2 h	Continuous regeneration	Continuous regeneration	Continuous regeneration
Catalyst life [years]	--	2-3	1-3	> 2	> 5	--	--	4-6
Conversion [%]	45-50	40-45	30-40	40-45	~35	~50	~45	~45
Selectivity [%]	80-85	82-87	85.5-88	95	80-90	~90	~93	87-90

1.2.2 Propane dehydrogenation over Ga modified catalysts

Generally, the PDH is catalyzed by metal-based catalysts, metal oxide-based catalysts and other formulations, and an illustration of these catalysts is shown in Figure 1.4.[36] Among them, Ga-based catalysts have been intensively studied as they have more advantages over the toxicity, high cost and deactivation from Cr- and Pt-based materials. The dehydrogenation activity of Ga_2O_3 supported on ZSM-5 was first reported in the late 1980s for the conversion of propane to aromatics.[50, 51] In the interim, both bulk and supported Ga_2O_3 have been used as dehydrogenation catalysts. In early reports, Ga modified H-ZSM-5 showed high aromatic selectivity but not propane conversion.[52] The mechanism of propane aromatization has been proposed, in which PDH is the primary step of aromatization.[53, 54]

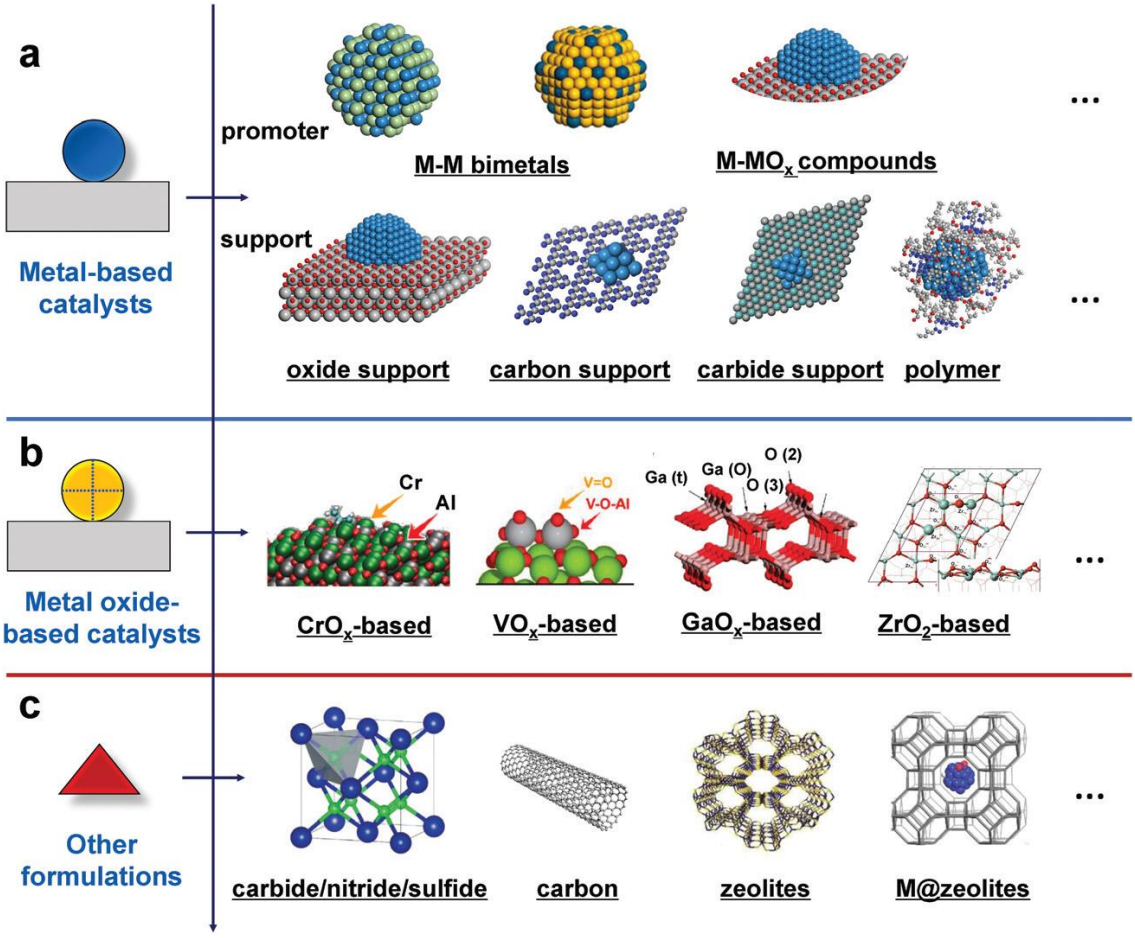

Figure 1.4 Model illustrations of different PDH catalysts: (a) metal-based catalysts, (b) metal oxide-based catalysts, and (c) other formulations. Adapted with permission from ref. [36]. Copyright (2021) Royal Society of Chemistry.

In recent years, the addition of Ga into zeolites has been reported to be particularly effective for light alkane dehydrogenation.[55-58] Ga/H-ZSM-5 catalyst had a PDH rate of two orders of magnitude higher with respect to parent H-ZSM-5. The homotopic Lewis-Brønsted acid pair,

formed by the interaction of a BAS with a Ga^{+}, were proposed as the active site.[59] Another Ga/H-MFI catalyst prepared via vapor-phase exchange was also used on PDH and propane cracking.[60] One order of magnitude higher PDH rate was achieved compared to the parent H-ZSM-5. The PDH rate was two orders of magnitude higher than the propane cracking rate, which resulted in superior propene selectivity. $[GaH]^{2+}$ cations were found to be the active centers for both propane dehydrogenation and cracking independently of the Ga/Al ratio.[60] Furthermore, a Ga-MFI obtained by isomorphous substitution of Ga in the MFI zeolite framework was also highly efficient for PDH.[61] The bridged framework Ga provided lower Brønsted acidity than Al and the presence of 3-mercaptopropyl-trimethoxysilane in the synthesis led to a weaker Brønsted acidity and stronger Lewis acidity, enhancing its PDH performance with higher dehydrogenation rate and selectivity. The LAS from highly dispersed EX-Ga^{3+} species were regarded as the main active sites[62] and the framework Ga sites were much less active.[63, 64] Moreover, the PDH performance was greatly improved with hierarchical Ga-MFI zeolite compared to bulk Ga-MFI catalyst by the repetitive branching or utilization of a long chain alkyl structure directing agent during the synthesis. A harder re-adsorption of propene and an advantageous quasi-2D distribution of BAS and LAS near the mesopores were responsible for the superior performance.[65] In order to inhibit the cracking and secondary reactions, high silica Ga-BEA catalysts were prepared from the dealuminated zeolite BEA. Ga was also found to substitute Al to generate BAS by the dry-gel conversion method. With the substitution of Ga for Al, the larger micropore surface area and higher Si/Ga ratio contributed to a higher propane conversion rate and propene selectivity.[32]

With diverse synthetic methods to incorporate Ga into zeolites,[32, 59-61, 65-69] a variety of Ga active species (*e.g.*, Ga^{3+}, Ga^{+}, $[GaO]^{+}$, $[GaH_x]^{\delta+}$, $[Ga(OH)]^{2+}$, $[Ga(OH)_2]^{+}$ and GaO_x clusters) have been suggested both experimentally and theoretically.[70-78] Nevertheless, the nature of these active sites remains to be debated. Meanwhile, propene selectivity is often limited by severe secondary reactions, such as dimerization and aromatization reactions, as they can be catalyzed by isolated BAS or isolated Ga cations easily.[79-81] It is highly important to introduce active and stable sites in zeolites for PDH while minimizing the number of sites that catalyze secondary reactions with propene. The exploitation of new efficient strategies for improving the activity, selectivity, stability, economical efficiency, and environmental friendliness by different preparation methods, supports and promoters is of significant importance.

1.3 Catalytic conversion of ethanol to 1,3-butadiene

The production of bio-derived ethanol has supplied 90% of the ethanol on the market nowadays.[82, 83] Around 67% bioethanol is used as transportation fuels to replace the nonrenewable ones as it has a higher octane number and can reduce greenhouse gas emissions.[84] However, it has drawbacks including the need for engine adaptations, only 2/3 energy density of gasoline, and the propensity to absorb water which may cause severe damage to the engine.[85] The production of value-added chemicals from bioethanol has been compared with its use in the transportation sector and it would be more economically viable with less CO_2 emissions.[86]

As shown in scheme 1.5, in the last few years, new technologies and strategic partnerships motivated to upgrade ethanol to more valuable chemicals such as ethene, acetaldehyde (AcH), ethyl acetate, acetic acid, 1,3-butadiene (1,3-BD), *n*-butanol, and so on.[87, 88] Among them, 1,3-BD is an important feedstock for the production of high-performance synthetic rubbers, which are extensively used in tires, toughened plastics, and many other products.[89] Currently, 1,3-BD is mainly produced from the isolation of naphtha steam cracker fractions from paraffinic hydrocarbons mixture, which is followed by distillation, in the manufacture of ethene and its higher homologues.[88] It accounts for over 95% of the worldwide 1,3-BD production.[90] The development of a cheap and sustainable process for 1,3-BD production from biomass-based resources would result in a reduced reliance on oil resources.

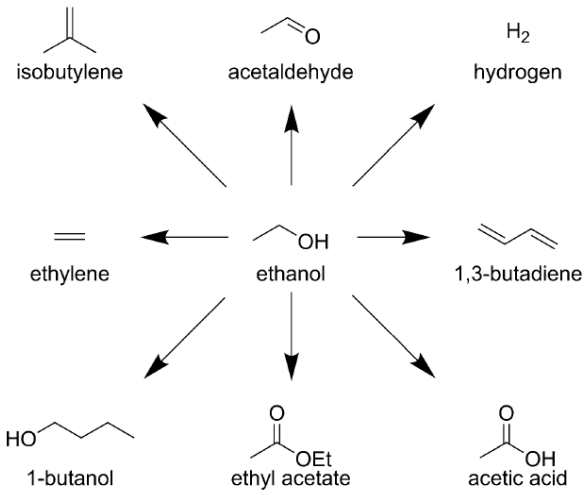

Scheme 1.5 The conversion of ethanol to a number of important bulk chemicals. Adapted with permission from ref. [88]. Copyright (2013) John Wiley and Sons.

1,3-BD was firstly found to be formed in small amounts by passing ethanol over powdered aluminum at the beginning of the 19th century by Ipatiev.[91] In 1915, the work of Ostromislenskiy showed that larger quantities of 1,3-BD could be produced by passing a

mixture of ethanol and AcH over alumina or clay catalysts.[92] Several research groups developed a two-step process including ethanol dehydrogenation and the reaction between AcH and ethanol to produce 1,3-BD.[93-95] Later, Lebedev noticed that it was possible to produce a considerable amount of 1,3-BD in one step with ethanol as the only feedstock, as shown in Scheme 1.6.[96] The one-step process used a catalyst consisting of silicon and magnesium oxides, with small amounts of other oxides present as promoters. It exhibited both dehydration and dehydrogenation activities. Even though the two-step process gave a higher 1,3-BD yield with higher purity, the greater simplicity and economic efficiency made the one-step process a more promising strategy for 1,3-BD production.

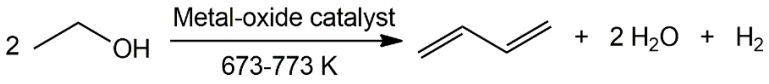

Scheme 1.6 The conversion of ethanol to 1,3-BD in one-step Lebedev process. Adapted with permission from ref. [88]. Copyright (2013) John Wiley and Sons.

1.3.1 Reaction mechanism of the production of 1,3-butadiene from ethanol

In recent years, more and more research articles about the conversion of ethanol to 1,3-BD have been published. However, the mechanism including several cascade steps has not yet been unequivocally established. The current understanding of the reaction mechanism comes predominantly from fragmentary evidence gathered over several decades by different research groups. The one- and two-step processes are generally recognized to follow the same reaction pathway.[97] Herein, two of the leading pathways including Prins reaction and Aldol condensation routes are discussed in detail.

1.3.1.1Prins reaction route

Generally, AcH is regarded as an important precursor to 1,3-BD formation. Gruver *et al.* proposed ethene as an intermediate for 1,3-BD formation over aluminated sepiolite catalysts, since both 1,3-BD selectivity and ethene selectivity increased at the same time with the total conversion.[98] As a result, a Prins-like reaction between AcH and ethene (both derived from ethanol), followed by dehydration to yield 1,3-BD has been suggested (Scheme 1.7).

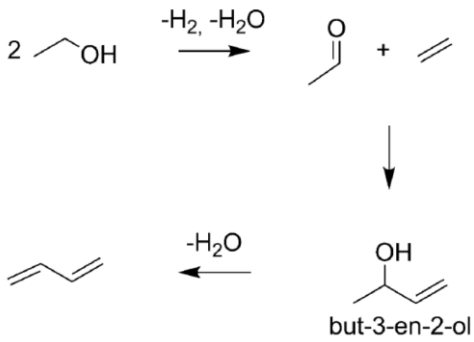

Scheme 1.7 The Prins reaction mechanism from ethanol to 1,3-BD. Adapted with permission from ref. [88]. Copyright (2013) John Wiley and Sons.

The Prins reaction enables the formation of C-C and C-O bonds (dioxanes) through an acid-catalyzed condensation of alkenes with aldehydes. The products can be unsaturated alcohols, glycols and acetals.[99] The production of 1,3-BD from ethanol via this route is of current interest because of the availability and low cost of lower olefins from shale gas and AcH from bioethanol. The Prins reaction usually requires LAS or BAS with weak-to medium strength, as strong acid sites would lead to severe coking and catalyst deactivation.[100] The catalysts have been reported to be homogeneous mineral acids (*e.g.*, sulfuric acid) and homogeneous Lewis acids (*e.g.*, $SnCl_4$, BF_3, and $ZnCl_2$).[101] In the Prins reaction between ethene and AcH, the main products are diols **1**, unsaturated alcohol **2**, and alkyl dioxanes **3** (scheme 1.8).[102] The overall product yield and selectivity depend on the employed reaction conditions, solvent, and catalyst.[103] Secondary compounds such as pyrans and dienes could also be formed via consecutive reactions of the primary products. Under anhydrous conditions and an excess of ethene, the cationic intermediate will lose a proton to form an unsaturated alcohol (*i.e.*, 3-buten-1-ol, **2**), which is the most desired product, since it affords 1,3-BD by simple thermal dehydration. When AcH is excess and at lower reaction temperatures, the reaction product is mainly a dioxane, **3**. And with water and a protic acid (*e.g.*, sulfuric acid) present, the favored pathway is to a 1,3-diol, **1**.[100, 103]

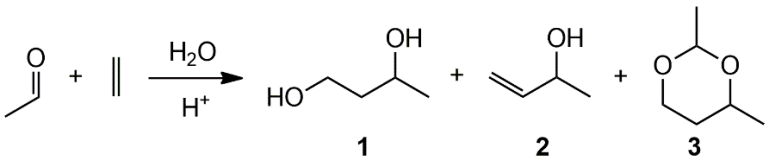

Scheme 1.8. Prins reaction of ethene and AcH.

The weakness of the Prins-like reaction for 1,3-BD synthesis is the protonation of ethene. It is an indispensable step and would generate a highly unstable primary carbocation, therefore, it has a high energy barrier.[110]

1.3.1.2Aldol condensation route

Toussaint and co-workers proposed an alternative mechanism based on the Aldol condensation between two AcH molecules formed upon ethanol dehydrogenation.[104] The Aldol condensation pathway is more favorable compared with the Prins-like pathway from theoretical calculations.[88, 105] It generally consists of five key steps, including (1) ethanol dehydrogenation; (2) AcH condensation to 3-hydroxybutanal (*i.e.*, acetaldol); (3) acetaldol dehydration to crotonaldehyde; (4) reduction of crotonaldehyde to crotyl alcohol; and (5) crotyl alcohol dehydration, corresponding to Scheme 1.9 a to e, respectively.[97]

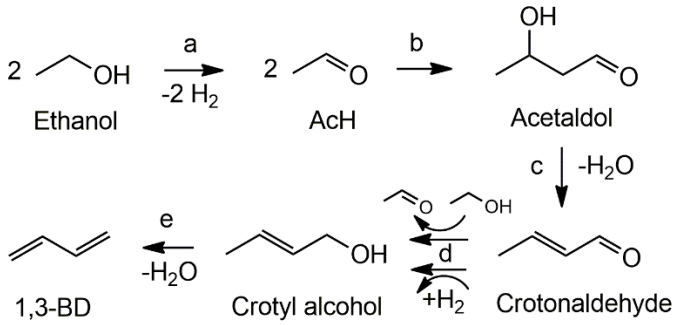

Scheme 1.9 The Aldol condensation pathway to 1,3-BD.[97]

Ethanol non-oxidative dehydrogenation is well-established as the first step to generate AcH which participates in the formation of C_4 precursors. With co-feeding deuterated and ^{14}C-labelled AcH and ethanol, the reversibility of ethanol dehydrogenation and the formation of 1,3-BD precursors from AcH were demonstrated.[106, 107] The Aldol condensation of two AcH molecules to 3-hydroxybutanal (commonly known as acetaldol) is the second elementary step (Scheme 1.9b). The acetaldol has been reported to be mostly absent in continuous flow heterogeneous catalytic reactions due to its high instability (*i.e.*, rapid dehydration to crotonaldehyde).[108-110] Davis and co-workers studied the Aldol condensation of AcH on TiO_2, hydroxyapatite and MgO. Crotonaldehyde was the only product observed.[111] Gao *et al.* studied the one-step process using the pulse reaction technique with a mass spectrometry over MgO-SiO_2 catalyst, and the sequential formation of AcH, acetaldol, crotonaldehyde, and 1,3-BD was observed.[112] Taifan *et al.* observed a band at 1273 cm^{-1} with diffuse reflectance infrared Fourier transform spectroscopy (DRIFTS), previously assigned to acetaldol, when reacting ethanol over MgO-SiO_2 during the temperature-programmed surface reaction (TPSR).[113] The quick dehydration of acetaldol to crotonaldehyde has been generally accepted as a key step in the Aldol condensation pathway. Crotonaldehyde was consumed at the same time to form crotyl alcohol (Scheme 1.9 d), making it an unstable secondary product as well.[109, 114]

Ethanol and H_2 can both be the hydrogen source for the reduction of crotonaldehyde to crotyl alcohol.[97] From theoretical calculation, the energy barrier is lower when using ethanol via the Meerwein-Ponndorf-Verley-Oppenauer (MPVO) reaction.[88] As a result, publications often disregard the role of H_2,[108] focusing instead on ethanol as more than a source of AcH in the reduction of crotonaldehyde.[104, 115] With isotopic labeling experiments, the deuterated crotyl alcohol was detected when labeled ethanol reacted with crotonaldehyde, and it is replaced by unlabeled crotyl alcohol upon switching to a non-isotopic feed, which further confirmed that ethanol was involved in crotyl alcohol formation.[116, 117] Moreover, the chemisorbed crotyl alcohol was found to disappear with the detection of signals attributed to vapor-phase 1,3-BD in DRIFTS monitored TPSR experiments, identifying crotyl alcohol as a kinetic precursor to 1,3-BD.[113] The dehydration of crotyl alcohol is highly favored thermodynamically,[88, 118] and can take place readily upon its formation on most "ethanol-to-1,3-BD catalysts". Therefore crotyl alcohol is often absent from the output stream of reactors.[97]

Although many researchers have subsequently adopted the general features of this mechanism, insufficient evidence has been gathered to conclude whether the generally accepted pathway follows a single mechanism or is dependent on the catalyst. Different suggestions have been proposed to what constitutes the rate determining step (RDS) in the reaction. Crotonaldehyde formation and crotonaldehyde reduction have both been proposed as the RDS and further studies are in progress.[119]

1.3.2 Typical catalysts for the conversion of ethanol to 1,3-butadiene

Many catalysts have been tested and reported in the literature since the research first began in the 1920s.[91, 92] Simultaneous attainment of high 1,3-BD productivity and selectivity is always challenging. The two main processes we mentioned before, the one-step process, which directly converts ethanol over a single catalyst to 1,3-BD, and the two-step process, where ethanol and AcH are both used as the feed to form 1,3-BD, require different active centers in the catalysts. For example, the one-step process needs active centers for both ethanol dehydrogenation and C-C bond coupling while the two-step process usually uses a catalyst that is highly active for C-C bond coupling.[120] Some transition-metal components (*e.g.*, Cu, Zn, and Ag) exhibited high dehydrogenation activity while some rare-earth metal components (*e.g.*, Y, La, Ce, Pr, and Nd) appeared to be active for the formation of C_4 products.[121] As a result, it has been proposed to merge these components in multifunctional catalysts to achieve the highest 1,3-BD productivity and selectivity.

The conversion of ethanol and AcH to 1,3-BD can be achieved with a series of MgO-SiO_2 catalysts with different structural properties due to different calcination temperatures.[122] The presence of LAS and intermediate amount of basic sites in MgO-SiO_2 calcined at 500°C greatly improved the catalytic activity with a high 1,3-BD selectivity of 80.7%. With an appropriate amount of water (10 wt.%) in the feed (mixture of 22.5 wt.% AcH/67.5 wt.% ethanol/10 wt.% water), the formation of *n*-butanol and coke precursors can be inhibited. On the other hand, metal-containing (M = Ag, Cu, Ni) oxide (MO_x= MgO, ZrO_2, Nb_2O_5, TiO_2, Al_2O_3) supported on silica showed improved dehydrogenation activity and can be used for the one-step 1,3-BD production.[109] The best catalytic performance was achieved over Ag/ZrO_2/SiO_2 catalyst with a 74% selectivity towards 1,3-BD. Tantalum-containing SiBEA zeolite with mononuclear Ta (V) was also active for the conversion of ethanol and AcH mixture into 1,3-BD, with selectivity of 80-90% at total 45-30% conversion of the mixture.[123] Similarly, with doping Ag, Cu, and Zn as additional dehydrogenation sites, the one-step conversion of ethanol to 1,3-BD can be achieved with a selectivity of 73% at 88% ethanol conversion over CuTaSiBEA at 598 K. The 1,3-BD selectivity increased in the order of TaSiBEA < ZnTaSiBEA < AgTaSiBEA < CuTaSiBEA.[124]

Recently, some publications used Zn and Y as the active centers for this reaction. Isolated Zn and Y sites supported on dealuminated zeolite BEA were prepared via incipient wetness impregnation and were found to be active for ethanol dehydrogenation and 1,3-BD formation, respectively.[125] In contrast to the widely reported reaction pathways, the authors proposed that the C-C bond coupling on Y-DeAlBEA proceeds via the reaction of co-adsorbed AcH and ethanol to form crotyl alcohol and water directly. When a bicomponent 0.15Zn-0.225Y-DeAlBEA was used, the synergistic effect of the bifunctional sites could be observed. The 1,3-BD productivity was 66.6 $mmol \cdot g^{-1} \cdot h^{-1}$ with a C_4 olefin selectivity of 61.6% (52% of 1,3-BD and 9.6% of butenes) at 673 K. Additionally, the structural confinement effects of different zeolites were also studied on constructed bicomponent Zn/Y/zeolite catalysts. The initial 1,3-BD productivity decreased with 5%Zn-5%Y/BEA > 5%Zn-5%Y/MCM-41 > 5%Zn-5%Y/SiO_2 under identical reaction conditions.[121] The intermediates can better react with each other on the coexisting neighboring Zn and Y sites to generate 1,3-BD in the BEA structure rather than escape as unwanted byproducts.[126] The highest 1,3-BD productivity of 43.1 $mmol \cdot g^{-1} \cdot h^{-1}$ with a selectivity of ~63% was achieved on 2%Zn-8%Y/BEA, even though the catalyst showed great activity loss during the reaction.[125] The study of the deactivation mechanism of Zn/Y/BEA found that AcH produced from ethanol was rapidly involved in a subsequent Aldol condensation with the simultaneous production of acetone.[127] AcH and acetone can go

through self- and cross-condensation reactions to produce unsaturated long-chain aldehydes and ketones. Finally, 2,4-dimethyl benzaldehyde was formed from cyclization reactions. It gradually covered the active sites and led to catalyst deactivation.

So far, more and more researchers focus on the development of efficient catalysts to improve 1,3-BD productivity. The reaction mechanism is always under debate and remains to be investigated.

1.4 Scope of this study

Zeolites supported metal catalysts are important catalysts in different fields in both industry and academia. Zincosilicate based zeolites have been applied to several important reactions, including dehydrogenation, Diels-Alder reaction, oligomerization, and so on. In the first part of this work, a series of zeolite catalysts based on zincosilicate BEA were prepared and characterized. Their physical and chemical properties were determined to better understand the catalytic performance on propane dehydrogenation and ethanol conversion.

In the second part, Ga-based materials have been reported to be promising catalysts for propane dehydrogenation, and these materials exhibited different performances with varied preparation methods. Even though a series of Ga active site structures have been proposed, the mechanism remains in debate. Ga/BEA catalysts prepared via hydrothermal synthesis of zincosilicate Zn-BEA, incipient wetness impregnation of Ga and leaching of Zn via H_2 reduction were applied on propane dehydrogenation. The study of reaction order, propane adsorption, kinetic isotope effect, rate determining step, kinetic equations, activation energy, number of active sites were carried out. A comparison with several other catalysts (*i.e.*, Ga/Zn-MFI, Ga-BEA (HS), Pt/Ga-BEA (HS)) is also presented.

In the third part, the conversion of ethanol to 1,3-BD, which is an important reaction in the manufacture of bioethanol to useful chemicals, is discussed. Zn-BEA and Y/Zn-BEA were applied on ethanol conversion due to their excellent potential on dehydrogenation and C-C bond coupling reactions, which are two main steps in the formation of 1,3-BD from ethanol. The catalytic performance, reaction pathway, rate determining step and reaction kinetics were investigated. The 1,3-BD productivity was greatly improved with the addition of Y to Zn-BEA.

This work provides a better understanding of the application of zincosilicate catalysts on heterogeneous catalysis and highly inspires the studies on propane dehydrogenation and ethanol conversion to 1,3-BD.

1.5 Reference

[1] N. Kosinov, C. Liu, E.J.M. Hensen, E.A. Pidko, Engineering of Transition Metal Catalysts Confined in Zeolites, Chemistry of Materials, 30 (2018) 3177-3198.

[2] X. Querol, N. Moreno, J.C. Umaña, A. Alastuey, E. Hernández, A. López-Soler, F. Plana, Synthesis of zeolites from coal fly ash: an overview, International Journal of Coal Geology, 50 (2002) 413-423.

[3] P. Del Campo, C. Martínez, A. Corma, Activation and conversion of alkanes in the confined space of zeolite-type materials, Chemical Society Reviews, (2021).

[4] I.Z. Association, http://www.iza-online.org/, accessed July 2021.

[5] S. Kulprathipanja, Zeolites in industrial separation and catalysis, John Wiley & Sons2010.

[6] G.T.K. R. L. Wadlinger, E. J. Rosinski, US Pat., No 3308069 (1967).

[7] J.M. Newsam, M.M.J. Treacy, W.T. Koetsier, C.B. De Gruyter, Structural Characterization of Zeolite Beta, Proceedings of the Royal Society of London. Series A, Mathematical and Physical Sciences, 420 (1988) 375-405.

[8] Á. Cantín, A. Corma, M.J. Díaz-Cabañas, J.L. Jordá, M. Moliner, F. Rey, Synthesis and Characterization of the All-Silica Pure Polymorph C and an Enriched Polymorph B Intergrowth of Zeolite Beta, Angewandte Chemie International Edition, 45 (2006) 8013-8015.

[9] Y. Kamimura, W. Chaikittisilp, K. Itabashi, A. Shimojima, T. Okubo, Critical Factors in the Seed-Assisted Synthesis of Zeolite Beta and "Green Beta" from OSDA-Free Na^+-Aluminosilicate Gels, Chemistry - An Asian Journal, 5 (2010) 2182-2191.

[10] M. Boronat, A. Corma, What Is Measured When Measuring Acidity in Zeolites with Probe Molecules?, ACS Catalysis, 9 (2019) 1539-1548.

[11] J.i. Čejka, A. Corma, S. Zones, Zeolites and catalysis: synthesis, reactions and applications, Wiley-VCH, Weinheim, 2010.

[12] A. Palčić, V. Valtchev, Analysis and control of acid sites in zeolites, Applied Catalysis A: General, 606 (2020) 117795.

[13] R.E. Patet, M. Koehle, R.F. Lobo, S. Caratzoulas, D.G. Vlachos, General Acid-Type Catalysis in the Dehydrative Aromatization of Furans to Aromatics in H-[Al]-BEA, H-[Fe]-BEA, H-[Ga]-BEA, and H-[B]-BEA Zeolites, The Journal of Physical Chemistry C, 121 (2017) 13666-13679.

[14] G. Ertl, H. Knözinger, J. Weitkamp, Handbook of heterogeneous catalysis, VCH Weinheim1997.

[15] M. Orazov, M.E. Davis, Catalysis by framework zinc in silica-based molecular sieves, Chemical Science, 7 (2016) 2264-2274.

[16] J.N. Kondo, E. Yoda, H. Ishikawa, F. Wakabayashi, K. Domen, Acid Property of Silanol Groups on Zeolites Assessed by Reaction Probe IR Study, Journal of Catalysis, 191 (2000) 275-281.

[17] E.M. Flanigen, J. Jansen, H. van Bekkum, Introduction to zeolite science and practice, Elsevier1991.

[18] R. Shigeishi, B.H. Chiche, F. Fajula, CO adsorption on superacid sites on dealuminated mazzite, Microporous and Mesoporous Materials, 43 (2001) 211-226.

[19] P. Wolf, M. Valla, A.J. Rossini, A. Comas-Vives, F. Núñez-Zarur, B. Malaman, A. Lesage, L. Emsley, C. Copéret, I. Hermans, NMR Signatures of the Active Sites in Sn-β Zeolite, Angewandte Chemie International Edition, 126 (2014) 10343-10347.

[20] R.E. Patet, S. Caratzoulas, D.G. Vlachos, Tandem Aromatization of Oxygenated Furans by Framework Zinc In Zeolites. A Computational Study, The Journal of Physical Chemistry C, 121 (2017) 22178-22186.

[21] M.A. Deimund, J. Labinger, M.E. Davis, Nickel-Exchanged Zincosilicate Catalysts for the Oligomerization of Propylene, ACS Catalysis, 4 (2014) 4189-4195.

[22] N. Koike, K. Iyoki, S.H. Keoh, W. Chaikittisilp, T. Okubo, Synthesis of New Microporous Zincosilicates with CHA Zeolite Topology as Efficient Platforms for Ion-Exchange of Divalent Cations, Chemistry-A European Journal, 24 (2018) 808-812.

[23] Y. Sakamoto, H.S. Zhao, H. Gies, K. Yamamoto, U. Kolb, T. Ikeda, A new microporous 12-ring zincosilicate THK-2 with many terminal silanols characterized by automated electron diffraction tomography, Dalton Transactions, 49 (2020) 12960-12969.

[24] A.D.a.B.J.M. P. McAnespie, U.S. Patent, No 4329328 (1982).

[25] M.A. Camblor, R.F. Lobo, H. Koller, M.E. Davis, Synthesis and characterization of zincosilicates with the SOD topology, Chemistry of Materials, 6 (1994) 2193-2199.

[26] T. Takewaki, L.W. Beck, M.E. Davis, Zincosilicate CIT-6: A precursor to a family of * BEA-type molecular sieves, The Journal of Physical Chemistry B, 103 (1999) 2674-2679.

[27] C. Röhrig, H. Gies, A New Zincosilicate Zeolite with Nine-Ring Channels, Angewandte Chemie International Edition, 34 (1995) 63-65.

[28] M.J. Annen, M.E. Davis, J.B. Higgins, J.L. Schlenker, VPI-7: The first zincosilicate molecular sieve containing three-membered T-atom rings, Journal of the Chemical Society, Chemical Communications, (1991) 1175-1176.

[29] M. Shamzhy, M. Opanasenko, P. Concepción, A. Martínez, New trends in tailoring active sites in zeolite-based catalysts, Chemical Society Reviews, 48 (2019) 1095-1149.
[30] P. Andy, M.E. Davis, Dehydrogenation of Propane over Platinum Containing CIT-6, Industrial & Engineering Chemistry Research, 43 (2004) 2922-2928.
[31] T. Inui, J.-B. Kim, T. Takeguchi, H. Nagata, Selective synthesis of aromatics from propene on platinum-modified zinco-silicate catalysts, Applied Catalysis A: General, 106 (1993) 83-95.
[32] M. Nakai, K. Miyake, R. Inoue, K. Ono, H. Al Jabri, Y. Hirota, Y. Uchida, S. Tanaka, M. Miyamoto, Y. Oumi, Dehydrogenation of propane over high silica* BEA type gallosilicate (Ga-Beta), Catalysis Science & Technology, 9 (2019) 6234-6239.
[33] N. Koike, K. Iyoki, S.H. Keoh, W. Chaikittisilp, T. Okubo, Synthesis of New Microporous Zincosilicates with CHA Zeolite Topology as Efficient Platforms for Ion-Exchange of Divalent Cations, Chemistry-A European Journal, 24 (2018) 808-812.
[34] T. Iida, D. Zanchet, K. Ohara, T. Wakihara, Y. Román-Leshkov, Concerted Bimetallic Nanocluster Synthesis and Encapsulation via Induced Zeolite Framework Demetallation for Shape and Substrate Selective Heterogeneous Catalysis, Angewandte Chemie International Edition, 57 (2018) 6454-6458.
[35] J.J.H.B. Sattler, J. Ruiz-Martinez, E. Santillan-Jimenez, B.M. Weckhuysen, Catalytic Dehydrogenation of Light Alkanes on Metals and Metal Oxides, Chemical Reviews, 114 (2014) 10613-10653.
[36] S. Chen, X. Chang, G. Sun, T. Zhang, Y. Xu, Y. Wang, C. Pei, J. Gong, Propane dehydrogenation: catalyst development, new chemistry, and emerging technologies, Chemical Society Reviews, 50 (2021) 3315-3354.
[37] M. Raad, S. Hamieh, J. Toufaily, T. Hamieh, L. Pinard, Propane aromatization on hierarchical Ga/HZSM-5 catalysts, Journal of Catalysis, 366 (2018) 223-236.
[38] V.R. Choudhary, D. Panjala, S. Banerjee, Aromatization of propene and n-butene over H-galloaluminosilicate (ZSM-5 type) zeolite, Applied Catalysis A: General, 231 (2002) 243-251.
[39] C. DEAN, Naphtha catalytic cracking for propylene production, Petroleum technology quarterly, 18 (2013).
[40] S. Sadrameli, Thermal/catalytic cracking of liquid hydrocarbons for the production of olefins: A state-of-the-art review II: Catalytic cracking review, Fuel, 173 (2016) 285-297.
[41] D. Sanfilippo, I. Miracca, Dehydrogenation of paraffins: synergies between catalyst design and reactor engineering, Catalysis Today, 111 (2006) 133-139.
[42] M.M. Bhasin, J.H. McCain, B.V. Vora, T. Imai, P.R. Pujadó, Dehydrogenation and oxydehydrogenation of paraffins to olefins, Applied Catalysis A: General, 221 (2001) 397-419.

[43] https://www.mcdermott.com/What-We-Do/Technology/Lummus/ Petrochemicals/ Olefins/Propylene-Production/Propane-Butane-Dehydrogenation. accessed July 2021.

[44] G.R. Kotelnikov, S.M. Komarov, V.P. Bespalov, D. Sanfilippo, I. Miracca, Application of FBD processes for C_3-C_4 olefins production from light paraffins, in: X. Bao, Y. Xu (Eds.) Studies in Surface Science and Catalysis, Elsevier 2004, pp. 67-72.

[45] https://www.honeywell.com/us/en/press/2019/09/honeywell-successfully-commissions-second-c3-oleflex-unit-for-zhejiang-satellite. Accessed July 2021.

[46] J. Lopez, Linde plan to jointly develop butadiene technology, https://www.icis.com/explore/resources/news/2014/06/03/9786384/basf-linde-plan-to-jointly-develop-butadienetechnology/. (2014), accessed on July 2021.

[47] https://www.thyssenkrupp-industrial-solutions.com/en/products-and-services/chemical-plants-and-processes/dehydrogenation-plants. Accessed July 2021.

[48] https://investors.dow.com/en/news/news-details/2019/Dow-to-Retrofit-Louisiana-Cracker-With-Fluidized-Catalytic-Dehydrogenation-FCDh-Technology-to-Produce-On-Purpose-Propylene/default.aspx. Accessed July 2021.

[49] G.W.a.N.S. C. Li, Chinese Patent, ZL201110123675.1 (2011).

[50] P. Meriaudeau, C. Naccache, Dehydrogenation and dehydrocyclization catalytic properties of gallium oxide, Journal of Molecular Catalysis, 50 (1989) L7-L10.

[51] N. Gnep, J. Doyemet, A. Seco, F.R. Ribeiro, M. Guisnet, Conversion of light alkanes to aromatic hydrocarbons: II. Role of gallium species in propane transformation on GaZSM5 catalysts, Applied catalysis, 43 (1988) 155-166.

[52] C. Bayense, J. Van Hooff, Aromatization of propane over gallium-containing H-ZSM-5 zeolites: Influence of the preparation method on the product selectivity and the catalytic stability, Applied Catalysis A: General, 79 (1991) 127-140.

[53] K.M. Dooley, C. Chang, G.L. Price, Effects of pretreatments on state of gallium and aromatization activity of gallium/ZSM-5 catalysts, Applied Catalysis A: General, 84 (1992) 17-30.

[54] E.G. Derouane, S.B. Abdul Hamid, I.I. Ivanova, N. Blom, P.-E. Højlund-Nielsen, Thermodynamic and mechanistic studies of initial stages in propane aromatisation over Ga-modified H-ZSM-5 catalysts, Journal of Molecular Catalysis, 86 (1994) 371-400.

[55] C.R. Bayense, A.J.H.P. van der Pol, J.H.C. van Hooff, Aromatization of propane over MFI-gallosilicates, Applied Catalysis, 72 (1991) 81-98.

[56] K.M. Dooley, T.F. Guidry, G.L. Price, Control of Intrazeolitic Gallium Cation Content and Its Effects on C_2 Dehydrogenation in Ga-MFI Catalysts, Journal of Catalysis, 157 (1995) 66-75.

[57] J. Bandiera, Y.B. Taarit, On the enhanced dehydrogenation versus cracking ability of an acidic gallium MFI: A tentative acid base interaction model, Applied Catalysis, 76 (1991) 199-208.

[58] E.A. Pidko, E.J.M. Hensen, R.A. van Santen, Dehydrogenation of Light Alkanes over Isolated Gallyl Ions in Ga/ZSM-5 Zeolites, The Journal of Physical Chemistry C, 111 (2007) 13068-13075.

[59] M.W. Schreiber, C.P. Plaisance, M. Baumgärtl, K. Reuter, A. Jentys, R. Bermejo-Deval, J.A. Lercher, Lewis-Brønsted Acid Pairs in Ga/H-ZSM-5 To Catalyze Dehydrogenation of Light Alkanes, Journal of the American Chemical Society, 140 (2018) 4849-4859.

[60] N.M. Phadke, E. Mansoor, M. Bondil, M. Head-Gordon, A.T. Bell, Mechanism and Kinetics of Propane Dehydrogenation and Cracking over Ga/H-MFI Prepared via Vapor-Phase Exchange of H-MFI with $GaCl_3$, Journal of the American Chemical Society, 141 (2018) 1614-1627.

[61] S.-W. Choi, W.-G. Kim, J.-S. So, J.S. Moore, Y. Liu, R.S. Dixit, J.G. Pendergast, C. Sievers, D.S. Sholl, S. Nair, Propane dehydrogenation catalyzed by gallosilicate MFI zeolites with perturbed acidity, Journal of Catalysis, 345 (2017) 113-123.

[62] V.J. Cybulskis, S.U. Pradhan, J.J. Lovón-Quintana, A.S. Hock, B. Hu, G. Zhang, W.N. Delgass, F.H. Ribeiro, J.T. Miller, The Nature of the Isolated Gallium Active Center for Propane Dehydrogenation on Ga/SiO_2, Catalysis Letters, 147 (2017) 1252-1262.

[63] V.R. Choudhary, P. Devadas, A.K. Kinage, C. Sivadinarayana, M. Guisnet, Acidity, catalytic activity, and deactivation of H-gallosilicate (MFI) in propane aromatization: Influence of hydrothermal pretreatments, Journal of Catalysis, 158 (1996) 537-550.

[64] V.R. Choudhary, C. Sivadinarayana, A.K. Kinage, P. Devadas, M. Guisnet, H-gallosilicate (MFI) propane aromatization catalyst - Influence of calcination temperature on acidity, activity and deactivation due to coking, Applied Catalysis A-General, 136 (1996) 125-142.

[65] W.-g. Kim, J. So, S.-W. Choi, Y. Liu, R.S. Dixit, C. Sievers, D.S. Sholl, S. Nair, C.W. Jones, Hierarchical Ga-MFI catalysts for propane dehydrogenation, Chemistry of Materials, 29 (2017) 7213-7222.

[66] V.J. Cybulskis, S.U. Pradhan, J.J. Lovón-Quintana, A.S. Hock, B. Hu, G. Zhang, W.N. Delgass, F.H. Ribeiro, J.T. Miller, The Nature of the Isolated Gallium Active Center for Propane Dehydrogenation on Ga/SiO_2, Catalysis Letters, 147 (2017) 1252-1262.

[67] R. Fricke, H. Kosslick, G. Lischke, M. Richter, Incorporation of gallium into zeolites: syntheses, properties and catalytic application, Chemical Reviews, 100 (2000) 2303-2406.

[68] K.C. Szeto, A. Gallo, S. Hernández-Morejudo, U. Olsbye, A. De Mallmann, F. Lefebvre, R.M. Gauvin, L. Delevoye, S.L. Scott, M. Taoufik, Selective Grafting of $Ga(i\text{-}Bu)_3$ on the Silanols of Mesoporous H-ZSM-5 by Surface Organometallic Chemistry, The Journal of Physical Chemistry C, 119 (2015) 26611-26619.

[69] K. Searles, G. Siddiqi, O.V. Safonova, C. Copéret, Silica-supported isolated gallium sites as highly active, selective and stable propane dehydrogenation catalysts, Chemical Science, 8 (2017) 2661-2666.

[70] J.A. Biscardi, E. Iglesia, Structure and function of metal cations in light alkane reactions catalyzed by modified H-ZSM5, Catalysis Today, 31 (1996) 207-231.

[71] K.M. Dooley, G.L. Price, V.I. Kanazirev, V.I. Hart, Gallium-loaded zeolites for light paraffin aromatization: Evidence for exchanged gallium cation active centers, Catalysis Today, 31 (1996) 305-315.

[72] N. Rane, A.R. Overweg, V.B. Kazansky, R.A. van Santen, E.J.M. Hensen, Characterization and reactivity of Ga^+ and GaO^+ cations in zeolite ZSM-5, Journal of Catalysis, 239 (2006) 478-485.

[73] E.J.M. Hensen, E.A. Pidko, N. Rane, R.A. van Santen, Water-promoted hydrocarbon activation catalyzed by binuclear gallium sites in ZSM-5 zeolite, Angewandte Chemie International Edition, 46 (2007) 7273-7276.

[74] Y.V. Joshi, K.T. Thomson, The roles of gallium hydride and Brønsted acidity in light alkane dehydrogenation mechanisms using Ga-exchanged HZSM-5 catalysts: A DFT pathway analysis, Catalysis Today, 105 (2005) 106-121.

[75] Y. Yuan, C. Brady, R.F. Lobo, B. Xu, Understanding the Correlation between Ga Speciation and Propane Dehydrogenation Activity on Ga/H-ZSM-5 Catalysts, ACS Catalysis, (2021) 10647-10659.

[76] E. Mansoor, M. Head-Gordon, A.T. Bell, Computational Modeling of the Nature and Role of Ga Species for Light Alkane Dehydrogenation Catalyzed by Ga/H-MFI, ACS Catalysis, 8 (2018) 6146-6162.

[77] N.M. Phadke, E. Mansoor, M. Head-Gordon, A.T. Bell, Mechanism and Kinetics of Light Alkane Dehydrogenation and Cracking over Isolated Ga Species in Ga/H-MFI, ACS Catalysis, 11 (2021) 2062-2075.

[78] E.A. Pidko, V.B. Kazansky, E.J.M. Hensen, R.A. van Santen, A comprehensive density functional theory study of ethane dehydrogenation over reduced extra-framework gallium species in ZSM-5 zeolite, Journal of Catalysis, 240 (2006) 73-84.
[79] A. Bhan, W. Nicholas Delgass, Propane Aromatization over HZSM-5 and Ga/HZSM-5 Catalysts, Catalysis Reviews, 50 (2008) 19-151.
[80] D.B. Lukyanov, N.S. Gnep, M.R. Guisnet, Kinetic modeling of propane aromatization reaction over HZSM-5 and GaHZSM-5, Industrial & Engineering Chemistry Research, 34 (1995) 516-523.
[81] M. Guisnet, N.S. Gnep, Aromatization of propane over GaHMFI catalysts. Reaction scheme, nature of the dehydrogenating species and mode of coke formation, Catalysis Today, 31 (1996) 275-292.
[82] A. Duque, C. Álvarez, P. Doménech, P. Manzanares, A.D. Moreno, Advanced Bioethanol Production: From Novel Raw Materials to Integrated Biorefineries, Processes, 9 (2021).
[83] C.N. Hamelinck, G.v. Hooijdonk, A.P.C. Faaij, Ethanol from lignocellulosic biomass: techno-economic performance in short-, middle- and long-term, Biomass and Bioenergy, 28 (2005) 384-410.
[84] L. Wei, L.O. Pordesimo, C. Igathinathane, W.D. Batchelor, Process engineering evaluation of ethanol production from wood through bioprocessing and chemical catalysis, Biomass and Bioenergy, 33 (2009) 255-266.
[85] S. Searle, F. Posada, C. Malins, J. German, Technical barriers to the consumption of higher blends of ethanol, ICCT report, (2014).
[86] J. Rass-Hansen, H. Falsig, B. Jorgensen, C.H. Christensen, Bioethanol: fuel or feedstock?, Journal of Chemical Technology and Biotechnology, 82 (2007) 329-333.
[87] P.H. Rana, P.A. Parikh, Catalytic Transformation of Ethanol to Industrially Relevant Fine Chemicals, in: S. Nanda, D.-V. N. Vo, P.K. Sarangi (Eds.) Biorefinery of Alternative Resources: Targeting Green Fuels and Platform Chemicals, Springer Singapore, Singapore, 2020, pp. 49-74.
[88] C. Angelici, B.M. Weckhuysen, P.C.A. Bruijnincx, Chemocatalytic Conversion of Ethanol into Butadiene and Other Bulk Chemicals, ChemSusChem, 6 (2013) 1595-1614.
[89] Y. Qi, Z. Liu, S. Liu, L. Cui, Q. Dai, J. He, W. Dong, C. Bai, Synthesis of 1,3-Butadiene and Its 2-Substituted Monomers for Synthetic Rubbers, Catalysts, 9 (2019).
[90] W.C. White, Butadiene production process overview, Chemico-Biological Interactions, 166 (2007) 10-14.

[91] V. Ipatiev, ZrJr question Iber the decasation of hhyl alcohol in the presence of various catalysts, J Prakt Chem, 2 (1903) 67-70.

[92] J. Ostromislenskiy, Production of butadiene, J. Russ. Phys. Chem. Soc, 47 (1915) 1472-1506.

[93] B. Corson, H. Jones, C. Welling, J. Hinckley, E. Stahly, Butadiene from Ethyl Alcohol. Catalysis in the One-and Two-Stop Processes, Industrial & Engineering Chemistry, 42 (1950) 359-373.

[94] W. Quattlebaum, W. Toussaint, J. Dunn, Deoxygenation of certain aldehydes and ketones: preparation of butadiene and styrene1, Journal of the American Chemical Society, 69 (1947) 593-599.

[95] W. Toussaint, J. Dunn, D. Jachson, Production of butadiene from alcohol, Industrial & Engineering Chemistry, 39 (1947) 120-125.

[96] S. Lebedev, British Patent 331402, 1929; b) SV Lebedev, British Patent 331482, 1930; c) SV Lebedev, French Patent 665917, 1929; d) SV Lebedev, Russian Journal of General Chemistry, 3 (1933) 698-708.

[97] G. Pomalaza, P.A. Ponton, M. Capron, F. Dumeignil, Ethanol-to-butadiene: the reaction and its catalysts, Catalysis Science & Technology, 10 (2020) 4860-4911.

[98] V. Gruver, A. Sun, J.J. Fripiat, Catalytic Properties of Aluminated Sepiolite in Ethanol Conversion, Catalysis Letters, 34 (1995) 359-364.

[99] E. Arundale, L. Mikeska, The Olefin-Aldehyde Condensation. The Prins Reaction, Chemical Reviews, 51 (1952) 505-555.

[100] S.P. Bedenko, K.I. Dement'ev, V.F. Tret'yakov, A.L. Maksimov, The Prins Reaction over Heterogeneous Catalysts (a Review), Petroleum Chemistry, 60 (2020) 723-730.

[101] E.S. Vasiliadou, N.S. Gould, R.F. Lobo, Zeolite-Catalyzed Formaldehyde-Propylene Prins Condensation, ChemCatChem, 9 (2017).

[102] F. Doro, N. Akeroyd, F. Schiet, A. Narula, The Prins Reaction in the Fragrance Industry: 100th Anniversary (1919-2019), Angewandte Chemie International Edition, 58 (2019) 7174-7179.

[103] I.M. Pastor, M. Yus, The Prins reaction: advances and applications, Current Organic Chemistry, 11 (2007) 925-957.

[104] W.M. Quattlebaum, W.J. Toussaint, J.T. Dunn, Deoxygenation of Certain Aldehydes and Ketones - Preparation of Butadiene and Styrene, Journal of the American Chemical Society, 69 (1947) 593-599.

[105] W.E. Taifan, T. Bučko, J. Baltrusaitis, Catalytic conversion of ethanol to 1,3-butadiene on MgO: A comprehensive mechanism elucidation using DFT calculations, Journal of Catalysis, 346 (2017) 78-91.

[106] M.D. Jones, C.G. Keir, C. Di Iulio, R.A.M. Robertson, C.V. Williams, D.C. Apperley, Investigations into the conversion of ethanol into 1,3-butadiene, Catalysis Science & Technology, 1 (2011) 267-272.

[107] M. Lewandowski, G.S. Babu, M. VezzOli, M.D. Jones, R.E. Owen, D. Mattia, P. Plucinski, E. Mikolajska, A. Ochenduszko, D.C. Apperley, Investigations into the conversion of ethanol to 1,3-butadiene using $MgO:SiO_2$ supported catalysts, Catalysis Communications, 49 (2014) 25-28.

[108] W.E. Taifan, T. Bucko, J. Baltrusaitis, Catalytic conversion of ethanol to 1,3-butadiene on MgO: A comprehensive mechanism elucidation using DFT calculations, Journal of Catalysis, 346 (2017) 78-91.

[109] V.L. Sushkevich, I.I. Ivanova, V.V. Ordomsky, E. Taarning, Design of a Metal-Promoted Oxide Catalyst for the Selective Synthesis of Butadiene from Ethanol, ChemSusChem, 7 (2014) 2527-2536.

[110] T. De Baerdemaeker, M. Feyen, U. Muller, B. Yilmaz, F.S. Xiao, W.P. Zhang, T. Yokoi, X.H. Bao, H. Gies, D.E. De Vos, Bimetallic Zn and Hf on Silica Catalysts for the Conversion of Ethanol to 1,3-Butadiene, ACS Catalysis, 5 (2015) 3393-3397.

[111] Z.D. Young, S. Hanspal, R.J. Davis, Aldol Condensation of Acetaldehyde over Titania, Hydroxyapatite, and Magnesia, ACS Catalysis, 6 (2016) 3193-3202.

[112] M.X. Gao, Z.Z. Liu, M.H. Zhang, L. Tong, Study on the Mechanism of Butadiene Formation from Ethanol, Catalysis Letters, 144 (2014) 2071-2079.

[113] W.E. Taifan, G.X. Yan, J. Baltrusaitis, Surface chemistry of MgO/SiO_2 catalyst during the ethanol catalytic conversion to 1,3-butadiene: in-situ DRIFTS and DFT study, Catalysis Science & Technology, 7 (2017) 4648-4668.

[114] G.M.C. Gonzalez, R. Murciano, A.L.V. Perales, A. Martinez, F. Vidal-Barrero, M. Campoy, Ethanol conversion into 1,3-butadiene over a mixed Hf-Zn catalyst: A study of the reaction pathway and catalyst deactivation, Applied Catalysis A-General, 570 (2019) 96-106.

[115] H.E. Jones, E.E. Stahly, B.B. Corson, Butadiene from Ethanol - Reaction Mechanism, Journal of the American Chemical Society, 71 (1949) 1822-1828.

[116] P. Muller, S.P. Burt, A.M. Love, W.P. McDermott, P. Wolf, I. Hermans, Mechanistic Study on the Lewis Acid Catalyzed Synthesis of 1,3-Butadiene over Ta-BEA Using Modulated Operando DRIFTS-MS, ACS Catalysis, 6 (2016) 6823-6832.

[117] T.T. Yan, W.L. Dai, G.J. Wu, S. Lang, M. Hunger, N.J. Guan, L.D. Li, Mechanistic Insights into One-Step Catalytic Conversion of Ethanol to Butadiene over Bifunctional Zn-Y/Beta Zeolite, ACS Catalysis, 8 (2018) 2760-2773.

[118] E.V. Makshina, M. Dusselier, W. Janssens, J. Degreve, P.A. Jacobs, B.F. Sels, Review of old chemistry and new catalytic advances in the on-purpose synthesis of butadiene, Chemical Society Reviews, 43 (2014) 7917-7953.

[119] R. Johansson, S.L. Hruby, J. Rass-Hansen, C.H. Christensen, The hydrocarbon pool in ethanol-to-gasoline over HZSM-5 catalysts, Catalysis Letters, 127 (2009) 1-6.

[120] M.D. Jones, Catalytic transformation of ethanol into 1,3-butadiene, Chemistry Central Journal, 8 (2014).

[121] W. Dai, S. Zhang, Z. Yu, T. Yan, G. Wu, N. Guan, L. Li, Zeolite Structural Confinement Effects Enhance One-Pot Catalytic Conversion of Ethanol to Butadiene, ACS Catalysis, 7 (2017) 3703-3706.

[122] Q. Zhu, B. Wang, T. Tan, Conversion of ethanol and acetaldehyde to butadiene over MgO-SiO_2 catalysts: effect of reaction parameters and interaction between MgO and SiO_2 on catalytic performance, ACS Sustainable Chemistry & Engineering, 5 (2017) 722-733.

[123] P.I. Kyriienko, O.V. Larina, S.O. Soloviev, S.M. Orlyk, S. Dzwigaj, High selectivity of TaSiBEA zeolite catalysts in 1,3-butadiene production from ethanol and acetaldehyde mixture, Catalysis Communications, 77 (2016) 123-126.

[124] P.I. Kyriienko, O.V. Larina, S.O. Soloviev, S.M. Orlyk, C. Calers, S. Dzwigaj, Ethanol Conversion into 1,3-Butadiene by the Lebedev Method over MTaSiBEA Zeolites (M=Ag, Cu, Zn), ACS Sustainable Chemistry & Engineering, 5 (2017) 2075-2083.

[125] L. Qi, Y.F. Zhang, M.A. Conrad, C.K. Russell, J. Miller, A.T. Bell, Ethanol Conversion to Butadiene over Isolated Zinc and Yttrium Sites Grafted onto Dealuminated Beta Zeolite, Journal of the American Chemical Society, 142 (2020) 14674-14687.

[126] T. Yan, W. Dai, G. Wu, S. Lang, M. Hunger, N. Guan, L. Li, Mechanistic Insights into One-Step Catalytic Conversion of Ethanol to Butadiene over Bifunctional Zn-Y/Beta Zeolite, ACS Catalysis, 8 (2018) 2760-2773.

[127] T. Yan, L. Yang, W. Dai, C. Wang, G. Wu, N. Guan, M. Hunger, L. Li, On the deactivation mechanism of zeolite catalyst in ethanol to butadiene conversion, Journal of Catalysis, 367 (2018) 7-15.

Chapter 2

2. Preparation and characterization of materials

2.1 Abstract

Zincosillicate with BEA structure (Zn-BEA) was prepared and used as support and catalyst for propane dehydrogenation and ethanol conversion. Ga and Y were introduced into Zn-BEA via incipient wetness impregnation. With subsequent H_2 treatment, the demetallization of Zn was carried out to produce Ga/BEA with both framework and extra-framework Ga sites. Zn-BEA has a significant amount of LAS and few BAS. An increase in BET surface area and micropore volume was observed on Ga/BEA after Zn-leaching. The BAS and LAS of Ga/BEA increased linearly with Ga loading. For Y/Zn-BEA, mainly the LAS concentration increased with Y loading compared to Zn-BEA. On the contrary, the micropore volume decreased with Y loading, suggesting an introduction of Y into the micropores. For comparison, Zn-MFI and Ga-BEA (HS) from direct hydrothermal synthesis were prepared and Ga and Pt were introduced by incipient wetness impregnation on Zn-MFI and Ga-BEA (HS), respectively.

2.2 Introduction

Zeolites continue to play an increasingly important role in heterogeneous catalysis in both industry and academia. Substituting a tetrahedrally coordinated framework Si^{4+} with Zn^{2+} instead of Al^{3+}, as in traditional aluminosilicate, has been found to provide unique advantages compared to aluminosilicates and zeolites with Zn introduced via ion-exchange or impregnation.[1, 2] The knowledge about the structure and properties of these materials is a prerequisite for understanding their catalytic performance.

Different characterization techniques have been applied to investigate zeolite materials (Table 2.1). X-ray diffraction (XRD) and elemental analysis examine the crystalline structure, Si/Al ratio and other metal contents of the materials. N_2 physisorption reveals the specific surface area and micropore volume in the zeolites. These are important parameters to verify the successful synthesis and are related to their catalytic performance. Most importantly, similar to other solid acids, zeolites possess both BAS and LAS, which are typically bridging hydroxyl groups and coordinatively unsaturated cations, respectively. IR spectroscopy has been established as an essential tool to investigate intermolecular interactions within zeolites, for example, hydrogen and coordination bondings.[3] IR spectra of activated zeolites typically give rise to two or more major bands in the hydroxyl spectral region, with silanol groups at 3710-3760 cm^{-1} and O-H stretching mode of the bridged group at 3600-3620 cm^{-1}.[4, 5] The bridged hydroxyl group is the most important chemical entity as they are typically strong BAS. Pyridine was first proposed as the adsorbed probe molecule to give valuable information on the acidic properties as early as 1963,[6] giving ring vibrations in the region 1600-1400 cm^{-1} to identify pyridine bounding to different surface sites.[7] The quantitative information according to the nature, number, and strength of the acid sites reacting with pyridine can also be determined.[8]

The Zn-BEA was synthesized and used as the parent sample for most catalysts in this work. The Ga/BEA, which is the main catalyst used on propane dehydrogenation, was prepared in general via three steps including the synthesis of Zn-BEA, Ga addition via incipient wetness impregnation and Zn leaching by H_2 treatment. When applying the catalysts on ethanol conversion to 1,3-BD, Y was introduced to Zn-BEA by incipient wetness impregnation to improve the 1,3-BD productivity. For comparison, Zn-MFI, Ga-BEA (HS, HS refers to hydrothermal synthesis), Ga/Zn-MFI, Ga/MFI and Pt/Ga-BEA (HS) were also prepared. In this chapter, we describe the preparation methods and the characterization of the physical and chemical properties of all the prepared catalysts. It helped to rationally design the catalysts and obtain further understanding of their catalytic performance.

Table 2.1 The properties of catalysts measured by different characterization techniques

Characterization technique	Physical and chemical properties measured
XRD	Crystallographic structure
N_2 physisorption	BET surface area and micropore volume
Elemental analysis	Element content
IR spectroscopy of pyridine adsorption	Concentration and strength of LAS and BAS

2.3 Catalyst preparation

2.3.1 Zn-BEA

Hydrothermal synthesis of Zn-BEA was carried out according to a method previously reported by Davis *et al*.[2, 9] The synthesis gel was prepared by adding colloidal silica (LUDOX@AS-40), zinc acetate dihydrate (Alfa Aesar, ≥98.0%), tetraethylammonium hydroxide (TEAOH, Sigma Aldrich, 35 wt.% in water), lithium hydroxide monohydrate (Sigma Aldrich, ≥99.0%) and water with a molar composition of 1 SiO_2/0.03 $Zn(OAc)_2$/0.65 TEAOH/0.05 LiOH/30 H_2O into a Teflon liner. Subsequently, the Teflon liner was introduced into a stainless steel autoclave and heated at 410 K for 7.5 days. The obtained solid was separated from the liquid by centrifugation, and afterward washed with water and dried at 353 K overnight. The dried powder was calcined in 100 $mL \cdot min^{-1}$ synthetic air (20% O_2 in N_2) by 1 $K \cdot min^{-1}$ to 823 K and kept at 823 K for 10 h to remove the structure directing agent. The zeolite was further converted into proton form by ion exchange with 1.0 M NH_4NO_3 (Sigma Aldrich, ≥99.5%) solution at 353 K for 10 h followed by the same calcination procedure as described above.

2.3.2 Zn-MFI

Hydrothermal synthesis of Zn-MFI was carried out according to a previously reported method.[2] Zinc sulfate heptahydrate (Sigma Aldrich, >99.0%) was dissolved in distilled water and ammonia solution (Sigma Aldrich, 25% solution in water) was added into the solution until the pH increased to ~6 to form a white precipitate ($Zn(OH)_2$). Then the precipitate was filtered, washed thoroughly with distilled water, and dried. Later sodium hydroxide (Sigma Aldrich, >98%) and tetrapropylammonium hydroxide (TPAOH, Sigma Aldrich 40% solution in water) dissolved in distilled water were added to the precipitate. The mixture was stirred until the precipitate dissolved. Colloidal silica (LUDOX@AS-40) was finally added with thorough stirring to maintain a homogeneous synthesis gel with a composition of 1 SiO_2/0.067 ZnO/0.105 TPAOH/0.107 Na_2O/14.6 H_2O. The gel was charged into a Teflon-lined autoclave and heated

in a rotating oven at 443 K for 4 days under autogenous pressure. The obtained solid was recovered by centrifugation, washed with distilled water, and dried at 353 K overnight. Then the as-synthesized sample was calcined in 100 mL·min^{-1} synthetic air by 1 K·min^{-1} to 823 K and kept for 18 h. Following this, the zeolite was ion-exchanged with 1.0 M NH_4NO_3 (Sigma Aldrich, ≥99.5%) solution at 353 K for 1 h and separated from the liquid by centrifugation. The same calcination procedure was used to generate the proton form of Zn-MFI.

2.3.3 Ga-BEA (HS)

The Ga-BEA was synthesized according to a method previously reported in [10, 11]. Colloidal silica (LUDOX@AS-40), sodium hydroxide (Sigma Aldrich, >98%), tetraethylammonium hydroxide (Sigma Aldrich, 35 wt.% in water), $Ga(NO_3)_3$ (Alfa Aesar, ≥99.99%) and distilled water were added into a Teflon liner to form a homogeneous gel with a molar composition of 0.2 $(TEA)_2O$:1 SiO_2:0.008 Ga_2O_3:0.1 Na_2O_3:15 H_2O. The pH of the final gel was ~13. Finally, the Teflon liner was introduced into a stainless steel autoclave and heated at 410 K for 8 days. The as-synthesized sample was separated from the liquid by centrifugation, and afterward washed with water and dried at 353 K overnight. Then it was calcined in 100 mL·min^{-1} synthetic air by 1 K·min^{-1} to 823 K and kept for 10 h. Subsequently, it was converted into proton form by ion exchange with 1.0 M NH_4NO_3 (Sigma Aldrich, ≥99.5%) solution at 343 K six times followed by the same calcination procedure as described above.

2.3.4 Ga/Zn-BEA and Ga/Zn-MFI

The Ga/Zn-BEA and Ga/Zn-MFI were prepared via incipient wetness impregnation of the above-prepared proton form zeolites with aqueous $Ga(NO_3)_3$ (Alfa Aesar, ≥99.99%) solution (Table S2.1). The impregnated sample was dried at 353 K overnight and calcined in 100 mL·min^{-1} synthetic air by 5 K·min^{-1} to 823 K and kept for 5 h. They are denoted as Ga/Zn-BEA-X or Ga/Zn-MFI-X, where X refers to the Ga weight content (wt.%) of the sample.

2.3.5 Ga/BEA and Ga/MFI

Ga/BEA and Ga/MFI free of Zn was obtained by reduction of the above prepared Ga/Zn-BEA and Ga/Zn-MFI under 50 mL·min^{-1} H_2 by 15 K·min^{-1} at 823 K for 24 h, during which the Zn was completely leached. Part of Ga was found to be incorporated into the zeolite BEA framework but not MFI. The samples were finally calcined in 100 mL·min^{-1} synthetic air by 5 K·min^{-1} to 823 K and kept for 5 h. They are denoted as Ga/BEA-X and Ga/MFI-X, where X refers to the Ga weight content (wt.%) of the sample.

2.3.6 Pt/Ga-BEA (HS)

The Pt/Ga-BEA (HS) was prepared via incipient wetness impregnation of the above-prepared proton form Ga-BEA (HS) with aqueous $Pt(NH_3)_4 \cdot (NO_3)_2$ (Sigma Aldrich, ≥99.995%%) solution. The impregnated sample was dried at 353 K overnight and calcined in 100 mL·min-1 synthetic air by 5 $K \cdot min^{-1}$ to 823 K and kept for 5 h. They are denoted as Pt/Ga-BEA (HS)-Y, where Y refers to the Pt weight content (wt.%) of the sample.

2.3.7 Y/Zn-BEA

The Y/Zn-BEA was prepared via incipient wetness impregnation of the above-prepared proton form Zn-BEA with aqueous $Y(NO_3)_3$ (Sigma Aldrich, ≥99.99%) solution. The impregnated sample was dried at 353 K overnight and calcined in 100 $mL \cdot min^{-1}$ air by 5 $K \cdot min^{-1}$ to 823 K and kept for 5 h. They are denoted as Y/Zn-BEA-Z, where Z refers to the Y weight content (wt.%) of the sample.

2.4 Chemical and physicochemical characterization

All X-ray diffraction measurements were performed on a PANalytical Empyreal System diffractometer, equipped with a Cu-Kα radiation and operating at 45 kV and 40 mA. The diffractograms were measured using a sample spinner stage in a 2θ range between 5 and 50° under ambient conditions.

The Ga and Zn contents in catalysts were determined by an AA280FS Fast Sequential Atomic Absorption Spectrometer from VARIAN. The acid mixture solution (2% H_2SO_4, 1% HNO_3 and 5% $LaCl_3$) was used to digest the solid samples for Ga and Zn measurement.

Pt contents in catalysts were determined by a Cary 100 UV-Vis Spectrophotometer from Agilent Technologies. Y contents in catalysts were determined by a 700 Series inductively coupled plasma-optical emission spectrometry (ICP-OES) from Agilent technology.

The N_2 sorption measurements were performed using a PMI Automatic Sorptometer. The zeolite samples were outgassed under vacuum at 523 K for 2 h and cooled to liquid N_2 temperature (77 K) before measurement. The micropore volume of zeolites was determined by the *t*-Plot (Lippens and de Boer) method.[12]

The concentration of acid sites on the catalysts was determined by IR spectroscopy of adsorbed pyridine using a Bruker VERTEX 70 IR spectrometer. All the spectra were recorded at specific temperatures under $<10^{-5}$ mbar vacuum. Prior to the pyridine adsorption, a self-supporting

wafer of catalysts was activated in vacuum at 723 K for 1 h (heating rate 15 $K \cdot min^{-1}$). For Zn-BEA, Ga/Zn-BEA, Ga/BEA, Ga-BEA (HS), Pt/Ga-BEA (HS), Zn-MFI, Ga/Zn-MFI and Ga/MFI, pyridine was adsorbed on the catalyst at 313 K with increasing pressure from 10^{-2} to 1 mbar and the final pressure was kept for 1 h until the adsorption equilibrium. Then the spectrum was taken after the cell was outgassed under vacuum at 313 K overnight and at 373, 573 and 723 K for 1 h, respectively. Concentrations of LAS and BAS were determined via quantifications of the bands related to coordinatively adsorbed pyridine (Py-LAS) and protonated pyridine (PyH^+), using molar extinction coefficients of 3.26 and 4.32 $\mu mol \cdot cm^{-2}$, respectively. The LAS/BAS and the strong LAS/BAS (sLAS/sBAS) refer to the sites remaining after evacuation at 373 K and 723 K for 1 h, respectively. For Y/Zn-BEA, differently pyridine was adsorbed at 423 K for 1 h until equilibrium and the LAS/BAS refer to the sites remaining after evacuation at 423 K for 1 h.

2.5 Characterization results

2.5.1 Ga/Zn-BEA and Ga/BEA

All the catalysts are in the crystalline structure of the zeolite BEA, as shown by consistent XRD patterns (Figure 2.1).[13] The Ga impregnation and afterward the removal of Zn under reduction in H_2 did not change their diffractograms. In addition, diffraction peaks of GaO_x and ZnO_x species were not detected.[14, 15]

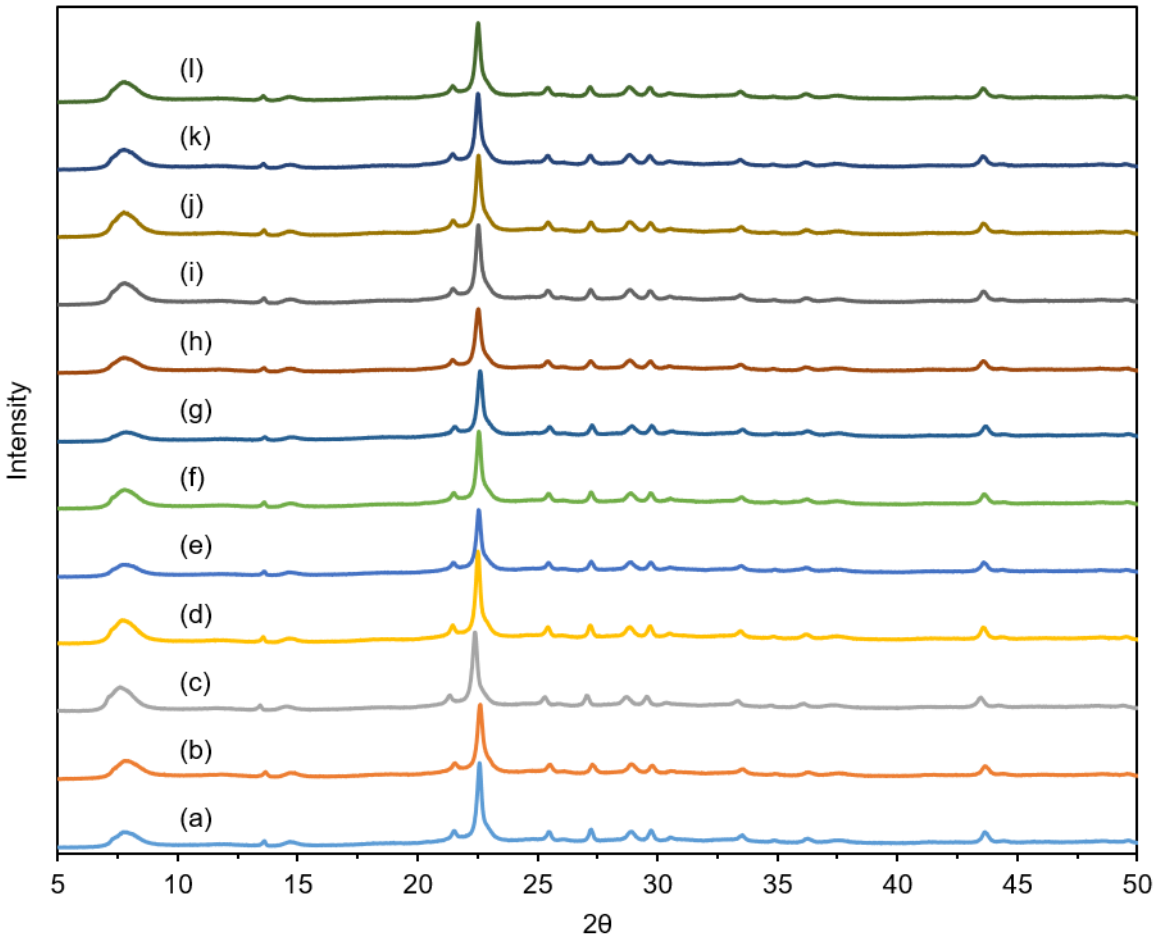

Figure 2.1 XRD patterns of (a) Ga/Zn-BEA-0; (b) Ga-BEA-0; (c) Ga/Zn-BEA-0.7; (d) Ga/Zn-BEA-1.5; (e) Ga/Zn-BEA-1.9; (f) Ga/Zn-BEA-3.0; (g) Ga/Zn-BEA-5.0; (h) Ga/BEA-0.6; (i) Ga/BEA-1.4; (j) Ga/BEA-2.1; (k) Ga/BEA-3.2; (l) Ga/BEA-4.6.

IR spectra of adsorbed pyridine on the zeolites were used to measure qualitatively and quantitatively the acidity of the different samples. Pyridine adsorption on parent Zn-BEA gave characteristic bands at 1452, 1455 cm^{-1} (pyridine interacting with Lewis acid site, Py-LAS), 1444 cm^{-1} (hydrogen-bonded pyridine, Py-H) and 1548 cm^{-1} (pyridinium ions, PyH^{+}) after evacuation at 373 K (Figure 2.2a). The band at 1452 cm^{-1} is attributed to ZnO,[2] formed with a very low content during zeolite calcination. This band was not observed upon evacuation at 723 K. However, the band at 1455 cm^{-1} remained after evacuation at 723 K, indicative of stronger Lewis acidity. It is suggested this band may arise from the lattice Zn site coordinated to the zeolite framework.[2] The small band at 1548 cm^{-1} at 373 K is indicative of BAS-OH interacting with pyridine and it disappeared after evacuation at higher temperature. The parent Zn-BEA contains a much higher amount of LAS (542 $\mu mol \cdot g^{-1}$) than of BAS (28 $\mu mol \cdot g^{-1}$) (Table 2.2).

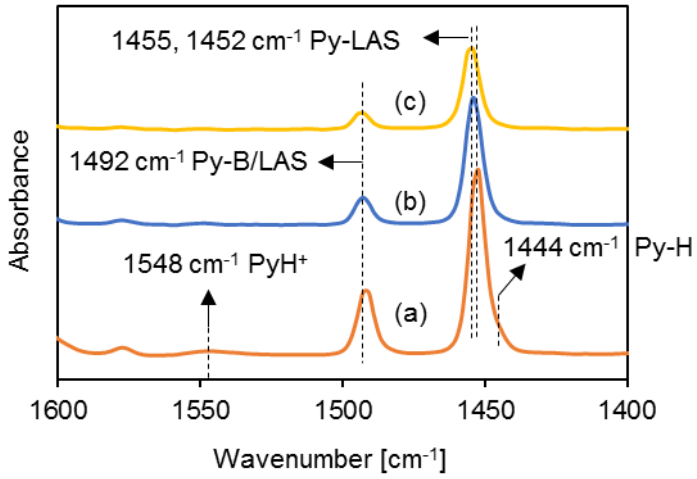

Figure 2.2 IR spectra of pyridine adsorbed on parent Zn-BEA. Evacuation for 1 h at (a) 373 K; (b) 573 K; (c) 723 K. The spectra were the difference spectra of Zn-BEA before and after pyridine adsorption.

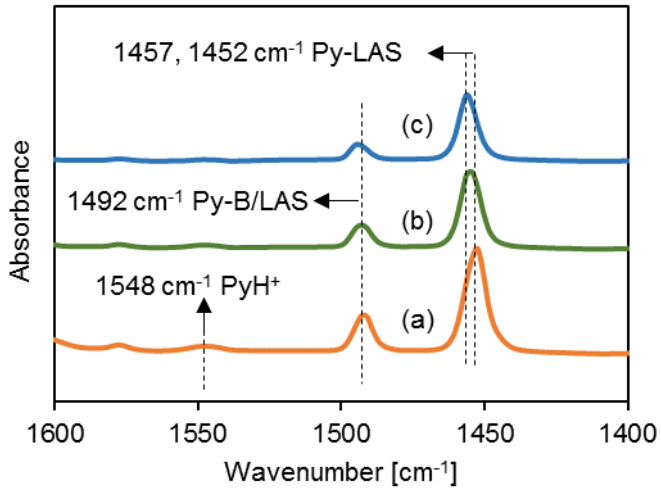

Figure 2.3 IR spectra of pyridine adsorbed on Ga/Zn-BEA-5.0. Evacuation for 1 h at (a) 373 K; (b) 573 K; (c) 723 K. The spectra were the difference spectra of Ga/Zn-BEA-5.0 before and after pyridine adsorption.

Table 2.2 shows the main results of the physicochemical characterization of Ga/Zn-BEA. The BET surface area and micropore volume of Ga/Zn-BEA did not change compared to the parent Zn-BEA. All Ga/Zn-BEA samples have similar micropore volume of 0.13 ± 0.01 $cm^3 \cdot g^{-1}$ and BET surface area of 324 ± 8 $m^2 \cdot g^{-1}$. The effect of Ga impregnation did not cause changes in the zeolite structure. Pyridine adsorption on parent Ga/Zn-BEA-5.0 mainly gave characteristic bands at 1452, 1457 cm^{-1} (Py-LAS) and 1548 cm^{-1} (PyH^+) after evacuation at 373 K (Figure 2.3a). Moreover, the LAS and BAS concentration of all Ga/Zn-BEA also stayed constant with parent Zn-BEA. The Ga sites introduced by incipient wetness impregnation cannot generate BAS, and the introduced Ga may cover some of the original Zn sites to make them inaccessible to pyridine, therefore, the total LAS concentration stayed the same.

Table 2.2 Physical and chemical properties of Ga/Zn-BEA catalysts

Samples[a]	Ga, [wt. %]	BET surface area, [$m^2 \cdot g^{-1}$]	Micropore volume, [$cm^3 \cdot g^{-1}$]	LAS	BAS	sLAS	sBAS
				[$\mu mol \cdot g^{-1}$]			
Ga/Zn-BEA-0	0	332	0.14	542	28	236	5
Ga/Zn-BEA-0.7	0.7	323	0.14	545	40	187	6
Ga/Zn-BEA-1.5	1.5	317	0.13	525	26	223	4
Ga/Zn-BEA-1.9	1.9	325	0.15	519	31	246	6
Ga/Zn-BEA-3.0	3.0	329	0.15	554	40	198	8
Ga/Zn-BEA-5.0	5.0	316	0.15	515	38	277	9

The Zn concentration is around 6 wt.% for all the catalysts from elemental analysis.

Table 2.3 shows the physical and chemical properties of the prepared Ga/BEA catalysts. All the Ga/BEA samples had similar micropore volume of 0.16 ± 0.01 $cm^3 \cdot g^{-1}$ and BET surface area of 355 ± 15 $m^2 \cdot g^{-1}$, demonstrating that different concentrations of Ga did not change these properties. Compared to the corresponding precursors (Ga/Zn-BEA), the BET surface area and micropore volume both increased slightly, *e.g.*, the micropore volume from 0.15 to 0.16 $cm^3 \cdot g^{-1}$ and the BET surface area from 316 to 365 $m^2 \cdot g^{-1}$ for Ga/BEA-4.6. It is hypothesized that the removal of Zn formed silica defects and Ga^{3+} migrated at high temperature to coordinate with the O atoms of neighboring silanols.

Ga/BEA-0 was obtained via H_2 treatment to remove Zn from parent Zn-BEA. Zn was completely leached as shown by the results from elemental analysis. To investigate the structural changes before and after the removal of Zn, the difference IR spectra of Ga/BEA-0 and Ga/BEA-4.6 (before and after Zn removal) are compared in Figure 2.4a and 2.4b. An increase of the broadband at 3508 cm^{-1} and the sharp band at 3745 cm^{-1} were observed after Zn leaching with Ga/BEA-0 (Figure 2.4a (iii)). The bands are assigned to H-bonded internal silanol groups (3508 cm^{-1}) and free silanol groups (3745 cm^{-1}), respectively.[16-18] These observations support the hypothesis of the formation of defect sites by the removal of Zn^{2+}. Pyridine adsorbed on Ga/BEA-0 showed bands of the ring vibrations at 1452 and 1455 cm^{-1} (Py-LAS), 1444 cm^{-1} (Py-H) and 1548 cm^{-1} (PyH^+) after evacuation at 373 K (Figure 2.5). The concentration of LAS and BAS was estimated to be 46 $\mu mol \cdot g^{-1}$ and 10 $\mu mol \cdot g^{-1}$, respectively (Table 2.3).

Table 2.3 Physical and chemical properties of Ga/BEA catalysts

Samples[a]	Ga, [wt.%]	BET surface area, [$m^2 \cdot g^{-1}$]	Micropore volume, [$cm^3 \cdot g^{-1}$]	LAS	BAS	sLAS	sBAS
				[$\mu mol \cdot g^{-1}$]			
Ga/BEA-0	0	355	0.15	46	10	18	5
Ga/BEA-0.6	0.6	370	0.17	135	29	62	8
Ga/BEA-1.4	1.6	356	0.15	132	65	115	27
Ga/BEA-2.1	2.1	351	0.15	155	96	126	21
Ga/BEA-3.2	3.2	341	0.15	175	95	159	20
Ga/BEA-4.6	4.6	365	0.16	220	168	251	72

[a]The original Zn content is 6 wt.% on Ga/Zn-BEA and the remaining Zn content is 0 wt.% for all Ga/BEA from elemental analysis.

With the addition of Ga, major differences were observed in both the IR spectra (Figure 2.4b) and the acid site concentration (Table 2.3). An increase in external silanols (3745 cm^{-1}) and EX Ga-OH species (3690 cm^{-1}) was seen on Ga/BEA-4.6 after Zn leaching. On the contrary to Ga/BEA-0, no change was observed in the internal silanol networks (3508 cm^{-1}) in Figure 2.4b (iii). This suggests that Ga healed the silicon defects of the zeolite framework during Zn leaching. Moreover, a significant amount of BAS (168 $\mu mol \cdot g^{-1}$) was generated with Ga/BEA-4.6, as the incorporation of Ga^{3+} into a lattice defect would lead to the formation of a BAS. This Si-OH-Ga band was observed at 3612 cm^{-1} (Figure S2.1). It appeared at a slightly lower wavenumber than the Ga bridging OH groups in gallosilicate MFI at 3620 cm^{-1},[19] indicating the different environment of Ga incorporated in BEA. It should be noted that Nakai *et al.* prepared high silica Ga-BEA from a dealuminated zeolite, using the dry gel conversion method generating BAS, while this was not observed for Ga impregnated dealuminated zeolite BEA.[20]

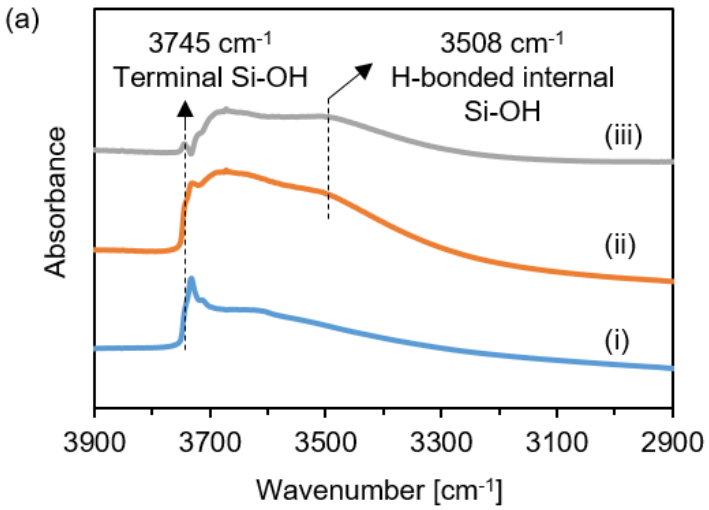

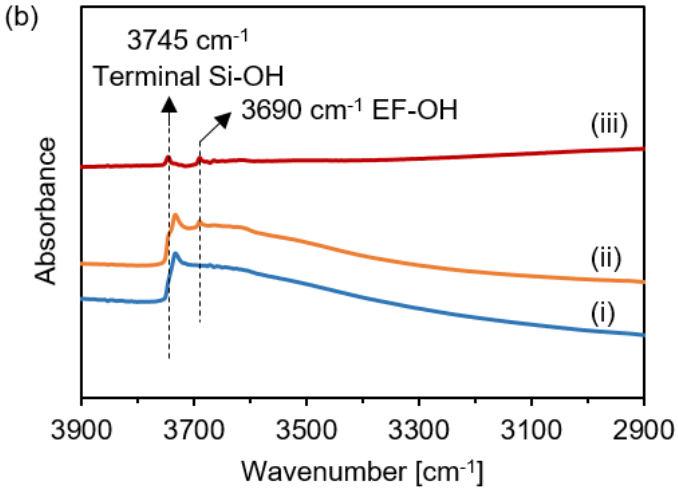

Figure 2.4 (a) IR spectra of (i) Ga/Zn-BEA-0; (ii) Ga/BEA-0 and (iii) subtracted spectra of (i) from (ii); (b) IR spectra of (i) Ga/Zn-BEA-4.6; (ii) Ga/BEA-4.6 and (iii) subtracted spectra of (i) from (ii). The spectra were normalized to the overtone area.

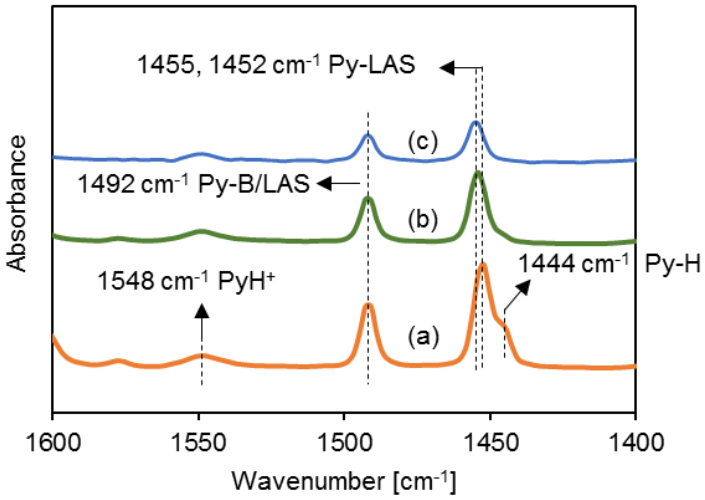

Figure 2.5 IR spectra of adsorbed pyridine on Ga/BEA-0 after evacuation for 1 h at (a) 373 K; (b) 573 K; (c) 723 K. The spectra were the difference spectra of Ga/BEA-0 before and after pyridine adsorption.

The IR spectra of adsorbed pyridine on Ga/BEA-4.6 showed bands at 1446, 1457, 1490 and 1545 cm^{-1} (Figure 2.6), indicating interactions with BAS and LAS. The band at 1457 cm^{-1} (adsorption on Ga^{3+} sites) remained after evacuation at 723 K, indicating a high Lewis acid strength in agreement with the literature.[21, 22] Both the BAS and LAS concentrations increased with Ga loading in zeolite (Table 2.3).

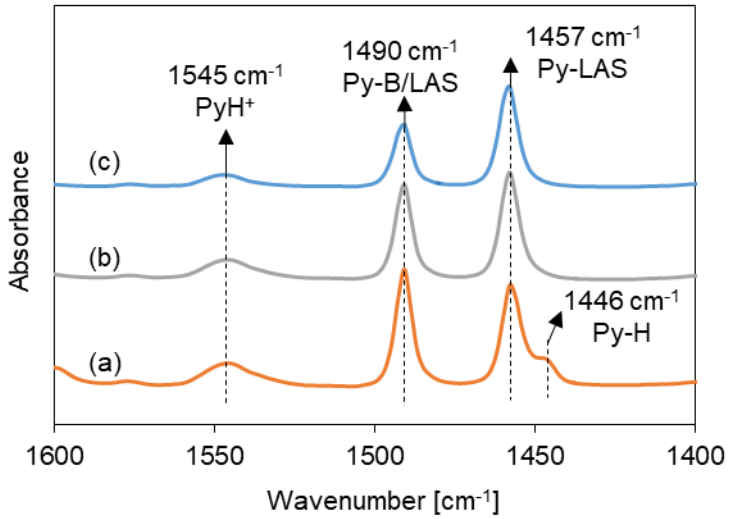

Figure 2.6 IR spectra of adsorbed pyridine on Ga/BEA-4.6 after evacuation for 1 h at (a) 373 K; (b) 573 K; (c) 723 K. The spectra were the difference spectra of Ga/BEA-4.6 before and after pyridine adsorption.

2.5.2 Ga-BEA (HS) and Pt/Ga-BEA (HS)

As expected, the hydroxyl vibration region of IR spectra of Ga-BEA (HS) showed characteristic bands at 3615 (bridging OH group) and 3682 cm^{-1} (hydroxyl groups on the EX-Ga species) (Figure 2.7 a), which is in good agreement with Chao *et al.*[11] It has been reported that the EX-Ga species can be generated by calcination and it was observed on the IR spectrum of evacuated $GaNH_4$-H-BEA that was prepared by Ga ion exchange with NH_4-H-BEA.[23] With pyridine adsorption, the characteristic bands including 1457 cm^{-1} (Py-LAS), 1444 cm^{-1} (Py-H or pyridine sorbed on EX-GaO_x, Py-GaO_x)[24] and 1547 cm^{-1} (PyH^+) were observed after evacuation at 373 K (Figure 2.7). The concentration of LAS and BAS were 440 $\mu mol \cdot g^{-1}$ and 560 $\mu mol \cdot g^{-1}$, respectively (Table 2.4), and particularly large percentages of BAS (70%) and LAS (99%) were proved to be sBAS and sLAS. Both acid site concentrations were much higher than that in Ga/BEA-4.6 catalyst with the same Ga content. Therefore, more Ga sites were incorporated to generate BAS during hydrothermal synthesis. The concentration of BAS and LAS were above the total Ga concentration (660 $\mu mol \cdot g^{-1}$) in the zeolite.

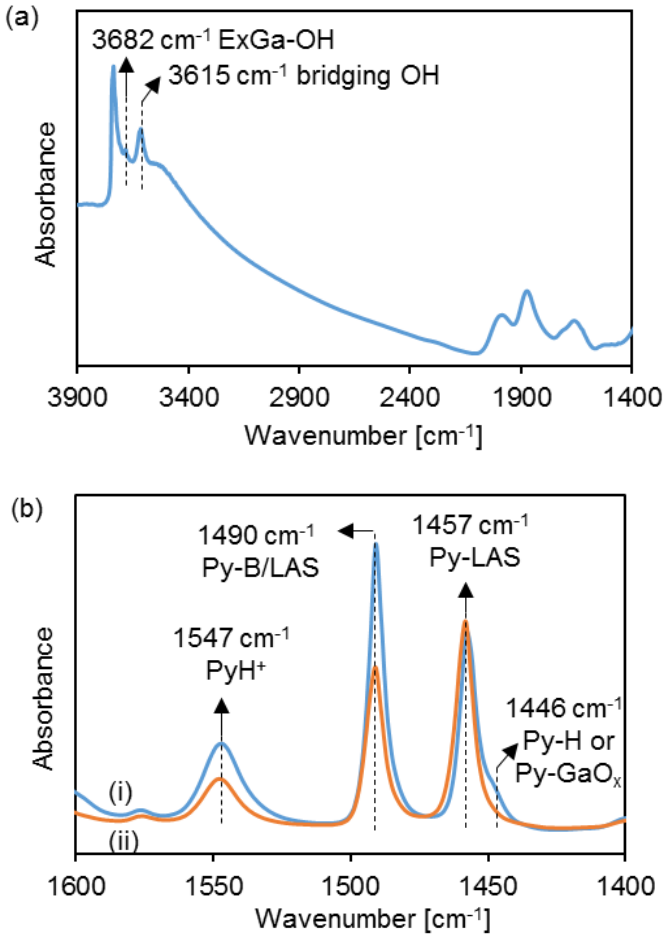

Figure 2.7 IR spectra of Ga/BEA (HS) (a) after activation; (b) adsorbed pyridine after evacuation for 1 h at (i) 423 K and (ii) 723 K. The spectra were the difference spectra of Ga/BEA (HS) before and after pyridine adsorption.

The BAS and LAS concentrations on Pt/Ga-BEA (HS) were also estimated by IR spectroscopy of adsorbed pyridine (Table 2.4). The BAS concentration decreased with Pt loading, suggesting that Pt might cover some acid sites and hindered their interactions with pyridine. Another possibility would be that some tetrahedrally coordinated framework Ga sites became partial or total EX-Ga sites or GaO_x clusters during the calcination after Pt addition, leading to lower BAS concentration.[25] Differently, the LAS was kept in a similar concentration after Pt addition. The sLAS concentration appeared to be a little higher than the LAS concentration and this could be due to the errors from the deconvolution of the bands at 1457 and 1446 cm^{-1} (Figure 2.7b).

Table 2.4 Acid site concentration of (Pt/)Ga-BEA (HS) catalysts

Samples	Ga content		Pt content [wt.%]	LAS[a]	BAS	sLAS	sBAS
	[wt.%]	[μmol·g^{-1}]		[μmol·g^{-1}]			
Ga-BEA (HS)			0	440	560	436	393
Pt/Ga-BEA (HS)-0.1	4.6	660	0.1	470	504	475	338
Pt/Ga-BEA (HS)-0.2			0.2	445	440	460	306

[a]The LAS concentration only refers to the band at 1457 cm^{-1}.

2.5.3 Ga/Zn-MFI and Ga/MFI

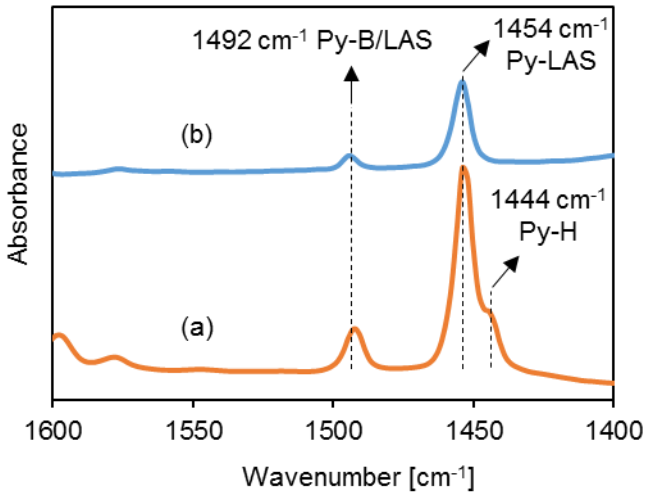

Figure 2.8 IR spectra of adsorbed pyridine on Zn-MFI after evacuation for 1 h at (a) 373 K; (b) 723 K. The spectra were the difference spectra of Zn-MFI before and after pyridine adsorption.

Table 2.5 Physical and chemical properties of MFI catalysts

Samplesa	Ga [wt.%]	Zn [wt.%]	LAS	BAS	sLAS	sBAS
			[μmol·g^{-1}]			
Zn-MFI	0	3.1	208	0	82	
Ga/Zn-MFI-2.7	2.7	3.1	190	0	55	0
Ga/MFI-1.2	1.2	0	29	0	13	0

The acid site characteristics of Zn-MFI prepared via direct hydrothermal synthesis were also measured by IR spectroscopy of adsorbed pyridine (Figure 2.8). Similar to Zn-BEA, Zn-MFI contained only LAS and no BAS, with characteristic bands at 1454 cm^{-1} (Py-LAS) and 1444 cm^{-1} (Py-H). With lower Zn content (3 wt.% compared to 6 wt.% in Zn-BEA), the LAS concentration was also around half as that in Zn-BEA (Table 2.5).

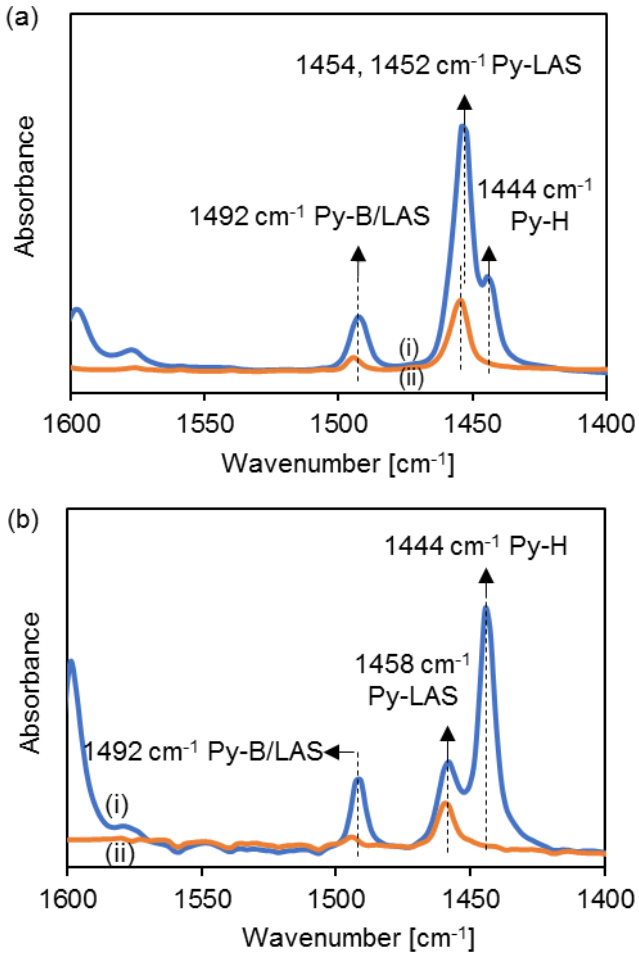

Figure 2.9 IR spectra of adsorbed pyridine on (a) Ga/Zn-MFI-2.7 and (b) Ga/MFI-1.2 after evacuation for 1 h at (i) 373 K; (ii) 723 K. The spectra were the difference spectra of zeolites before and after pyridine adsorption.

With the addition of Ga, the LAS and BAS concentration did not change. Three bands at 1452, 1454 cm^{-1} (Py-LAS) and 1444 cm^{-1} (Py-H) were observed on Ga/Zn-MFI-2.7 (Figure 2.9a). Different from the incorporation of Ga into zeolite framework in Zn-BEA during H_2 treatment, both Ga and Zn were found to be leached during H_2 treatment. Ga and Zn contents decreased from 2.7 wt.% and 3.1 wt.% to 1.2 wt.% and 0 wt.% respectively from Ga/Zn-MFI-2.7 to Ga/MFI-1.2. No BAS was generated and the LAS concentration decreased from 190 to 29 $\mu mol \cdot g^{-1}$ on Ga/MFI-1.2 (Figure 2.9b). Ga_2O is volatile above 473 K and it can be formed during the reduction of Ga oxides in H_2 treatment,[26] therefore it might be the reason for Ga leaching from Ga/Zn-MFI-2.7. Correspondingly, a large band at 1444 cm^{-1} was observed on Ga/MFI-1.2 (Figure 2.9b), which could be from the H-bonded pyridine by silanol nests formed after Zn removal. A band at 1458 cm^{-1} (Py-LAS) was observed on Ga/MFI-1.2, which could be from the EX-Ga sites in zeolites.[21, 22] However, only 13% of these LAS remained after evacuation at 723 K compared with 91% in Ga/Zn-BEA-3.2, indicating the different strength of these Ga acidic sites in MFI and BEA zeolites. H_2 treatment had different impacts on Ga/Zn-

MFI and Ga/Zn-BEA. The different framework environments led to different nature, locations and concentrations of acid sites.

2.5.4 Y/Zn-BEA

The crystalline structure of all Y/Zn-BEA zeolites was confirmed using powder XRD as shown in Figure 2.10.[13] The diffractograms of BEA zeolite did not change upon Y impregnation. In addition, diffraction peaks of Y_2O_3 and ZnO_x species were not detected.[14, 27] All the Y/Zn-BEA samples had similar BET surface area of 337 ± 19 $m^2 \cdot g^{-1}$ and microspore volume of 0.15 ± 0.01 $cm^3 \cdot g^{-1}$, showing that different loadings of Y did not change these morphological properties.

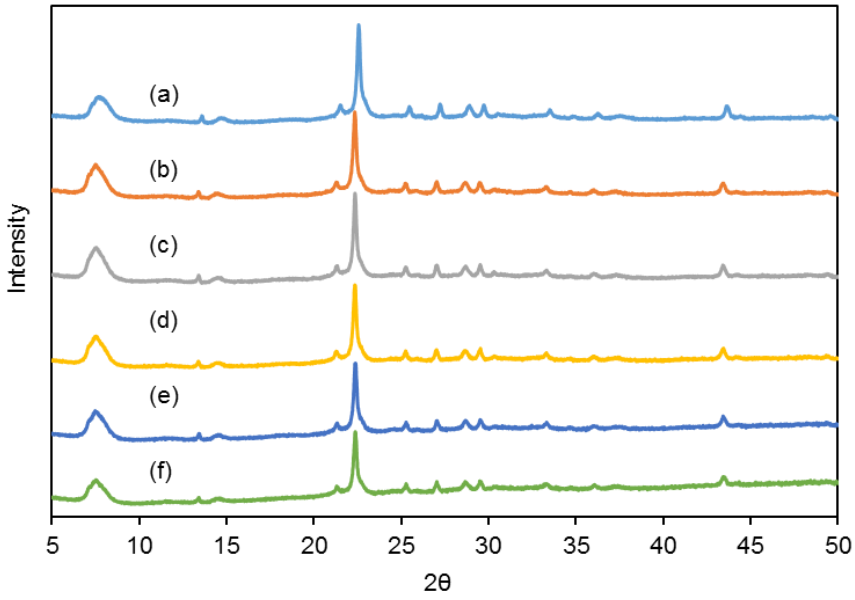

Figure 2.10 XRD patterns of all the materials. (a) Y/Zn-BEA-0; (b) Y/Zn-BEA-0.6; (c) Y/Zn-BEA-1.2; (d) Y/Zn-BEA-2.2; (e) Y/Zn-BEA-4.3; (f) Y/Zn-BEA-6.4.

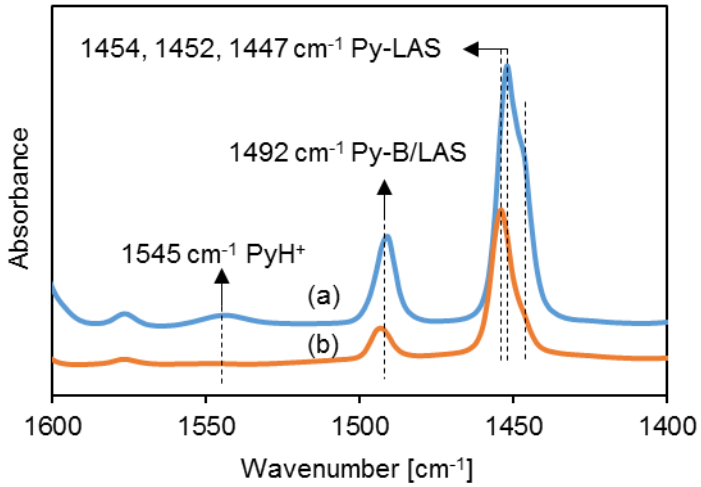

Figure 2.11 IR spectra of adsorbed pyridine on Y/Zn-BEA-2.2 after evacuation for 1 h at (a) 423 K; (b) 723 K. The spectra were the difference spectra of Y/Zn-BEA-2.2 before and after pyridine adsorption.

The IR spectra of pyridine adsorbed Y/Zn-BEA-2.2 (Figure 2.11) had characteristic bands at 1545, 1492, 1454, 1452 and 1447 cm^{-1}. The band at 1545 cm^{-1} and 1492 cm^{-1} were from Py-BAS and Py-B/LAS. The bands at 1454 and 1452 cm^{-1} were attributed to pyridine adsorbed Lewis acid Zn sites compared with the spectra of parent Zn-BEA. The H-bonded pyridine and Lewis acid Y sites interacting with pyridine can both show a band at around 1447 cm^{-1},[28] however, this band partly remained after evacuation at 723 K, showing a strong acidity different from the H-bonded pyridine. It increased with the loading of Y from 0.6 to 6.4 wt.% (Figure S2.7). It was also barely visible on the parent Zn-BEA, therefore, it was assigned to pyridine interacting with Y Lewis acid sites. In general, the LAS concentration increased with Y loading (Table 2.6), which can also be seen from the increase of the band at 1447 cm^{-1} on different Y/Zn-BEA samples in Figure S2.7. The BAS concentration of Y/Zn-BEA was slightly higher than that of parent Zn-BEA, and it increased slightly with increasing Y loading.

Table 2.6 Physical and chemical properties of Y/Zn-BEA catalysts

Samples[a]	Y [wt.%]	BET surface area, [$m^2 \cdot g^{-1}$]	Microspore volume, [$cm^3 \cdot g^{-1}$]	LAS[b]	BAS	sLAS[c]	sBAS
				[$\mu mol \cdot g^{-1}$]			
Y/Zn-BEA-0	0	332	0.14	492	23	236	5
Y/Zn-BEA-0.6	0.6	348	0.15	456	25	216	0
Y/Zn-BEA-1.2	1.2	355	0.16	534	40	259	0
Y/Zn-BEA-2.2	2.2	337	0.14	590	45	297	0
Y/Zn-BEA-4.3	4.3	332	0.15	637	38	288	0
Y/Zn-BEA-6.4	6.4	318	0.14	668	60	294	0

[a]The Zn content is 6 wt.% on Y/Zn-BEA

[b]The LAS and BAS concentrations were determined after evacuation at 423 K for 1 h.

[c]The sLAS and sBAS concentrations were determined after evacuation at 723 K for 1 h.

2.5.5 H-BEA

H-BEA-5 (Si/Al=5) and H-BEA-75 (Si/Al=75) were purchased from Süd Chemie company and tested as reference samples for ethanol conversion. Their acid site concentration was determined by IR spectroscopy of adsorbed pyridine (Table 2.7, Figures S2.5 and S2.6). As expected, H-BEA-5 with a lower Si/Al ratio had much more acid sites than H-BEA-75 and both catalysts had more BAS than LAS. A large percentage of these acid sites have high acidic strength (except for the LAS in H-BEA-75) as the bands mostly remained after evacuation at 723 K for 1 h.

Table 2.7 Acid site concentration of H-BEA catalysts

Samples	Si/Al	LASa	BAS	sLASb	sBAS
		[µmol·g^{-1}]			
H-BEA-5	5	483	1148	489	810
H-BEA-75	75	60	126	18	117

[a]The LAS and BAS concentrations were determined after evacuation at 423 K for 1 h.

[b]The sLAS and sBAS concentrations were determined after evacuation at 723 K for 1 h.

2.6 Conclusion

A series of zeolites including Zn-BEA, Zn-MFI and Ga-BEA (HS) were synthesized successfully. Subsequent addition of Ga on Zn-BEA and Zn-MFI, Pt on Ga-BEA (HS) and Y on Zn-BEA via incipient wetness impregnation produced Ga/Zn-BEA, Ga/Zn-MFI, Pt/Ga-BEA (HS) and Y/Zn-BEA. With further reduction of Ga/Zn-BEA by H_2, complete Zn leaching occurred and Ga/BEA was finally obtained. Different from Ga/Zn-BEA, the leaching of both Ga and Zn occurred during the H_2 treatment of Ga/Zn-MFI. With the addition of these metals in zeolites, no obvious changes on the diffractograms, BET surface area and micropore volume were observed.

With H_2 treatment on Ga/Zn-BEA, the diffractograms did not change while the specific surface area and the microspore volume increased a bit. It indicated small changes in the zeolite structure, as the removal of Zn generated more silicon defects and Ga migration occurred at high temperature. With further measurement of pyridine adsorbed IR, the parent Zn-BEA has 542 $\mu mol \cdot g^{-1}$ LAS and 28 $\mu mol \cdot g^{-1}$ BAS. All Ga/Zn-BEA have similar BAS and LAS concentrations with respect to Zn-BEA. Ga addition did not affect the BAS or LAS concentration. With H_2 treatment to remove the Zn, only 46 $\mu mol \cdot g^{-1}$ LAS and 10 $\mu mol \cdot g^{-1}$ BAS were measured on H_2 treated Zn-BEA (that is Ga/BEA-0). On the contrary, a significant amount of BAS was found on Ga/BEA-X (X=0.6-4.6 wt.%), for example, 175 $\mu mol \cdot g^{-1}$ LAS and 95 $\mu mol \cdot g^{-1}$ BAS on Ga/BEA-3.2. The difference in the hydroxyl region of the Ga/Zn-BEA and Zn-BEA before and after H_2 treatment also indicated the incorporation of Ga into the zeolite framework, leading to the generation of BAS. The BAS and LAS concentration increased linearly with the increasing Ga loading on Ga/BEA catalysts. For comparison, the synthesized Zn-MFI showed 208 $\mu mol \cdot g^{-1}$ LAS and no BAS. The Ga-BEA (HS) with the same Ga content (4.6 wt.%) as Ga/BEA-4.6 (220 $\mu mol \cdot g^{-1}$ LAS and 168 $\mu mol \cdot g^{-1}$ BAS) was found to have 440 $\mu mol \cdot g^{-1}$ LAS and 560 $\mu mol \cdot g^{-1}$ BAS, suggesting that more Ga was incorporated into the framework to generate BAS during hydrothermal synthesis.

Looking at the Y/Zn-BEA, low BAS concentration was found on all Y/Zn-BEA while it increased slightly with the addition of Y. Three main LAS showed characteristic bands with pyridine adsorption at 1454, 1452 and 1447 cm^{-1}. The former two were assigned to pyridine adsorbed Zn sites and the latest one was assigned to pyridine adsorbed Y sites whose intensity increased with Y loading. Correspondingly, the LAS concentration of Y/Zn-BEA increased gradually with Y loading.

2.7 Appendix

Table S2.1. Ga content in Ga/BEA and Ga/MFI catalysts

Samples	Introduced Ga content [wt.%]	Final Ga content from elemental analysis [wt.%]
Ga/BEA-0.6	0.6	0.6
Ga/BEA-1.4	1.6	1.4
Ga/BEA-2.1	2.1	2.1
Ga/BEA-3.2	3.2	3.2
Ga/BEA-4.6	4.8	4.6
Ga/MFI-1.2	3.2	1.2

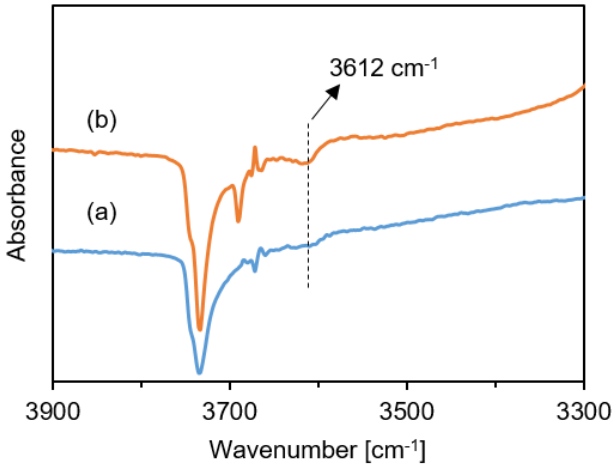

Figure S2.1. IR spectra of pyridine adsorbed at 313 K on (a) Ga/Zn-BEA-4.6; (b) Ga/BEA-4.6. The spectra were obtained by subtracting the spectrum taken after activation from the spectrum taken after pyridine adsorption. The band at 3612 cm^{-1} disappeared after pyridine adsorption and it can be seen more obviously from the decrease of the band on these subtracted spectra.

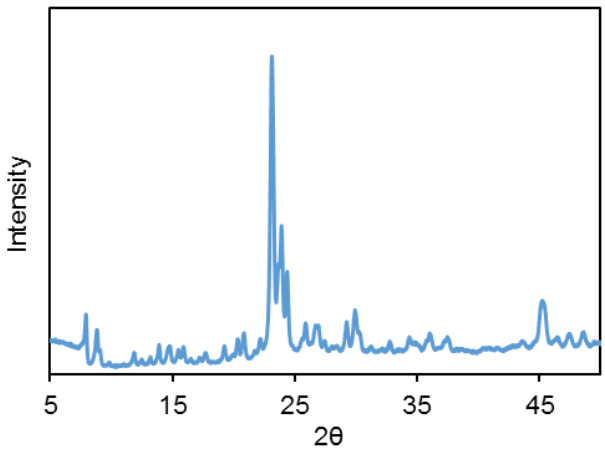

Figure S2.2 XRD patterns of as-synthesized Zn-MFI.

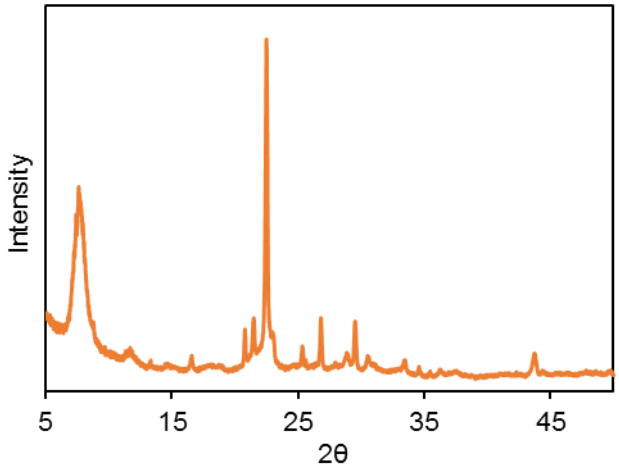

Figure 2.4 XRD patterns of as-synthesized Ga-BEA (HS).

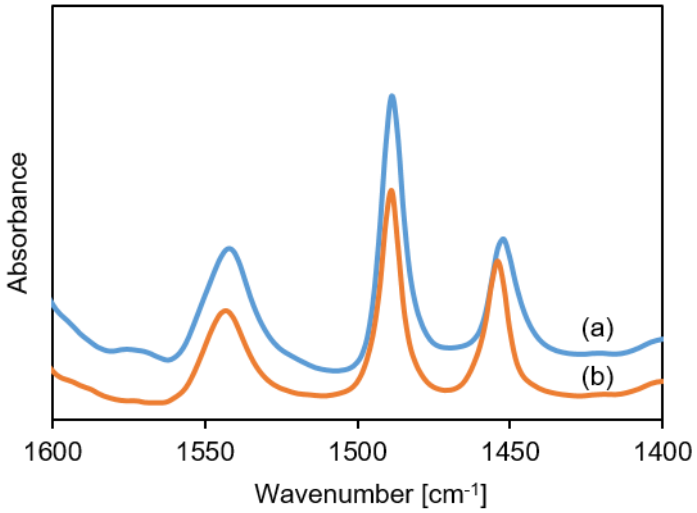

Figure S2.5 IR spectra of adsorbed pyridine on H-BEA-5 after evacuation for 1 h at (a) 423 K; (b) 723 K. The spectra were the difference spectra of H-BEA-5 before and after pyridine adsorption.

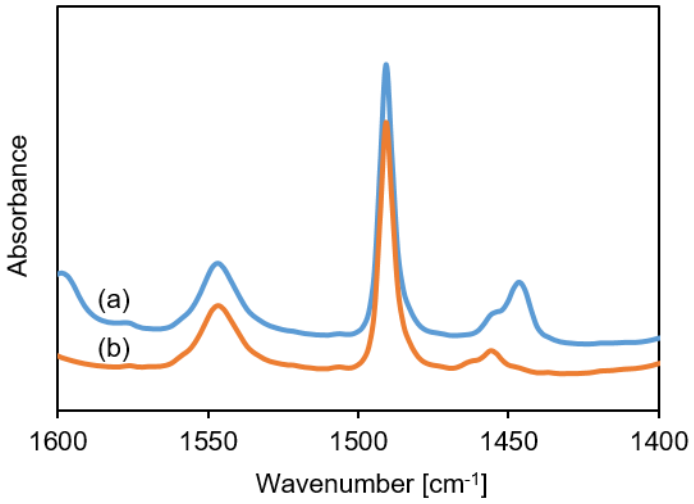

Figure S2.6 IR spectra of adsorbed pyridine on H-BEA-75 after evacuation for 1 h at (a) 423 K; (b) 723 K. The spectra were the difference spectra of H-BEA-75 before and after pyridine adsorption.

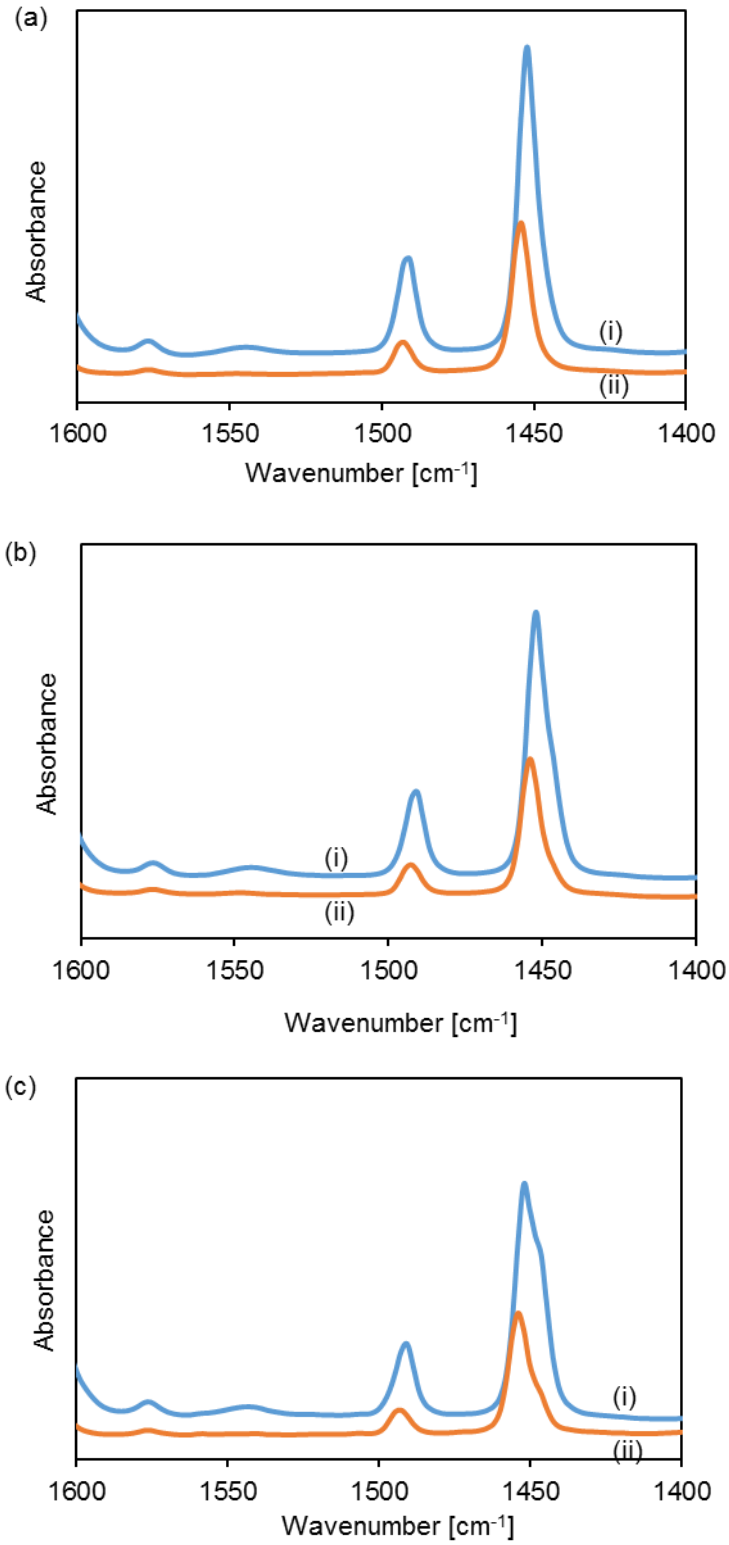
(a)
Absorbance
(i)
(ii)
1600
1550
1500
1450
1400
Wavenumber [cm-1]
(b)
Absorbance
(i)
(ii)
1600
1550
1500
1450
1400
Wavenumber [cm-1]
(c)
Absorbance
(i)
(ii)
1600
1550
1500
1450
1400
Wavenumber [cm-1]

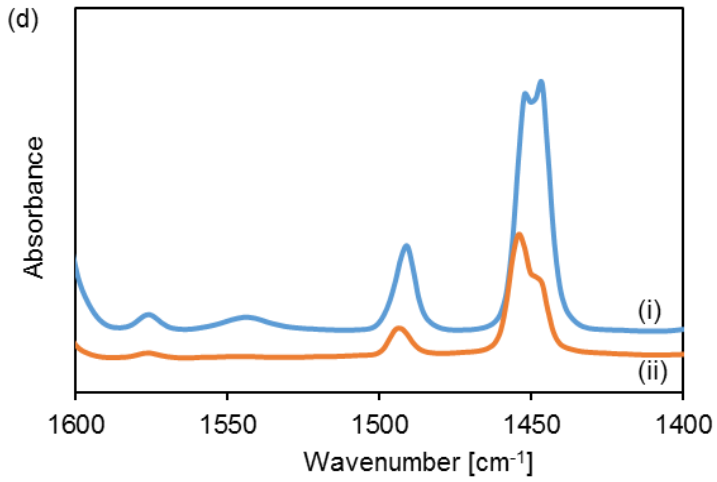

Figure S2.7 IR spectra of adsorbed pyridine on Y/Zn-BEA-X (a) X=0.6; (b) X=1.2; (c) X=4.3; (d) X=6.4 after evacuation for 1 h at (i) 423 K; (ii) 723 K. The spectra were the difference spectra of Y/Zn-BEA-X before and after pyridine adsorption.

2.8 Reference

[1] Y. Sakamoto, H. Zhao, H. Gies, K. Yamamoto, U. Kolb, T. Ikeda, A new microporous 12-ring zincosilicate THK-2 with many terminal silanols characterized by automated electron diffraction tomography, Dalton Transactions, 49 (2020) 12960-12969.

[2] M. Orazov, M.E. Davis, Catalysis by framework zinc in silica-based molecular sieves, Chemical Science, 7 (2016) 2264-2274.

[3] J. Cejka, A. Corma, S. Zones, Zeolites and catalysis: synthesis, reactions and applications, John Wiley & Sons2010.

[4] P. Behrens, E. Brunner, H. Förster, E. Geidel, W. Grünert, R. Heidler, M. Hunger, H. Karge, L. Rees, R. Schlögl, Characterization I, Springer Science & Business Media 2004.

[5] M.A. Makarova, J. Dwyer, FTIR analysis of the hydroxyl region in US-Y zeolites, The Journal of Physical Chemistry, 97 (1993) 6337-6338.

[6] E. Parry, An infrared study of pyridine adsorbed on acidic solids. Characterization of surface acidity, Journal of Catalysis, 2 (1963) 371-379.

[7] T. Barzetti, E. Selli, D. Moscotti, L. Forni, Pyridine and ammonia as probes for FTIR analysis of solid acid catalysts, Journal of the Chemical Society, Faraday Transactions, 92 (1996) 1401-1407.

[8] R. Buzzoni, S. Bordiga, G. Ricchiardi, C. Lamberti, A. Zecchina, G. Bellussi, Interaction of pyridine with acidic (H-ZSM5, H-β, H-MORD zeolites) and superacidic (H-Nafion membrane) systems: An IR investigation, Langmuir, 12 (1996) 930-940.

[9] P. Andy, M.E. Davis, Dehydrogenation of Propane over Platinum Containing CIT-6, Industrial & Engineering Chemistry Research, 43 (2004) 2922-2928.

10] A.-C. Wei, P.-H. Liu, K.-J. Chao, E. Yang, H.-Y. Cheng, X-ray absorption measurement and density functional theory analysis of gallium in gallium-containing beta zeolites, Microporous and Mesoporous Materials, 47 (2001) 147-156.

[11] K.J. Chao, S.P. Sheu, L.-H. Lin, M.J. Genet, M.H. Feng, Characterization of incorporated gallium in beta zeolite, Zeolites, 18 (1997) 18-24.

[12] B.C. Lippens, J.H. de Boer, Studies on pore systems in catalysts: V. The t method, Journal of Catalysis, 4 (1965) 319-323.

[13] M.A. Deimund, J. Labinger, M.E. Davis, Nickel-Exchanged Zincosilicate Catalysts for the Oligomerization of Propylene, ACS Catalysis, 4 (2014) 4189-4195.

[14] A.K. Zak, R. Razali, W.H. Abd Majid, M. Darroudi, Synthesis and characterization of a narrow size distribution of zinc oxide nanoparticles, International Journal of Nanomedicine, 6 (2011) 1399.

[15] E. Huang, J. Li, G. Wu, W. Dai, N. Guan, L. Li, A simple synthesis of Ga_2O_3 and GaN nanocrystals, RSC Advances, 7 (2017) 47898-47903.

[16] A. Jentys, G. Rumplmayr, J.A. Lercher, Hydroxyl-Groups in Phosphorus-Modified HZSM-5, Applied Catalysis, 53 (1989) 299-312.

[17] A. Jentys, G. Mirth, J. Schwank, J.A. Lercher, Interaction of Hydrocarbons and Water with ZSM-5, Studies in Surface Science and Catalysis, 49 (1989) 847-855.

[18] J.i. Čejka, A. Corma, S. Zones, Zeolites and catalysis: synthesis, reactions and applications, Wiley-VCH, Weinheim, 2010.

[19] C.T.W. Chu, C.D. Chang, Isomorphous substitution in zeolite frameworks. 1. Acidity of surface hydroxyls in [B]-, [Fe]-, [Ga]-, and [Al]-ZSM-5, The Journal of Physical Chemistry, 89 (1985) 1569-1571.

[20] M. Nakai, K. Miyake, R. Inoue, K. Ono, H. Al Jabri, Y. Hirota, Y. Uchida, S. Tanaka, M. Miyamoto, Y. Oumi, C.Y. Kong, N. Nishiyama, Dehydrogenation of propane over high silica *BEA type gallosilicate (Ga-Beta), Catalysis Science & Technology, 9 (2019) 6234-6239.

[21] S.-W. Choi, W.-G. Kim, J.-S. So, J.S. Moore, Y. Liu, R.S. Dixit, J.G. Pendergast, C. Sievers, D.S. Sholl, S. Nair, C.W. Jones, Propane dehydrogenation catalyzed by gallosilicate MFI zeolites with perturbed acidity, Journal of Catalysis, 345 (2017) 113-123.

[22] J.-G.E. Victor de O. Rodrigues, and Arnaldo C. Faro, Jr., Correlations between Dispersion, Acidity, Reducibility, and Propane Aromatization Activity of Gallium Species Supported on HZSM-5 Zeolites, The Journal of Physical Chemistry C, 114 (2010) 4557-4567.

[23] R.B. Borade, A. Clearfield, Characterization of acid sites in Beta and ZSM-20 zeolites, The Journal of Physical Chemistry, 96 (1992) 6729-6737.

[24] M.W. Schreiber, C.P. Plaisance, M. Baumgärtl, K. Reuter, A. Jentys, R. Bermejo-Deval, J.A. Lercher, Lewis-Brønsted acid pairs in Ga/H-ZSM-5 to catalyze dehydrogenation of light alkanes, Journal of the American Chemical Society, 140 (2018) 4849-4859.

[25] C. Otero Areán, G. Turnes Palomino, F. Geobaldo, A. Zecchina, Characterization of gallosilicate MFI-type zeolites by IR spectroscopy of adsorbed probe molecules, The Journal of Physical Chemistry, 100 (1996) 6678-6690.

[26] T. Akatsu, A. Plößl, H. Stenzel, U. Gösele, GaAs wafer bonding by atomic hydrogen surface cleaning, Journal of Applied Physics, 86 (1999) 7146-7150.

[27] D. Avram, B. Cojocaru, M. Florea, C. Tiseanu, Advances in luminescence of lanthanide doped Y_2O_3: case of S 6 sites, Optical Materials Express, 6 (2016) 1635-1643.

[28] L. Qi, Y.F. Zhang, M.A. Conrad, C.K. Russell, J. Miller, A.T. Bell, Ethanol Conversion to Butadiene over Isolated Zinc and Yttrium Sites Grafted onto Dealuminated Beta Zeolite, Journal of the American Chemical Society, 142 (2020) 14674-14687.

Chapter 3

3. Highly active and selective sites for propane dehydrogenation in zeolite Ga/BEA

3.1 Abstract

Highly selective Ga-modified zeolite BEA for propane dehydrogenation have been prepared via grafting Ga on Zn-BEA followed by removal of Zn via reduction by H_2. An 82 % propene selectivity was achieved at 19 % propane conversion at 813 K. Based on the kinetic analysis, a model of the catalytic cycle was established based on elementary steps of propane adsorption, first C-H bond cleavage, β-H transfer, propene desorption and H_2 desorption. The propane dehydrogenation rate is determined by the C-H bond cleavage of propane at low pressures, however, at high pressure, the rate is limited by desorption of H_2 from the catalytic site. The concentration of active sites was quantified by the reversible adsorption and desorption of H_2 on catalysts. For comparison, Ga-BEA (HS) from hydrothermal synthesis and Pt/Ga-BEA (HS) were also tested. Ga-BEA (HS) showed comparable activity as Ga/BEA and the addition of Pt greatly improved the propane dehydrogenation activity.

3.2 Introduction

Propene is a key raw material in the chemical industry for the production of a wide variety of products.[1] The dehydrogenation of propane (PDH) has attracted growing interest due to the surges in hydrocarbon production from shale gas. As the key reaction step appears to be the cleavage of the first C-H bond of propane, Cr- and Pt-based catalysts are widely used in commercially implemented processes (*e.g.*, Catofin & Oleflex processes).[2, 3] However, rapid deactivation and limited propene selectivity restrict their applications.

The substitution of Ga^{3+} for Al^{3+} in MFI and the addition of Ga-oxide nanoclusters is highly effective for dehydrogenation but also leads to substantial cyclization and aromatization.[4-6] Schreiber *et al*. showed the formation of homotopic Lewis-Brønsted acid pairs in Ga/ZSM-5,[7] formed by the interaction of a BAS with a Ga^{+}, replacing another BAS, led to an increase of two orders of magnitude in PDH rate, with respect to parent H-ZSM-5. Diverse synthetic methods have been extensively studied to incorporate Ga into zeolites,[7-15] suggesting a variety of Ga active species both experimentally and theoretically.[16-24] Although the catalytic activity of these supported Ga catalysts for PDH has been extensively explored, the nature of their active metal sites is often a point of contention. Isolated BAS and isolated Ga cations tend to catalyze secondary reactions, such as dimerization and aromatization, decreasing the propene selectivity with propane conversion.[25-27] The challenge for catalyst synthesis lies, therefore, in combining highly active sites with blocking C-C bond cleavage and oligomerization.

In a quest to synthesize materials with highly uniform active sites, we chose the zeolite framework BEA substituted with Zn as the parent material. Ga^{3+} cations have been introduced via incipient wetness impregnation. The synthesis strategy allowed to replace Zn with Ga leading to Ga Lewis and Brønsted acid sites. Zn is removed in this approach via reduction at elevated temperatures, leading to gradual vapor phase removal. The nature and concentration of these Ga^{3+} sites are probed by IR spectroscopy of adsorbed pyridine and *in situ* H_2 temperature-programed desorption. The effects of Ga^{3+} sites on PDH in terms of activity, selectivity as well as reaction mechanism are investigated by kinetic studies, isotopic experiments and operando propane uptake measurements, without, however, being able to atomistically define the active sites. Finally, Ga-BEA (HS) from hydrothermal synthesis and Pt/Ga-BEA (HS) were also tested on PDH for comparison.

3.3 Experimental

Catalyst resting

The catalysts were tested for PDH reaction in a fixed bed plug flow reactor, consisting of a quartz glass tube with 4 mm inner diameter. In a typical test, 10 mg of the catalyst with particle size of 180-300 μm mixed with SiC (250-500 μm) was loaded in the middle of a quartz tube supported between two quartz wool plugs. Prior to the reaction, the catalyst was pre-dried *in situ* under 10 $mL \cdot min^{-1}$ He at 823 K for 1 h. Subsequently, the reaction was carried out at 1 bar total pressure (with He as a carrier gas) with a total flow rate of 5-100 $mL \cdot min^{-1}$ (weight hour space velocity, WHSV: 0.21~106 $g_{C_3H_8} \cdot g_{cat}^{-1} \cdot h^{-1}$) at 813 K. The pressure of propane ($p_{C_3H_8}$) was in the range of 2-100 mbar. The products were detected with an online Agilent 6890 series gas chromatograph (GC) equipped with an HP-PLOT/Q column (30 m × 0.320 mm) and an FID detector. The conversion of propane and yield of products were calculated based on the peak areas from GC analysis. The cracking rate was determined based on the concentration of produced methane, and the dehydrogenation rate was determined based on the concentration of produced propene.

Kinetic isotopic experiment

C_3D_8 (Sigma Aldrich, 99 atom% D) was used for the measurements of the kinetic isotope effect (KIE). The experiments were performed by the same reaction procedure as section 2.3 at 2, 20, 40, 60 and 100 mbar of $p_{C_3H_8}$ or $p_{C_3D_8}$ at 813 K. The reactant was switched from C_3H_8 to C_3D_8 after 21 h time on stream (TOS) until the reaction was in a steady state. The samples were taken every 30 min in 2 h by GC and the switch between C_3H_8 and C_3D_8 was subsequently repeated and further carried out at different pressure.

Temperature-programed desorption of H_2

The desorption experiment of H_2 was carried out directly in the same fixed-bed reactor and the desorbed H_2 was analyzed by an online mass spectrometer. Typically, 50 mg catalyst were first pre-dried in 10 $mL \cdot min^{-1}$ He at 823 K for 1 h and then cooled to liquid N_2 temperature in a liquid N_2 bath. Then, at liquid N_2 temperature, the adsorption of H_2 was started by switching the gas from He to 15 $mL \cdot min^{-1}$ H_2 and kept for 15 min. Afterward, the gas was switched back to 30 $mL \cdot min^{-1}$ He to flash the catalysts for half an hour. Then the liquid N_2 bath was removed and the temperature of the reactor increased to room temperature gradually. Subsequently, the reactor was heated to 813 K by 30 $K \cdot min^{-1}$ and kept for 30 min and finally cooled to room temperature.

Propane adsorption

The heat of adsorption of propane on Ga/BEA-3.2 was measured with a Setaram TG-DSC 111 calorimeter connected to a high vacuum system. The catalyst (about 20 mg) was placed in a quartz crucible and activated at 723 K for 1 h under vacuum ($<10^{-6}$ mbar). After cooling to 313 K, propane was dosed to the system stepwise with controlled pressure from 0.3 to 24 mbar. Each step was equilibrated until the sample weight and thermal flux were constant. The adsorption enthalpy was obtained by integration of the heat flux signal and normalized to propane uptake.

3.4 Results and discussion of Ga/BEA on propane dehydrogenation

3.4.1 Catalytic performance of Ga/BEA

Figure 3.1a shows the reaction of propane on Ga/BEA-3.2 with increasing contact time (weight hour space velocity^{-1}, WHSV^{-1}). Propane conversion was negligible in the absence of catalysts. The conversion of propane increased linearly with WHSV^{-1} at low conversions, however, deviated at higher WHSV^{-1}, reaching the equilibrium conversion at 28 % at 1 bar and 813 K.[28] The selectivity of propene began to deviate moderately beyond 10 % conversion in Figure 3.1b and 3.1c, because of secondary (higher order) reactions consuming propene. Methane and ethene were the main byproducts generated from the cracking of propane. While propane cracking should produce equimolar amounts of methane and ethene, the yield of ethene gradually overtook that of methane at higher conversions. This suggests a second pathway to produce ethene such as cracking of higher hydrocarbons formed by oligomerization of propene. And the deviated methane yield at conversion above 12% in Figure 3.1b indicates an increasing selectivity, which could also result from the formation of methane from cracking of higher hydrocarbons at higher conversions. Notably, C_4 to C_6 hydrocarbons and aromatics were observed at higher propane conversions as secondary products, *e.g.*, formed from propene.

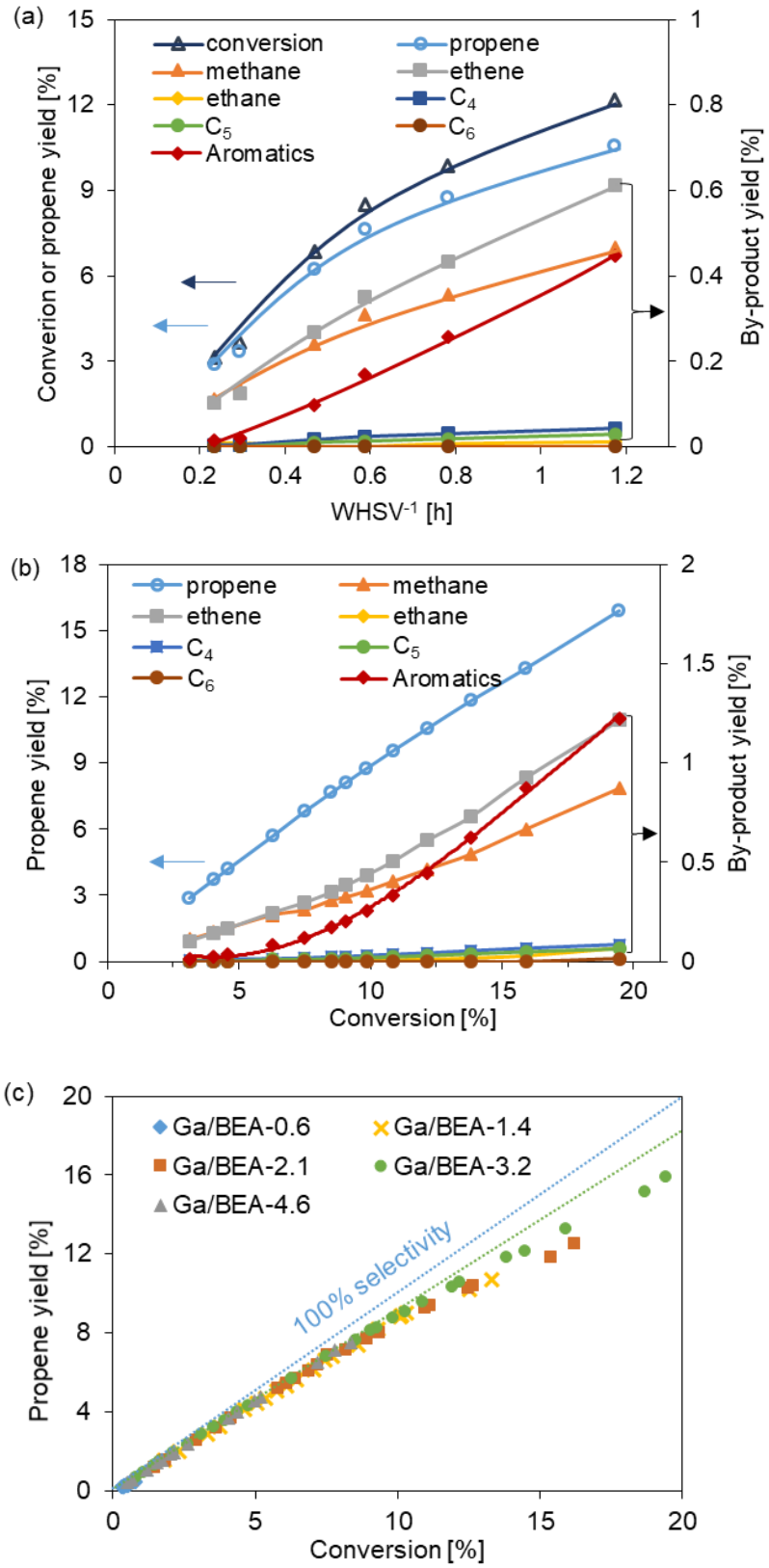

Figure. 3.1 (a) The propane conversion and product yield at different $WHSV^{-1}$ over Ga/BEA-3.2; (b) The yield of different products at different conversion over Ga/BEA-3.2; (c) Propene yield as a function of conversion with different Ga/BEA-X catalysts. Reaction condition: 813K, 1 bar, 5-100 $mL \cdot min^{-1}$, 50 mg catalyst, $p_{C_3H_8}$ 20 mbar.

Figure. 3.1b shows the product yield as a function of propane conversion on Ga/BEA-3.2 at 813 K. At low conversion, the selectivity to propene was 93% with methane (3.5% selectivity) and ethene (3.3% selectivity) being the main side products. The selectivity to propene decreased gradually with propane conversion, reaching 82 % at 19 % conversion. The yield of methane, ethene and aromatics increased correspondingly, while a remarkably high selectivity to propene was still achieved. All Ga/BEA catalysts showed the same trend highlighting the similarity of the sites generated (Figure 3.1c). At 873 K 72 % propene selectivity was achieved at 40 % conversion (Figure S3.3). The selectivity was significantly higher than for previously reported Ga modified zeolites [18, 29] and comparable to the benchmark catalysts Pt/Al_2O_3 and Cr_3O_3/Al_2O_3 (~ 75% at 40% conversion).[29-31] Notably, the ratio of ethene/methane was close to one at conversions up to 35% at 873 K, suggesting the second pathway to form ethene and aromatization became less significant at higher temperatures.

In order to investigate the impact of the concentration of Ga^{3+} on the PDH, the Ga/BEA with Ga loadings (0 - 4.6 wt. %) were studied at 813 K (Figure S3.1). Figure 3.2 shows the rate of propane conversion, as well as rates of dehydrogenation and cracking of propane. For the parent Ga/BEA-0, a reaction rate of 0.05 $\mu mol \cdot g^{-1} \cdot s^{-1}$ was observed at low conversions (<0.1%), showing a propene selectivity of 93%. The byproducts were methane, ethene and ethane. The secondary products (*i.e.*, C_4 to C_6 hydrocarbons and aromatics) from oligomerization and aromatization were not detected. For Ga/BEA-X (0.6 - 4.6 wt.%), propane conversion rates were between 0.25 - 2.5 $\mu mol \cdot g^{-1} \cdot s^{-1}$, increasing by two orders of magnitude in comparison to Ga/BEA-0. With the increase of Ga content, the PDH rate first increased until a Ga content of 3.2 wt. % (Ga/original Zn ratio of 1/2) and decreased at higher Ga content. This suggests the optimal Ga content entails the replacement of two Zn atoms. The stabilization of one Ga cation would involve two silanol nests. These silanols could originate from vacant Zn sites and/or previous silanols.

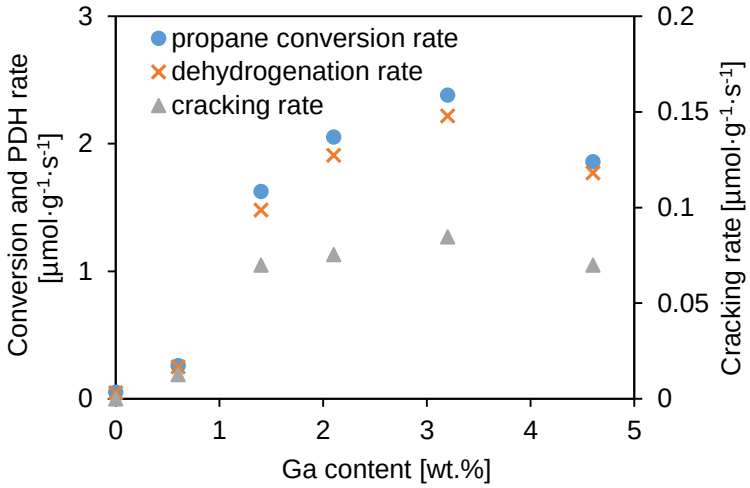

Figure. 3.2 Rates of conversion, dehydrogenation and cracking of propane as a function of Ga content. Reaction condition: 813 K, 1 bar, 50 mL·min^{-1}, 10 mg catalyst, $p_{C_3H_8}$ 20 mbar, at 21 h TOS. Rates were determined at conversions below 4%.

3.4.2 Reaction kinetics

The PDH rate (Figure 3.3a) increased gradually with $p_{C_3H_8}$ to a plateau, with a concurrent decrease of the reaction order from 0.8 at 2 mbar to 0.2 at 100 mbar (Figure 3.3c). The dependence of the cracking rate on $p_{C_3H_8}$ had the same trend as the PDH rate (Figure S3.7). A reaction order of 0.9 was determined at $p_{C_3H_8}$ around 2 mbar, a reaction order of 0.3 at 100 mbar. While the decrease of the reaction order with $p_{C_3H_8}$ could be attributed to increasing coverage of active sites. However, the *in situ* determined constant propane uptake on the catalyst during the reaction (Figure 3.3b, for Ga/BEA-3.2) indicates that this is not a valid hypothesis. The negligible weight increase with different $p_{C_3H_8}$ indicates that the coverage of propane is very low.

The PDH rates of C_3H_8 and C_3D_8 on Ga/BEA-3.2 were 0.47 and 0.29 µmol·g^{-1}·s^{-1} at 2 mbar, respectively, corresponding to a KIE of 1.6. The KIE suggests the cleavage of the C-H bond as the rate determining step (RDS) in agreement with the literature.[32, 33] The KIE value decreased with increasing $p_{C_3H_8}$ and reached 0.8 at 100 mbar (Figure 3.3c). The KIE below 1 at high pressure, is speculated to be caused by the desorption of H_2 as the RDS.[34] With a lower zero-point energy (ZPE) of D_2 compared to H_2, the H_2 desorption step has a higher energy barrier compared to D_2 desorption, leading to an inverse KIE. Thus, we hypothesize that the RDS shifts from C-H bond cleavage to H_2 desorption with increasing $p_{C_3H_8}$. Interestingly, Biscardi and Iglesia proposed H_2 desorption to be the RDS in propane dehydrogenation on Ga/H-ZSM-5 at 773 K, suggesting an irreversible recombinative desorption step of H atoms.[35]

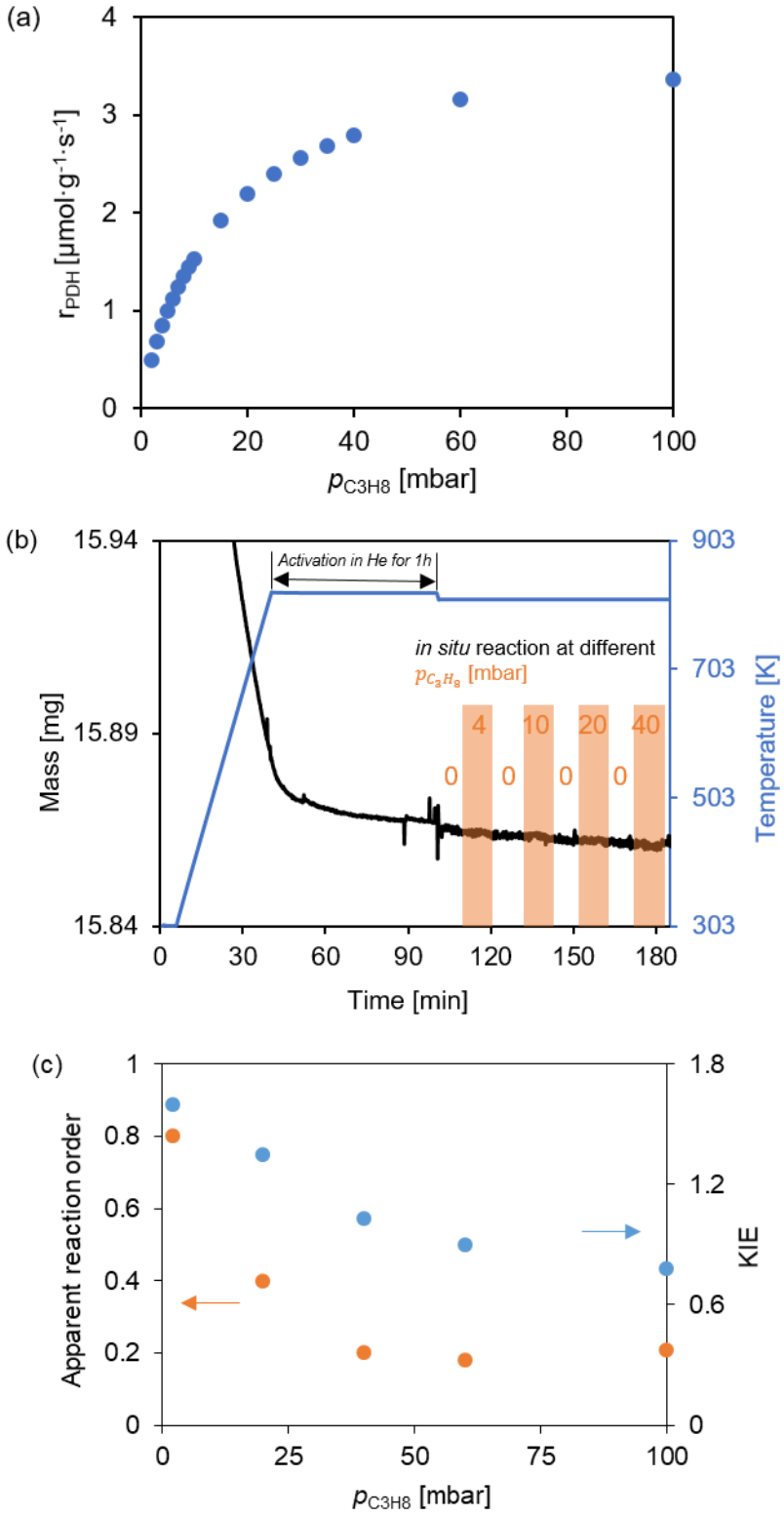

Figure 3.3 (a) PDH rate as a function of $p_{C_3H_8}$ on Ga/BEA-3.2; (b) Propane uptake on Ga/BEA-3.2 during the reaction at 813 K; (c) The decrease of reaction order and KIE as a function of $p_{C_3H_8}$ on Ga/BEA-3.2. Reaction condition: 813 K, 1 bar, 100 mL·min^{-1}, 10 mg catalyst, $p_{C_3H_8}$ 2-100 mbar.

The elementary steps for PDH are listed in Scheme 3.1. Propane first adsorbs reversibly on the site (Scheme 3.1, [C_3H_8-S]). Then, the cleavage of the first C-H bond occurs to form an

intermediate state (Scheme 3.1, [C_3H_7-SH]). Propene is formed as a result of a β-H transfer from the alkyl group to the site (Scheme 3.1, [C_3H_6-SH_2]), leading to the desorption of alkene and H remains on the site (Scheme 3.1, [S-H_2]). Finally, the reaction cycle is completed by the desorption of H_2 and the regeneration of the active site.

$$C_3H_8\,(g) + [S] \overset{K_a^o}{\rightleftharpoons} [C_3H_8\text{-}S]$$

$$[C_3H_8\text{-}S] \xrightarrow{k_1} [C_3H_7\text{-}SH]$$

$$[C_3H_7\text{-}SH] \xrightarrow{k_2} [C_3H_6\text{-}SH_2]$$

$$[C_3H_6\text{-}SH_2] \xrightarrow{k_3} C_3H_6\,(g) + [S\text{-}H_2]$$

$$[S\text{-}H_2] \xrightarrow{k_4} H_2\,(g) + [S]$$

Scheme 3.1. The elementary steps of propane dehydrogenation.

From the equilibrium of the adsorption step, we have

$$K_a^o = \frac{\theta_{C_3H_8-S}}{\theta_s \cdot p_{C_3H_8}/p^o} \tag{1a}$$

$$\theta_s = \frac{\theta_{C_3H_8-S}}{K_a^o \cdot p_{C_3H_8}/p^o} \tag{1b}$$

Where K_a^o is the equilibrium constant of propane adsorption, $\theta_{C_3H_8-S}$ is the coverage of species [C_3H_8-S], as presented in Scheme 3.1, and θ_S is the coverage of the free site. p^o refers to the standard pressure (1 bar).

Applying steady state approximation to species [C_3H_7-SH], [C_3H_6-SH_2] and [S-H_2], leads to:

$$k_1 \cdot \theta_{C_3H_8-S} = k_2 \cdot \theta_{C_3H_7-SH} = k_3 \cdot \theta_{C_3H_6-SH_2} = k_4 \cdot \theta_{S-H_2} \tag{2}$$

The k_i (i=1−4) are forward reaction rate constants of the elementary steps in Scheme 3.1. The $\theta_{C_3H_7-SH}$, $\theta_{C_3H_6-SH_2}$, and θ_{S-H_2} are the coverage of the species [C_3H_7-SH], [C_3H_6-SH_2], and [S-H_2]. The correlation between other site coverages and $\theta_{C_3H_8-S}$ are defined as Eq. (3).

$$\theta_{C_3H_7-SH} = \frac{k_1 \cdot \theta_{C_3H_8-S}}{k_2} \tag{3a}$$

$$\theta_{C_3H_6-SH_2} = \frac{k_1 \cdot \theta_{C_3H_8-S}}{k_3} \tag{3b}$$

$$\theta_{S-H_2} = \frac{k_1 \cdot \theta_{C_3H_8-S}}{k_4} \tag{3c}$$

The site balance will give the relation:

$$\theta_{C_3H_8-S}+\theta_{C_3H_7-SH}+\theta_{C_3H_6-SH_2} + \theta_{S-H_2} + \theta_S = 1 \tag{4}$$

If any of the species [C_3H_8-S], [C_3H_7-SH] and [C_3H_6-SH_2] has substantial coverages, an increase of catalyst weight would be expected during the reaction. However, this was not observed (Figure 3.3b), suggesting very low coverages, *i.e.*, $\theta_{C_3H_8-S} \approx 0, \theta_{C_3H_7-SH} \approx 0, \theta_{C_3H_6-SH_2} \approx 0$. Thus, only the θ_S and θ_{S-H_2} terms remain in the site balance equation:

$$\theta_{S-H_2} + \theta_s = 1 \tag{5}$$

With equations (1b) (3c) and (5), the expression of θ_S, θ_{S-H_2} and *r*, the reaction rate of PDH, are obtained (derivation details in Appendix 3.7.2):

$$\theta_s = \frac{k_4}{k_1 \cdot K_a^o \cdot p_{C_3H_8}/p^o + k_4} \tag{6a}$$

$$\theta_{S-H_2} = \frac{k_1 \cdot K_a^o \cdot (p_{C_3H_8}/p^o)}{k_1 \cdot K_a^o \cdot (p_{C_3H_8}/p^o) + k_4} \tag{6b}$$

$$r = N \cdot k_4 \cdot \theta_{S-H_2} = N \cdot \frac{k_1 \cdot K_a^o \cdot (p_{C_3H_8}/p^o)}{\frac{k_1 \cdot K_a^o \cdot (p_{C_3H_8}/p^o)}{k_4} + 1} \tag{6c}$$

The variable *N* is the concentration of active sites on the catalyst. The reciprocal of the rate equation, Eq. (6c), gives

$$\frac{1}{r} = \frac{1}{N \cdot k_4} + \frac{1}{N \cdot k_1 \cdot K_a^o} \cdot \frac{1}{(p_{C_3H_8}/p^o)} \tag{6d}$$

which indicates the linearly increasing correlation between 1/*r* and $1/(p_{C_3H_8}/p^o)$, with a slope of $1/(N \cdot k_1 \cdot K_a^o)$ and an intercept of $1/(N \cdot k_4)$. This fits well with the measured experimental

data on Ga/BEA-3.2 (Figure 3.4). In particular, at low pressure of propane ($p_{C_3H_8} \rightarrow 0$), the Eq. (6c) can be simplified as Eq. (7).

$$\lim_{p_{C_3H_8}\rightarrow 0} r = N \cdot k_1 \cdot K_a^o \cdot (p_{C_3H_8}/p^o) \quad (7a)$$

$$\lim_{p_{C_3H_8}\rightarrow 0} \theta_S = 1 \quad (7b)$$

When $p_{C_3H_8}$ is very high ($p_{C_3H_8} \rightarrow +\infty$), the Eq. (6) can be simplified as Eq. (8).

$$\lim_{p_{C_3H_8}\rightarrow +\infty} r = N \cdot k_4 \quad (8a)$$

$$\lim_{p_{C_3H_8}\rightarrow +\infty} \theta_{S-H_2} = 1 \quad (8b)$$

From Eq. (7), at very low $p_{C_3H_8}$, the active site is barely covered ($\theta_S = 1$), and the rate equation gives a first order dependency on $p_{C_3H_8}$. The only involved rate constant is k_1, indicating the cleavage of the first C-H bond of propane is the RDS at this condition. Our measured KIE of 1.6 of PDH rates over C_3H_8 and C_3D_8 on Ga/BEA-3.2 also showed the factor for the C-H bond cleavage.[32, 33] From Eq. (8) at high pressure ($p_{C_3H_8} \rightarrow +\infty$), the active site is nearly fully covered by H_2 ($\theta_{S-H_2} = 1$), and the rate equals $N \cdot k_4$ and is independent of $p_{C_3H_8}$. The desorption of H_2 becomes the RDS. This is in line with the measured KIE of 0.8 and the reaction order of 0.2 at 100 mbar propane. The shift of the RDS from C-H bond cleavage to H_2 desorption is in agreement with the decrease of the KIE and the PDH reaction order with increasing $p_{C_3H_8}$.

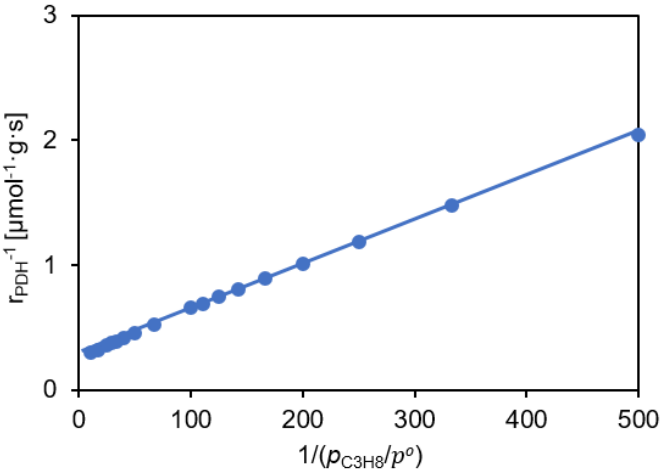

Figure 3.4. Regression of PDH rate over Ga/BEA-3.2 with Eq. (6d). Reaction condition: 813 K, 1 bar, 100 mL·min^{-1}, 10 mg catalyst, $p_{C_3H_8}$ 2-100 mbar.

3.4.3 Nature and concentration of active sites

The reaction results on other Ga/BEA catalysts also show good regression with Eq. (6d) (Figure S3.9), implying that the catalytic activity on all these catalysts is dominated by one type of active site and follow the same reaction mechanism. This is further supported by Figure 3.5, which plots log *r* vs. $p_{C_3H_8}$, that all Ga/BEA catalysts show the same dependence, varying only by the magnitude of the rates. This close analogy between the different catalysts displayed in Figure 3.5 substantiates the same active site and reaction mechanism, while the different intercepts on the y-axis indicate different concentrations of the active site. Thus, we note that different types of sites, such as isolated BAS and LAS, exist on Ga/BEA, but that either only one site or a fixed combination of sites determine catalytic activity and selectivity.

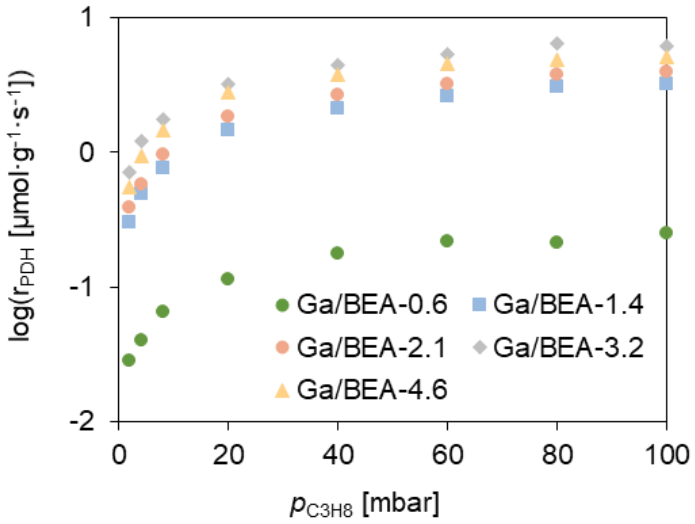

Figure 3.5. Correlation between PDH rate and $p_{C_3H_8}$ on different Ga/BEA-X catalysts. Reaction condition: 813 K, 1 bar, 100 mL·min^{-1}, 10 mg catalyst, $p_{C_3H_8}$ 2-100 mbar.

To determine the concentration of this active site, we note that H_2 adsorbs reversely on it as shown in the elementary step (IV) in Scheme 3.1. This allowed us to determine its concentration by adsorption and desorption of H_2. Figure 3.6a shows the temperature programmed desorption profile of pre-adsorbed H_2 on Ga/BEA-3.2 (desorption profiles of other catalysts are shown in Appendix Figure S3.10). H_2 was adsorbed on the catalyst at liquid N_2 temperature under 1 bar H_2 flow and desorbed with a fixed temperature increment in flowing He. The desorption peak covered a temperature range from 398 to 493 K (Figure 3.6a). The concentration of desorbed H_2 directly correlated with the PDH rate (Figure 3.6b), suggesting that stabilizing H on the catalyst is a critical property of the catalyst. Such a good correlation is not seen when correlating the rate *vs* the concentration of Ga, BAS or LAS (Figure 3.2 and Appendix Figure S3.4).

It suggests that the active sites cannot be solely Brønsted or Lewis acid induced by Ga. As reported, the Lewis acidic Ga_2O_3 catalyst would deactivate rapidly due to the reduction of Ga^{3+} sites during propane dehydrogenation.[36, 37] The dehydrogenation activity and selectivity also both decreased with the generation of BAS in Ga/SiO_2 with the BAS preferentially catalyzing cracking and oligomerization.[37] In contrast to these deactivating catalysts, the slightly increasing rates of Ga/BEA for PDH were observed with 21 h TOS (Figure S3.1). Thus, it appears to have a synergy between the BAS from the incorporated Ga site in the zeolite framework and the LAS from the EX Ga site to contribute to the good PDH performance on Ga/BEA. We have reported the superior efficiency of the Lewis-Brønsted acid pair in Ga/H-ZSM-5 on PDH.[7] Whereas, it was also excluded by the fact that the PDH rate dropped from 2.2 to 0.8 $\mu mol \cdot g^{-1} \cdot s^{-1}$ after pre-reducing the Ga^{3+} sites into Ga^{+} by 1 bar H_2 at 823 K for 1 h (Figure S3.5), which was contrary to the results on Lewis-Brønsted acid pair on Ga/H-ZSM-5.

It should be noted that the concentration of stabilized H_2 was two orders of magnitude lower than the concentrations of Ga, BAS or LAS on Ga/BEA. This could either point to a very low fraction of active sites or to a high kinetic or thermodynamic barrier for the dissociative adsorption of H_2.

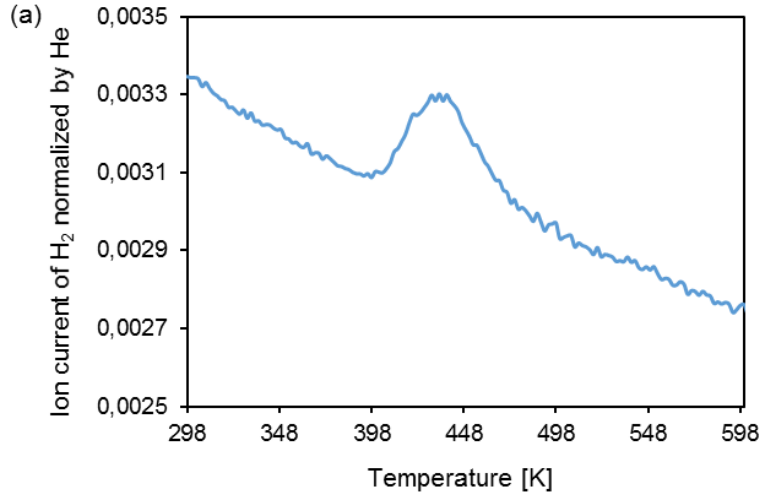

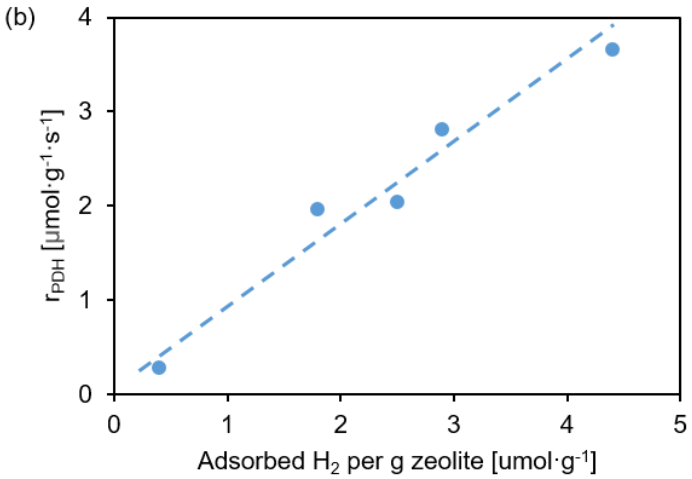

Figure. 3.6 (a) H_2 desorption with the increase of temperature (30 K·min^{-1}) on Ga/BEA-3.2; (b) Correlation between PDH rate at 100 mbar and the concentration of adsorbed H_2 on Ga/BEA-X catalysts.

The activation energies for the first C-H bond cleavage and the H_2 desorption step were calculated by the temperature dependence of the regressed $N{\cdot}k_1{\cdot}K_a^o$ and $N{\cdot}k_4$ using Eq. (6d). The Arrhenius plot for the reactions on Ga/BEA-3.2 from 793 to 843 K is shown in Figure 3.7, and the activation energies were summarized in Table 3.1. It shows the C-H bond cleavage has an intrinsic activation energy of 155 ± 8 kJ·mol^{-1}, which is 32 kJ·mol^{-1} higher than that of the H_2 desorption step. The apparent activation enthalpy of PDH was 129 ± 7 kJ·mol^{-1} by Lewis-Brønsted acid pair on Ga/ZSM-5 and 80 ± 25 kJ·mol^{-1} by Ga/H-MFI with $[GaH]^{2+}$ as the main active site.[7, 13] The results further indicate that the active site on the Ga/BEA is different from the Lewis-Brønsted acid pair or $[GaH]^{2+}$ reported earlier.

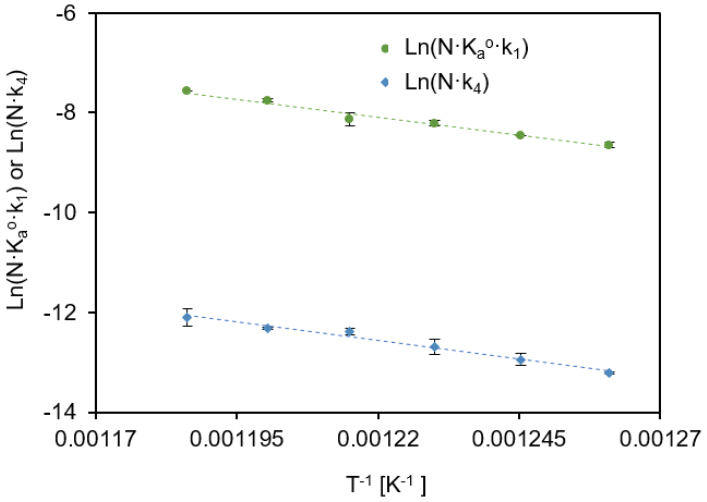

Figure 3.7. Arrhenius plot for Ga/BEA-3.2 from 793 to 823 K. Reaction condition: $p_{C_3H_8}$ 2-100 mbar, 1 bar, 100 mL·min^{-1}, 10 mg catalyst.

Table 3.1 Adsorption enthalpy and activation energies of elementary steps on PDH over Ga/BEA-3.2

Elementary step	Propane adsorption*	C-H bond cleavage	H_2 desorption
ΔH_{ads}^{o} *or* E_a [kJ·mol^{-1}]	-35 ± 7	155 ± 8	123 ± 8

* The calculation of adsorption enthalpy of propane is shown in Figure S3.11.

As H_2 desorption is the RDS at high $p_{C_3H_8}$, the heat of H_2 desorption on Ga/BEA-3.2 was also measured to compare with the E_a. From the temperature-programed desorption profile of H_2 in Figure 3.6a, the desorption heat was calculated as 121 kJ·mol^{-1} via the Redhead method (Appendix 3.7.3).[38, 39] It agrees well with the E_a of 123 ± 8 kJ·mol^{-1} for the H_2 desorption step, substantiates our proposed elementary steps and RDS.

It is well known that the BAS are active for the oligomerization and cyclization steps of alkane aromatization,[25-27] high aromatics selectivity (>50%) was observed at propane conversion above 20% on Ga loaded H-MFI.[40] In contrast, low selectivity of aromatics (<6.5%) at high conversions (*i.e.*, 19% and 40%) was observed on Ga/BEA (Figure 3.1b and S3.3). The good propene selectivity is more in line with the Lewis acidic Cr_3O_3/Al_2O_3 catalyst.[29] It is possible that the lower activity of BAS led to less aromatization reactions since it is believed that the BAS induced by Ga provides lower acidity than Al.[41] It has been also reported that the bridging OH band associated with framework Ga in the hydroxyl stretching region decreased its intensity with increasing preheating temperature above 700 K.[42] The Ga had a distinct tendency to go into either partial or total EX positions via high temperature hydrolysis of Si-O-T followed by dehydration, leading to the formation of strong Lewis acid centers in the zeolite pore structure. Therefore, at the high pretreatment temperature (823 K) and the reaction temperature (813 K), it is likely that some framework Ga sites in Ga/BEA could migrate to EX and ultimately form small oxidic clusters. It appears to reduce the effect of BAS on aromatics formation. The EX Ga sites have been suggested to be the main active sites instead of the framework Ga in gallosilicate catalysts.[43-46] However, if a variety of acid sites can be simultaneously present in Ga/BEA depending on the pretreatment conditions and they can act individually or in synergy, the investigation of the site structure and the interpretation of their catalytic performance will be complicated.

3.5 Effect of Ga-BEA (HS) and Pt/Ga-BEA (HS) on propane dehydrogenation

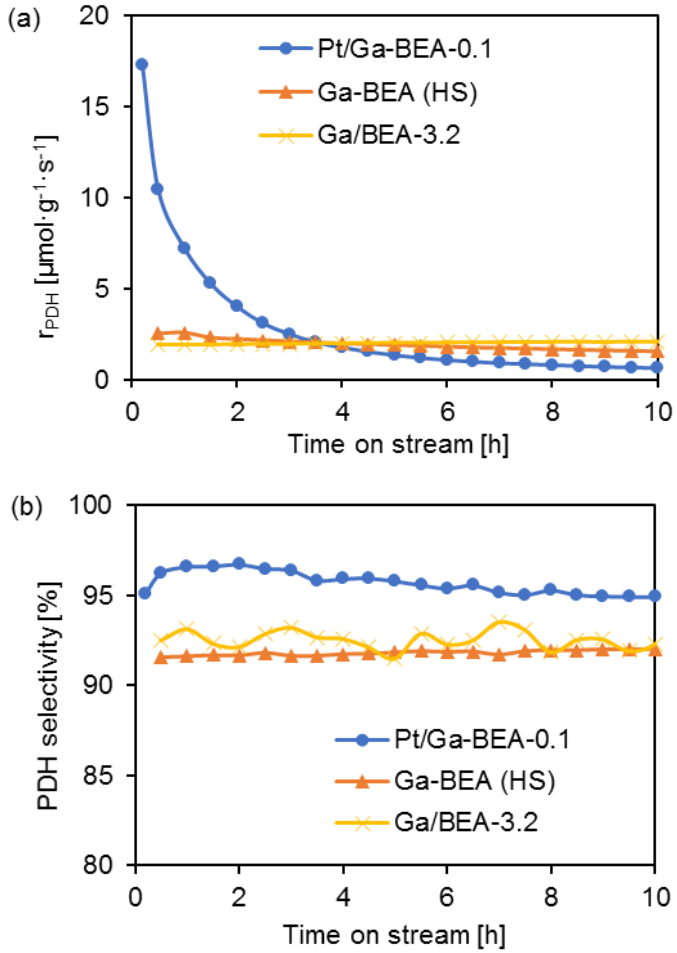

Figure 3.8 (a) The comparison among Ga-BEA (HS) (Ga 4.6 wt.%), Ga/BEA-3.2 and Pt/Ga-BEA (HS)-0.1 (Pt 0.1 wt.%) on PDH; (b) Dehydrogenation selectivity of different catalysts with TOS. Reaction condition: 813 K, 1 bar, 50 mL·min^{-1}, 10 mg catalyst, $p_{C_3H_8}$ 20 mbar.

Ga-BEA (HS) prepared directly from hydrothermal synthesis was tested to compare the PDH performance with Ga/BEA-3.2. The initial PDH rate was higher on Ga-BEA (HS) (Figure 3.8a) and the two catalysts showed the same dehydrogenation selectivity (Figure 3.8b). The Ga-BEA (HS) has much higher BAS and LAS concentrations, thus a higher concentration of catalytic active sites, leading to a higher initial PDH rate. However, it deactivated by 52% and the PDH rate decreased from 2.6 to 1.4 μmol·g^{-1}·h^{-1} within 21 h TOS while no deactivation was observed on Ga/BEA-3.2 under the same conditions. This could be attributed to the much higher concentration of BAS and sLAS on Ga-BEA (HS) compared to Ga/BEA-3.2 (BAS: 560 *vs* 95 μmol·g^{-1}; sLAS: 436 vs 159 μmol·g^{-1}). They both can catalyze oligomerization and aromatization reactions to form coke precursors that gradually covered the active sites.[25-27]

Furthermore, the PDH rate increased to 17.3 μmol·g^{-1}·h^{-1} on Pt/Ga-BEA (HS)-0.1 at 10 min TOS, which was one order of magnitude higher than that of Ga-BEA (HS) and Ga/BEA-3.2 (Figure 3.8a). The selectivity of propene was also improved and it kept stable within 10 h TOS (Figure 3.8b). Nevertheless, like Ga-BEA (HS), Pt/Ga-BEA (HS)-0.1 deactivated fast to a PDH rate of 0.7 μmol·g^{-1}·h^{-1} at 10 h TOS. The sintering of Pt particles [47, 48] and coke deposition [49] could both be the reasons. With a regeneration of Pt/Ga-BEA (HS)-0.1 in synthetic air at 813 K for 15 min, the catalytic activity was easily recovered for three runs as shown in Figure 3.9, suggesting that the coke deposition was the main reason for the deactivation. The easy and fast regeneration process suggests a promising commercial potential of the catalyst.

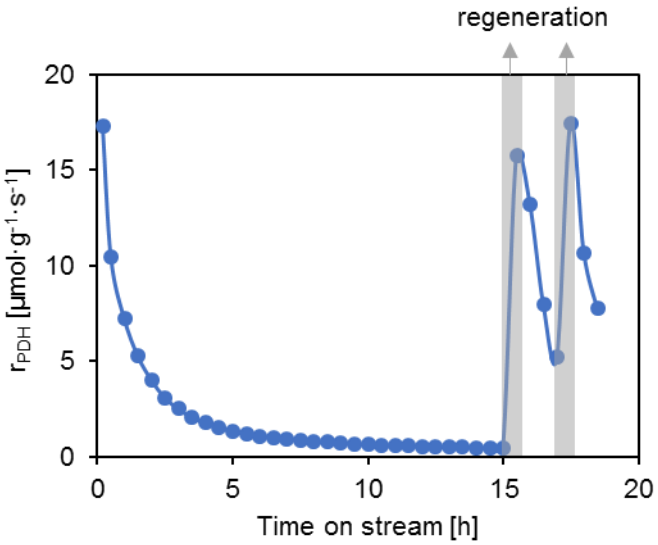

Figure 3.9 The effect of regeneration on Pt/Ga-BEA (HS)-0.1. Reaction condition: 813 K, 1 bar, 50 mL·min^{-1}, 10 mg catalyst, $p_{C_3H_8}$ 20 mbar, regeneration condition: 813 K in 50 mL·min^{-1} synthetic air for 15 min.

The effect of Pt loading was also studied. In Figure 3.10, the PDH rate increased first to reach an optimal value with Pt content of 0.1 wt.% and decreased further at higher Pt content. On the contrary, the cracking rate decreased linearly with increasing Pt content, implying that the PDH and cracking were catalyzed by different active sites. The active sites for cracking are dominated by BAS whose concentration decreased with Pt loading in Table 2.4, while the PDH active sites are related to a synergy between Ga and Pt, the optimal activity was achieved at 0.1 wt.% of Pt (Pt/Ga ratio of 1/129). The synergy between Ga and Pt has already been observed on a catalyst with 1000 ppm Pt, 3 wt.% Ga, and 0.25 wt.% K supported on alumina by Weckhuysen *et al.*[50] They proposed the unsaturated Ga^{3+} species as the active species and Pt as the promoter since the PDH activity did not change when Pt dispersion collapsed at 1023 K during the regeneration process. In contrast, in an early report of a Ga/Pt/Al_2O_3 catalyst, Ga was found to have a small effect on the activity but modify the structure of the metallic

phase.[49] It has also been reported that nanometric Ga-Pt bimetallic particles, supported on partially dehydroxylated silica, exhibited outstanding catalytic performance on PDH.[51] A fraction of Ga remained as isolated sites in highly dispersed Ga_xPt ($0.5< x <0.9$) alloyed structure and showed activity far surpassing each of the individual components. Even though different hypotheses have been proposed, the roles of Pt and Ga remain in debate and further studies are desired.

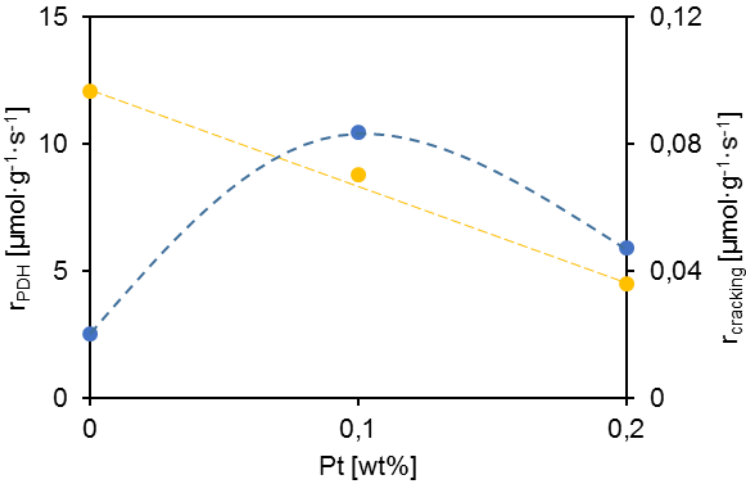

Figure 3.10 The PDH rate as a function of Pt content. Reaction condition: 813 K, 1 bar, 50 mL·min^{-1}, 10 mg catalyst, $p_{C_3H_8}$ 20 mbar, the rates are obtained at 0.5 h TOS.

3.6 Conclusion

The controlled incorporation of Ga in BEA via substitution of lattice Zn^{2+} led to a series of Ga-BEA zeolites with homotopic sites active for propane dehydrogenation. Propane conversion rate increased with the concentration of Ga from 0.05 $\mu mol \cdot g^{-1} \cdot s^{-1}$ on the parent sample without Ga to 2.5 $\mu mol \cdot g^{-1} \cdot s^{-1}$ on Ga/BEA-3.2, however, further increase of Ga concentration to 4.6 wt.% led to the drop of rate to 1.6 $\mu mol \cdot g^{-1} \cdot s^{-1}$. A high propene selectivity of 82% was obtained at 19 % conversion at 813 K and 72% selectivity was obtained at 40% conversion at 873 K on Ga/BEA-3.2.

The PDH exhibited a first-order kinetics concerning propane and the KIE with C_3H_8 and C_3D_8 turned out to be 1.6 at low pressure of propane of 2 mbar. With the increase of propane pressure, both reaction order and KIE decreased gradually to 0.2 and 0.8 at 100 mbar. Negligible changes of the catalyst weight with increase of propane pressure was observed in the propane uptake measurement, which excluded the high coverage of propane or its C_3-derivatives on the active sites. Together with kinetic analysis, we demonstrated the gradual shift of RDS from C-H bond cleavage at low propane pressure to H_2 desorption at high propane pressure. The model allowed to derive a kinetic equation, which showed good regression with the measured rates on all the Ga/BEA catalysts. With the regressed rate constants, the activation energies of the first C-H bond cleavage and the H_2 desorption were calculated to be 155 ± 8 and 123 ± 8 $kJ \cdot mol^{-1}$, respectively.

To quantify the catalytic active sites, the concentration of H_2 adsorbed/desorbed reversely on the catalysts was determined via temperature-programed desorption of H_2. The measured H_2 concentrations correlated proportionally with the PDH rate of all different Ga/BEA catalysts. The heat of H_2 desorption (121 $kJ \cdot mol^{-1}$) was in good agreement with the measured activation energy of the H_2 desorption step, which further substantiates the kinetic model. Surprisingly, the determined concentration of adsorbed/desorbed H_2 was around two orders of magnitude lower than the concentration of Ga in Ga/BEA catalysts. This indicated only a small fraction of the active sites could be determined by the method of H_2 adsorption/desorption or the H_2 adsorption is highly thermodynamically or kinetically limited.

For comparison, the Ga-BEA (HS) was synthesized hydrothermally and it showed higher initial PDH activity compared with Ga/BEA-3.2; however, deactivated fast. Notably, with the addition of Pt on Ga-BEA (HS), the PDH rate increased by one order of magnitude with Pt/Ga-BEA(HS)-0.1. and the synergy between Ga and Pt was observed with 0.1 wt.% of Pt. The easy

regeneration of Pt/Ga-BEA(HS) in synthetic air implied the promising industrial application of the catalyst.

3.7 Appendix

3.7.1 Catalytic performance on propane dehydrogenation

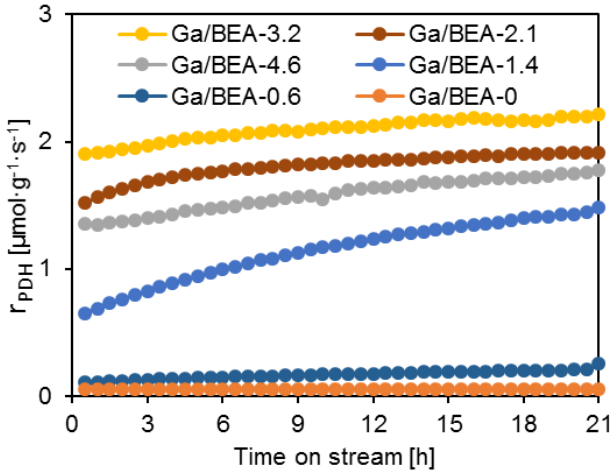

Figure S3.1 Propane dehydrogenation rate as a function of TOS with different Ga/BEA-X catalysts. Reaction condition: 813K, 1 bar, 50 mL·min^{-1}, 10 mg catalyst, $p_{C_3H_8}$ 20 mbar.

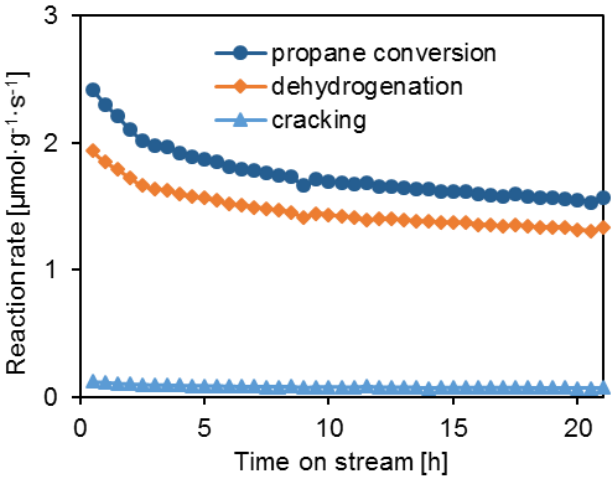

Figure S3.2 Propane conversion rate, dehydrogenation rate and cracking rate as a function of TOS with Ga/BEA-3.2 at high propane conversion. Reaction condition: 813 K, 10 mg Ga/BEA-3.2, 1 bar, 50 mL·min^{-1}, $p_{C_3H_8}$ 20 mbar.

A deactivation rate of 31 % on dehydrogenation and 40 % on cracking was observed within 21 h TOS by running the reaction at a high conversion level (24.2% to 15.7%, Figure S3.2). Thermogravimetric analysis (TGA-MS) showed the deactivation was due to coke deposition, resulting in a total of 15 mg C/g catalyst. In contrary to the deactivation behavior on both dehydrogenation and cracking, the dehydrogenation/cracking ratio increased slowly with TOS. This could be explained by a stronger decrease in the cracking rate due to the higher rate of deactivation on BAS, assuming protolytic cracking occurs mainly with BAS. The coked Ga/BEA-3.2 was re-calcined at 823 K for 5 h and re-used, giving nearly the same initial activity

of 2.3 μmol·g^{-1}·s^{-1} on propane conversion and a dehydrogenation selectivity of 94%, which suggests the easy regeneration and good reusability of the catalysts.

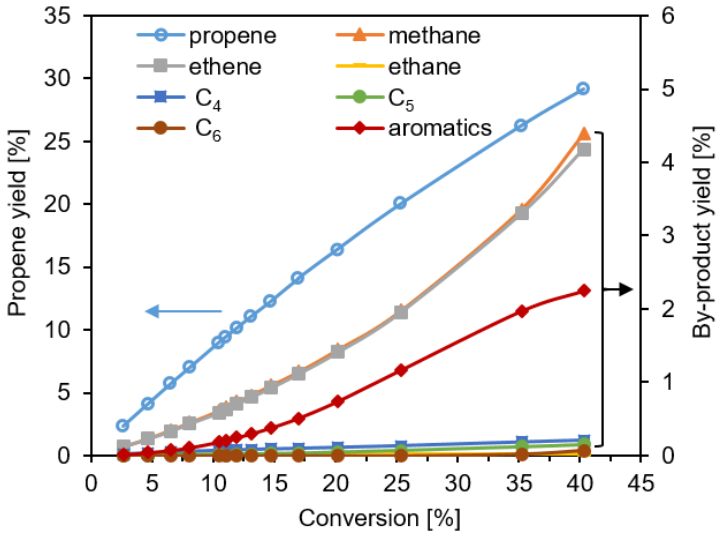

Figure S3.3 The yield of different products at different conversion on Ga/BEA-3.2 at 873 K. Reaction condition: 873K, 1 bar, 5-140 mL·min^{-1}, WHSV 29.8-0.13 h^{-1}, $p_{C_3H_8}$ 20 mbar.

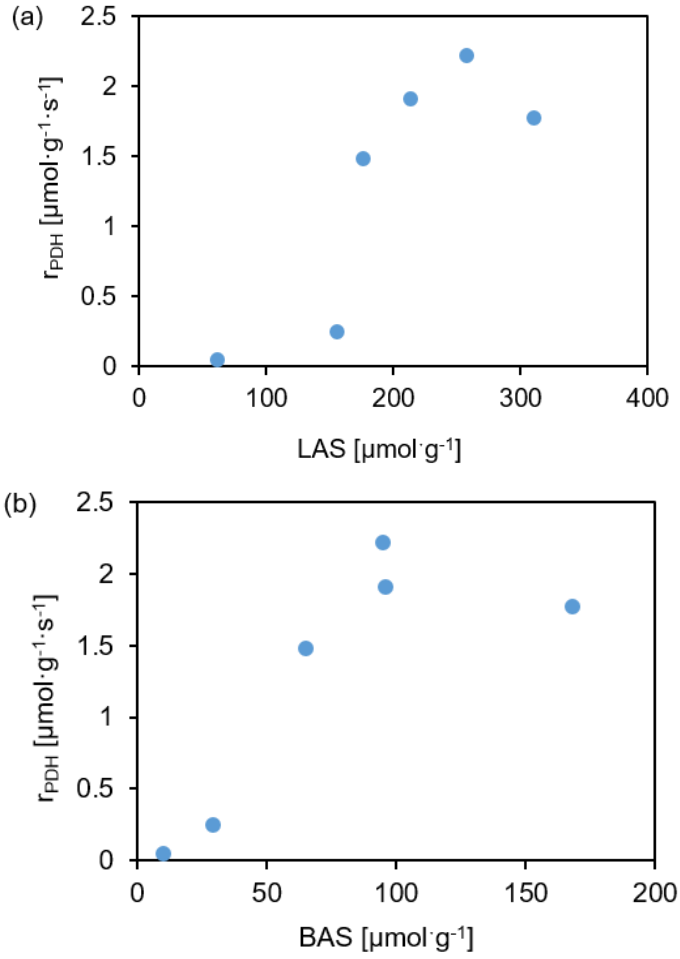

Figure S3.4 Rates of PDH as a function of LAS and BAS concentration. Reaction condition: $p_{C_3H_8}$ 20 mbar, 1 bar, 50 mL·min^{-1}, 10 mg catalyst, 813 K, at 21 h TOS.

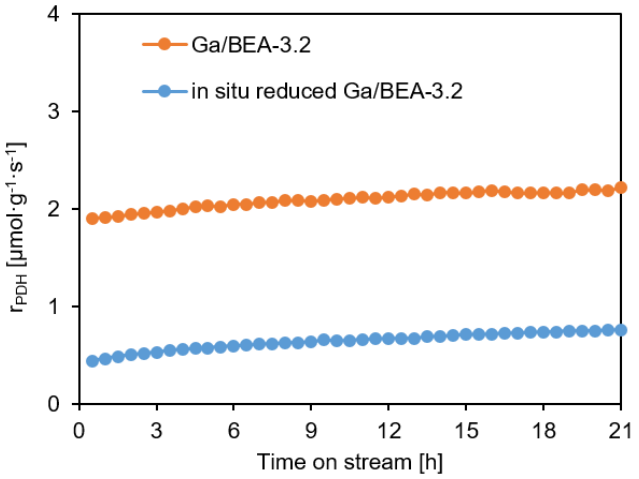

Figure S3.5 PDH rate on Ga/BEA-3.2 with different pre-treatments. Reaction condition: *in situ* pre-drying in He at 823 K for 1 h or reduction in H_2 at 823 K for 1 h, 813 K, 1 bar, 50 mL·min^{-1}, 10 mg catalyst, $p_{C_3H_8}$ 20 mbar.

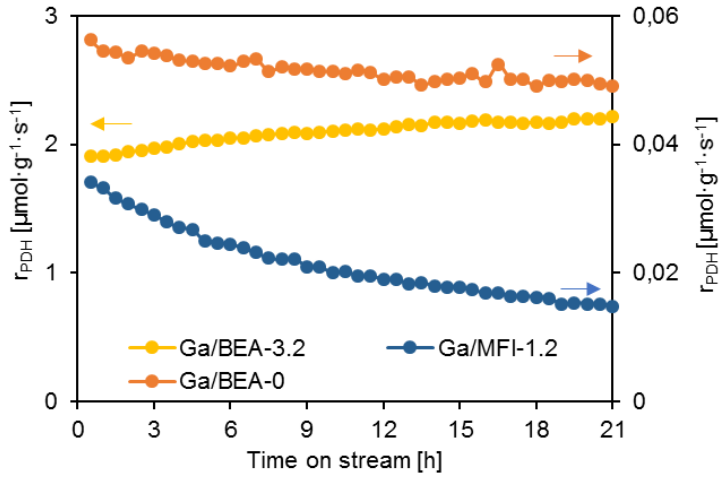

Figure S3.6 Comparison of PDH performance on Ga/BEA-3.2, Ga/MFI-1.2 and Ga/BEA-0. Reaction condition: 813K, 1 bar, 50 mL·min^{-1}, 10 mg catalyst, $p_{C_3H_8}$ 20 mbar.

The rate of PDH on Ga/MFI-1.2 was two orders of magnitude lower than that of Ga/BEA-3.2 and even lower than that on Ga/BEA-0. It also decreased obviously with time, indicating a significant deactivation. This is expected as both Ga and Zn were found to be leached during H_2 treatment of Ga/Zn-MFI-2.7 and finally only a small amount of weak LAS was observed with pyridine adsorbed IR on Ga/MFI-1.2. It can be concluded that Ga/MFI-1.2 had a low activity on PDH.

3.7.2 Reaction kinetics

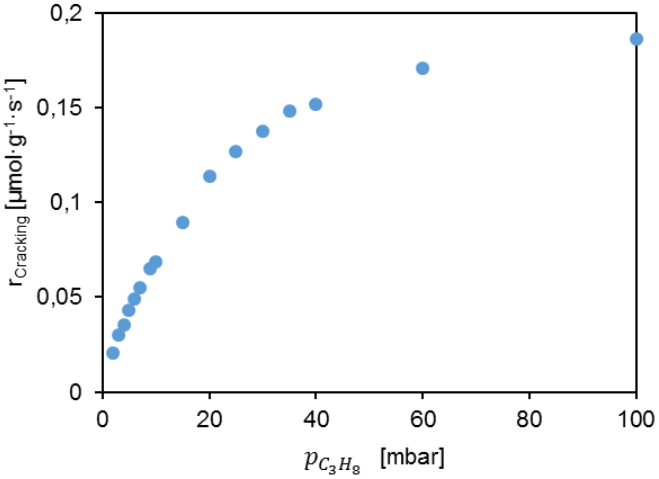

Figure S3.7 Measured cracking rate on Ga/BEA-3.2 with $p_{C_3H_8}$ ranging from 2-100 mbar. Reaction condition: 813 K, 1 bar, 100 mL·min^{-1}, 10 mg catalyst.

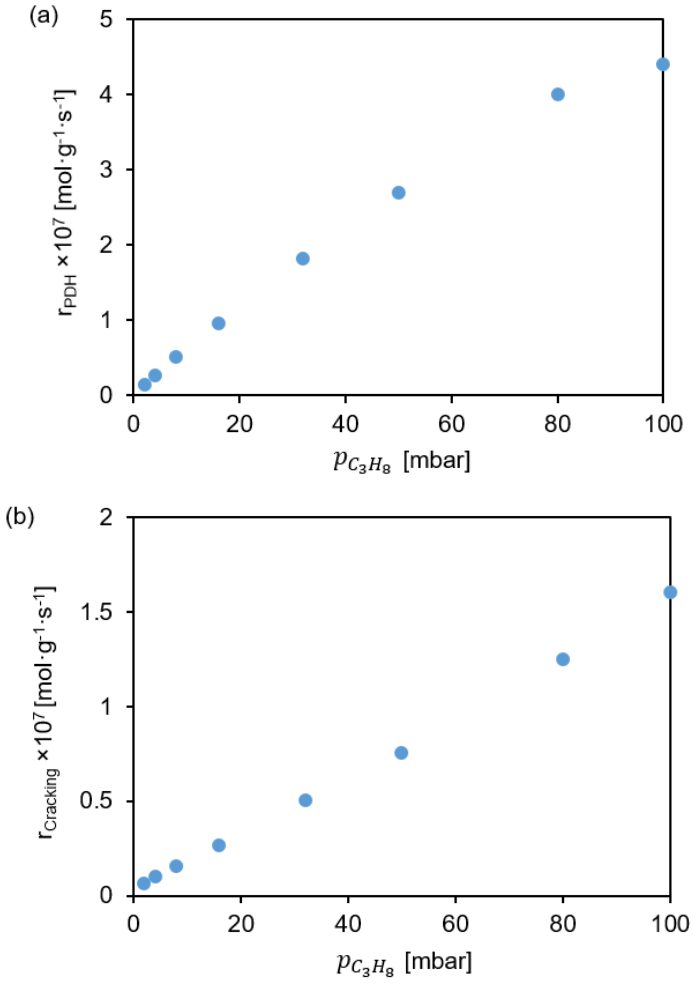

Figure S3.8 Measured reaction rates on Ga/BEA-0.6 (a) dehydrogenation; (b) cracking. Reaction condition: 813 K, 1 bar, 100 mL·min^{-1}, 10 mg catalyst.

Derivation of the kinetic equation

With the following equations in the manuscript:

$$\theta_s = \frac{\theta_{C_3H_8-S}}{K_a^o \cdot p_{C_3H_8}/p^o} \quad (1b)$$

$$\theta_{S-H_2} = \frac{k_1 \cdot \theta_{C_3H_8-S}}{k_4} \quad (3c)$$

$$\theta_{S-H_2} + \theta_s = 1 \quad (5)$$

Taking Eq. (1b) and (3c) into (5), we have

$$\frac{k_1 \cdot \theta_{C_3H_8-S}}{k_4} + \frac{\theta_{C_3H_8-S}}{K_a^o \cdot p_{C_3H_8}/p^o} = 1$$

Then $\theta_{C_3H_8-S}$ can be obtained as:

$$\theta_{C_3H_8-S} = \frac{k_4 \cdot K_a^o \cdot p_{C_3H_8}/p^o}{k_1 \cdot K_a^o \cdot p_{C_3H_8}/p^o + k_4}$$

Therefore we have:

$$\theta_s = \frac{1}{K_a^o \cdot p_{C_3H_8}/p^o} \times \frac{k_4 \cdot K_a^o \cdot p_{C_3H_8}/p^o}{k_1 \cdot K_a^o \cdot p_{C_3H_8}/p^o + k_4} = \frac{k_4}{k_1 \cdot K_a^o \cdot p_{C_3H_8}/p^o + k_4}$$

$$\theta_{S-H_2} = \frac{k_1}{k_4} \times \frac{\frac{k_4 \cdot K_a^o \cdot p_{C_3H_8}}{p^o}}{\frac{k_1 \cdot K_a^o \cdot p_{C_3H_8}}{p^o} + k_4} = \frac{k_1 \cdot K_a^o \cdot (p_{C_3H_8}/p^o)}{k_1 \cdot K_a^o \cdot (p_{C_3H_8}/p^o) + k_4}$$

$$r = N \cdot k_4 \cdot \theta_{S-H_2} = N \cdot \frac{k_4 \cdot k_1 \cdot K_a^o \cdot p_{C_3H_8}/p^o}{k_1 \cdot K_a^o \cdot p_{C_3H_8}/p^o + k_4} = N \cdot \frac{k_1 \cdot K_a^o \cdot (p_{C_3H_8}/p^o)}{\frac{k_1 \cdot K_a^o \cdot (p_{C_3H_8}/p^o)}{k_4} + 1}$$

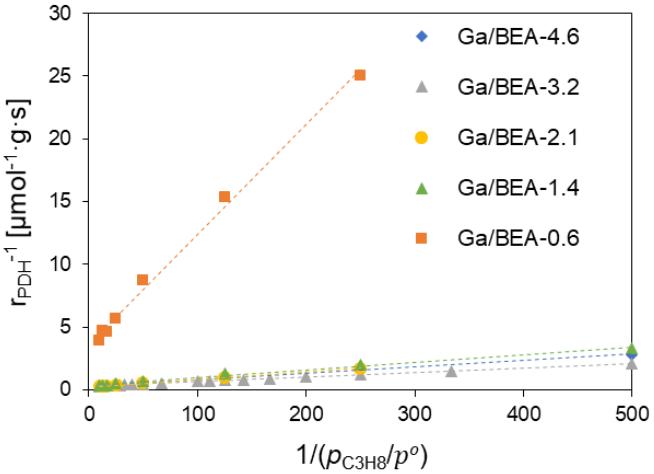

Figure S3.9 Regression of experimental data with the kinetic equation 6d. (1/*r* vs. 1/($p_{C_3H_8}/p^o$)) for all Ga/BEA-X catalysts. Reaction condition: 813 K, 1 bar, 100 mL·min^{-1}, 10 mg catalyst, $p_{C_3H_8}$ 2-100 mbar.

3.7.3 H_2 and propane adsorption on catalysts

Calculation of heat of adsorption of H_2:

From Polanyi-Wigner equation $r_{des} = -\frac{d\theta}{dt} = v_n \cdot \exp(-\frac{\Delta E_{des}}{RT}) \cdot \theta^n$

Based on the Redhead method for a 1st order desorption [38, 39]

$$\Delta E_{des} = RT_{max}[ln\frac{v_1 \cdot T_{max}}{\beta} - ln\frac{\Delta E_{des}}{RT_{max}}]$$

Where ΔE_{des} is the desorption heat

T_{max} is the temperature of the desorption rate maximum

β is the heating rate

v_1 is the frequency factor

T_{max}=438 K, β=0.5 K·s^{-1}, v_1=10^{13} s^{-1}, and $ln\frac{\Delta E_{des}}{RT_{max}}$ is estimated to be 3.5.

$$\Delta E_{des}=8.314 \times 438 \times [ln\frac{10^{13} \times 438}{0.5} - 3.5] \text{ kJ/mol}=121 \text{ kJ/mol}$$

Checking $ln\frac{\Delta E_{des}}{RT_{max}} = 3.503$, the error is 0.08 %.

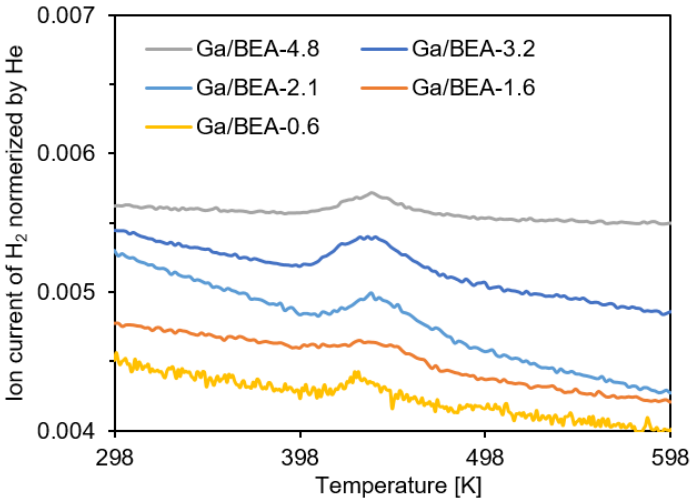

Figure S3.10 H_2 desorption with the increase of temperature (30 K·min^{-1}) on Ga/BEA-X.

Propane adsorption on Ga/BEA-3.2 at 313 K

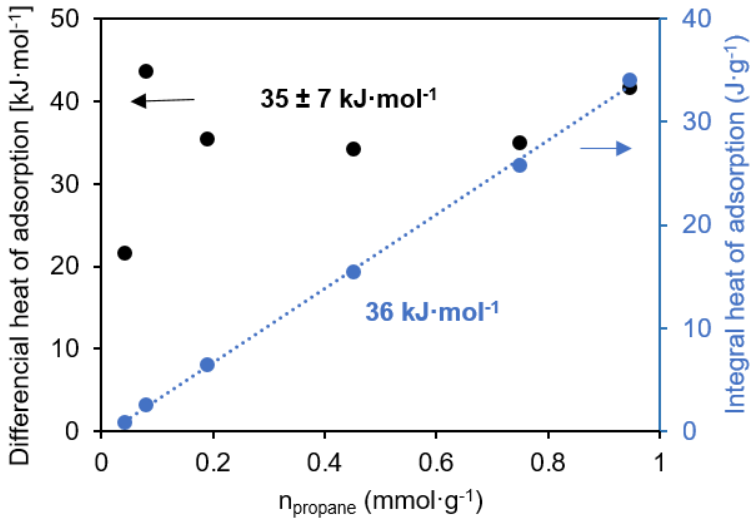

Figure S3.11 The determination of adsorption enthalpy of propane on Ga/BEA-3.2.

3.8 Reference

[1] Ceresana, Market Study: Propylene (2_{nd} edition), ceresana.com, (2014) accessed September 2021.

[2] J.J.H.B. Sattler, J. Ruiz-Martinez, E. Santillan-Jimenez, B.M. Weckhuysen, Catalytic Dehydrogenation of Light Alkanes on Metals and Metal Oxides, Chemical Reviews, 114 (2014) 10613-10653.

[3] S. Chen, X. Chang, G. Sun, T. Zhang, Y. Xu, Y. Wang, C. Pei, J. Gong, Propane dehydrogenation: catalyst development, new chemistry, and emerging technologies, Chemical Society Reviews, 50 (2021) 3315-3354.

[4] C.R. Bayense, A.J.H.P. van der Pol, J.H.C. van Hooff, Aromatization of propane over MFI-gallosilicates, Applied Catalysis, 72 (1991) 81-98.

[5] K.M. Dooley, T.F. Guidry, G.L. Price, Control of Intrazeolitic Gallium Cation Content and Its Effects on C_2 Dehydrogenation in Ga-MFI Catalysts, Journal of Catalysis, 157 (1995) 66-75.

[6] J. Bandiera, Y.B. Taarit, On the enhanced dehydrogenation versus cracking ability of an acidic gallium MFI: A tentative acid base interaction model, Applied Catalysis, 76 (1991) 199-208.

[7] M.W. Schreiber, C.P. Plaisance, M. Baumgärtl, K. Reuter, A. Jentys, R. Bermejo-Deval, J.A. Lercher, Lewis–Brønsted Acid Pairs in Ga/H-ZSM-5 To Catalyze Dehydrogenation of Light Alkanes, Journal of the American Chemical Society, 140 (2018) 4849-4859.

[8] V.J. Cybulskis, S.U. Pradhan, J.J. Lovón-Quintana, A.S. Hock, B. Hu, G. Zhang, W.N. Delgass, F.H. Ribeiro, J.T. Miller, The Nature of the Isolated Gallium Active Center for Propane Dehydrogenation on Ga/SiO_2, Catalysis Letters, 147 (2017) 1252-1262.

[9] S.-W. Choi, W.-G. Kim, J.-S. So, J.S. Moore, Y. Liu, R.S. Dixit, J.G. Pendergast, C. Sievers, D.S. Sholl, S. Nair, Propane dehydrogenation catalyzed by gallosilicate MFI zeolites with perturbed acidity, Journal of Catalysis, 345 (2017) 113-123.

[10] W.-g. Kim, J. So, S.-W. Choi, Y. Liu, R.S. Dixit, C. Sievers, D.S. Sholl, S. Nair, C.W. Jones, Hierarchical Ga-MFI catalysts for propane dehydrogenation, Chemistry of Materials, 29 (2017) 7213-7222.

[11] R. Fricke, H. Kosslick, G. Lischke, M. Richter, Incorporation of gallium into zeolites: syntheses, properties and catalytic application, Chemical Reviews, 100 (2000) 2303-2406.

[12] M. Nakai, K. Miyake, R. Inoue, K. Ono, H. Al Jabri, Y. Hirota, Y. Uchida, S. Tanaka, M. Miyamoto, Y. Oumi, C.Y. Kong, N. Nishiyama, Dehydrogenation of propane over high silica *BEA type gallosilicate (Ga-Beta), Catalysis Science & Technology, 9 (2019) 6234-6239.

[13] N.M. Phadke, E. Mansoor, M. Bondil, M. Head-Gordon, A.T. Bell, Mechanism and Kinetics of Propane Dehydrogenation and Cracking over Ga/H-MFI Prepared via Vapor-Phase Exchange of H-MFI with $GaCl_3$, Journal of the American Chemical Society, 141 (2018) 1614-1627.

[14] K.C. Szeto, A. Gallo, S. Hernández-Morejudo, U. Olsbye, A. De Mallmann, F. Lefebvre, R.M. Gauvin, L. Delevoye, S.L. Scott, M. Taoufik, Selective Grafting of $Ga(i\text{-}Bu)_3$ on the Silanols of Mesoporous H-ZSM-5 by Surface Organometallic Chemistry, The Journal of Physical Chemistry C, 119 (2015) 26611-26619.

[15] K. Searles, G. Siddiqi, O.V. Safonova, C. Copéret, Silica-supported isolated gallium sites as highly active, selective and stable propane dehydrogenation catalysts, Chemical Science, 8 (2017) 2661-2666.

[16] J.A. Biscardi, E. Iglesia, Structure and function of metal cations in light alkane reactions catalyzed by modified H-ZSM5, Catalysis Today, 31 (1996) 207-231.

[17] K.M. Dooley, G.L. Price, V.I. Kanazirev, V.I. Hart, Gallium-loaded zeolites for light paraffin aromatization: Evidence for exchanged gallium cation active centers, Catalysis Today, 31 (1996) 305-315.

[18] N. Rane, A.R. Overweg, V.B. Kazansky, R.A. van Santen, E.J.M. Hensen, Characterization and reactivity of Ga^+ and GaO^+ cations in zeolite ZSM-5, Journal of Catalysis, 239 (2006) 478-485.

[19] E.J.M. Hensen, E.A. Pidko, N. Rane, R.A. van Santen, Water-promoted hydrocarbon activation catalyzed by binuclear gallium sites in ZSM-5 zeolite, Angewandte Chemie International Edition, 46 (2007) 7273-7276.

[20] Y.V. Joshi, K.T. Thomson, The roles of gallium hydride and Brønsted acidity in light alkane dehydrogenation mechanisms using Ga-exchanged HZSM-5 catalysts: A DFT pathway analysis, Catalysis Today, 105 (2005) 106-121.

[21] Y. Yuan, C. Brady, R.F. Lobo, B. Xu, Understanding the Correlation between Ga Speciation and Propane Dehydrogenation Activity on Ga/H-ZSM-5 Catalysts, ACS Catalysis, (2021) 10647-10659.

[22] E. Mansoor, M. Head-Gordon, A.T. Bell, Computational Modeling of the Nature and Role of Ga Species for Light Alkane Dehydrogenation Catalyzed by Ga/H-MFI, ACS Catalysis, 8 (2018) 6146-6162.

[23] N.M. Phadke, E. Mansoor, M. Head-Gordon, A.T. Bell, Mechanism and Kinetics of Light Alkane Dehydrogenation and Cracking over Isolated Ga Species in Ga/H-MFI, ACS Catalysis, 11 (2021) 2062-2075.

[24] E.A. Pidko, V.B. Kazansky, E.J.M. Hensen, R.A. van Santen, A comprehensive density functional theory study of ethane dehydrogenation over reduced extra-framework gallium species in ZSM-5 zeolite, Journal of Catalysis, 240 (2006) 73-84.

[25] A. Bhan, W. Nicholas Delgass, Propane Aromatization over HZSM-5 and Ga/HZSM-5 Catalysts, Catalysis Reviews, 50 (2008) 19-151.

[26] D.B. Lukyanov, N.S. Gnep, M.R. Guisnet, Kinetic modeling of propane aromatization reaction over HZSM-5 and GaHZSM-5, Industrial & Engineering Chemistry Research, 34 (1995) 516-523.

[27] M. Guisnet, N.S. Gnep, Aromatization of propane over GaHMFI catalysts. Reaction scheme, nature of the dehydrogenating species and mode of coke formation, Catalysis Today, 31 (1996) 275-292.

[28] P. Andy, M.E. Davis, Dehydrogenation of Propane over Platinum Containing CIT-6, Industrial & Engineering Chemistry Research, 43 (2004) 2922-2928.

[29] S.-W. Choi, W.-G. Kim, J.-S. So, J.S. Moore, Y. Liu, R.S. Dixit, J.G. Pendergast, C. Sievers, D.S. Sholl, S. Nair, C.W. Jones, Propane dehydrogenation catalyzed by gallosilicate MFI zeolites with perturbed acidity, Journal of Catalysis, 345 (2017) 113-123.

[30] A.A.C. E.L. Jablonski, O.A. Scelza*, S.R. de Miguel, Effect of Ga addition to $PtAl_2O_3$ on the activity, selectivityand deactivation in the propane dehydrogenation, Applied Catalysis A: General 183 (1999) 189-198.

[31] P. Andy, M. Davis, Dehydrogenation of propane over platinum containing CIT-6, Industrial & Engineering Chemistry Research, 43 (2004) 2922-2928.

[32] J. Zhu, M.-L. Yang, Y. Yu, Y.-A. Zhu, Z.-J. Sui, X.-G. Zhou, A. Holmen, D. Chen, Size-dependent reaction mechanism and kinetics for propane dehydrogenation over Pt catalysts, ACS Catalysis, 5 (2015) 6310-6319.

[33] K.G. Azzam, G. Jacobs, W.D. Shafer, B.H. Davis, Dehydrogenation of propane over Pt/KL catalyst Investigating the role of L-zeolite structure on catalyst performance using isotope labeling, Applied Catalysis A-General, 390 (2010) 264-270.

[34] X. Zhao, S. Villar-Rodil, A.J. Fletcher, K.M. Thomas, Kinetic Isotope Effect for H_2 and D_2 Quantum Molecular Sieving in Adsorption/Desorption on Porous Carbon Materials, The Journal of Physical Chemistry B, 110 (2006) 9947-9955.

[35] J.A. Biscardi, E. Iglesia, Structure and function of metal cations in light alkane reactions catalyzed by modified H-ZSM5, Catalysis Today, 31 (1996) 207-231.

[36] B. Xu, B. Zheng, W. Hua, Y. Yue, Z. Gao, Support effect in dehydrogenation of propane in the presence of CO_2 over supported gallium oxide catalysts, Journal of Catalysis, 239 (2006) 470-477.

[37] P. Castro-Fernández, D. Mance, C. Liu, I.B. Moroz, P.M. Abdala, E.A. Pidko, C. Copéret, A. Fedorov, C.R. Müller, Propane Dehydrogenation on Ga_2O_3-Based Catalysts: Contrasting Performance with Coordination Environment and Acidity of Surface Sites, ACS Catalysis, 11 (2021) 907-924.

[38] S.L. Schroeder, M. Gottfried, Temperature-programmed desorption (TPD) thermal desorption spectroscopy (TDS), Advanced Lab Course Physical Chemistry, FU Berlin, June 2002, (2002).

[39] P.A. Redhead, Thermal desorption of gases, Vacuum, 12 (1962) 203-211.

[40] M. Guisnet, N. Gnep, Aromatization of propane over GaHMFI catalysts. Reaction scheme, nature of the dehydrogenating species and mode of coke formation, Catalysis Today, 31 (1996) 275-292.

[41] C.T.W. Chu, C.D. Chang, Isomorphous substitution in zeolite frameworks. 1. Acidity of surface hydroxyls in [B]-, [Fe]-, [Ga]-, and [Al]-ZSM-5, The Journal of Physical Chemistry, 89 (1985) 1569-1571.

[42] C. Otero Areán, G. Turnes Palomino, F. Geobaldo, A. Zecchina, Characterization of gallosilicate MFI-type zeolites by IR spectroscopy of adsorbed probe molecules, The Journal of Physical Chemistry, 100 (1996) 6678-6690.

[43] A.Y. Khodakov, L. Kustov, T. Bondarenko, A. Dergachev, V. Kazansky, K.M. Minachev, G. Borbely, H. Beyer, Investigation of the different states of gallium in crystalline gallosilicates with pentasil structure and their role in propane aromatization, Zeolites, 10 (1990) 603-607.

[44] G. Giannetto, A. Montes, N. Gnep, A. Florentino, P. Cartraud, M. Guisnet, Conversion of light alkanes into aromatic hydrocarbons. VII. Aromatization of propane on gallosilicates: effect of calcination in dry air, Journal of Catalysis, 145 (1994) 86-95.

[45] V. Choudhary, C. Sivadinarayana, A. Kinage, P. Devadas, M. Guisnet, H-Gallosilicate (MFI) propane aromatization catalyst Influence of calcination temperature on acidity, activity and deactivation due to coking, Applied Catalysis A: General, 136 (1996) 125-142.

[46] V. Choudhary, P. Devadas, A. Kinage, C. Sivadinarayana, M. Guisnet, Acidity, catalytic activity, and deactivation of H-gallosilicate (MFI) in propane aromatization: Influence of hydrothermal pretreatments, Journal of Catalysis, 158 (1996) 537-550.

[47] Y. Nagai, K. Dohmae, Y. Ikeda, N. Takagi, T. Tanabe, N. Hara, G. Guilera, S. Pascarelli, M.A. Newton, O. Kuno, In situ redispersion of platinum autoexhaust catalysts: an on-line approach to increasing catalyst lifetimes?, Angewandte Chemie International Edition, 47 (2008) 9303-9306.

[48] C.H. Bartholomew, Mechanisms of catalyst deactivation, Applied Catalysis A: General, 212 (2001) 17-60.

[49] E. Jablonski, A. Castro, O. Scelza, S. De Miguel, Effect of Ga addition to Pt/Al_2O_3 on the activity, selectivity and deactivation in the propane dehydrogenation, Applied Catalysis A: General, 183 (1999) 189-198.

[50] J.J. Sattler, I.D. Gonzalez-Jimenez, L. Luo, B.A. Stears, A. Malek, D.G. Barton, B.A. Kilos, M.P. Kaminsky, T.W. Verhoeven, E.J. Koers, Platinum-promoted Ga/Al_2O_3 as highly active, selective, and stable catalyst for the dehydrogenation of propane, Angewandte Chemie International Edition, 126 (2014) 9405-9410.

[51] K. Searles, K.W. Chan, J.A. Mendes Burak, D. Zemlyanov, O. Safonova, C. Copéret, Highly productive propane dehydrogenation catalyst using silica-supported Ga-Pt nanoparticles generated from single-sites, Journal of the American Chemical Society, 140 (2018) 11674-11679.

Chapter 4

4. Conversion of ethanol to 1,3-butadiene over Zn-BEA

4.1 Abstract

To gain an in-depth understanding of the catalytic properties of Zn-BEA and explore the effect of incorporating Y for the production of 1,3-BD, the conversion of ethanol to 1,3-BD was studied over Zn-BEA and Y/Zn-BEA. Zn-BEA was highly active and selective for ethanol dehydrogenation but not for the subsequent C-C bond formation reaction. 83% selectivity towards AcH was achieved at 26% ethanol conversion on Zn-BEA. The detailed reaction pathway for 1,3-BD production involves ethanol dehydrogenation, Aldol condensation of AcH, 3-hydroxybutanal dehydration, crotonaldehyde reduction and crytol alcohol dehydration. The reduction of crotonaldehyde was found to limit the 1,3-BD production on Zn-BEA, leading to an accumulation of AcH and a low yield of 1,3-BD (~1.2%). With the addition of Y, 1,3-BD productivity was significantly improved from 2.8 to 18 $mmol \cdot g^{-1}_{cat} \cdot h^{-1}$ with a selectivity of 40% at 20% ethanol conversion.

4.2 Introduction

Zincosilicates have attracted increasing attention due to their unique properties compared to conventional zeolites and many studies have focused on their applications in heterogeneous catalysis.[1-7] With growing environmental concerns and the need to reduce carbon emissions, the production of high-value chemicals from renewable resources has attracted intensive attention in recent decades. Biomass resources are promising alternatives to fossil resources. The availability of bioethanol has motivated the research for efficient methods to upgrade ethanol to valuable products such as ethene, 1,3-BD, *n*-butanol, and others.[8, 9]

1,3-BD is a very useful raw material for the production of tires, toughened plastics, and many other products.[10] Currently, 1,3-BD is mainly produced from the isolation of naphtha steam cracker fractions from paraffinic hydrocarbons mixtures, which is followed by complicated distillation steps, in the manufacture of ethene and its higher homologues.[11] 1,3-BD was reported to be formed from ethanol via C-C bond formation in the Lebedev process at the beginning of the 19th century.[12] The catalyst was a silicon and magnesium oxide with small amounts of other oxides present as promoters, which exhibited both dehydrating and dehydrogenating activities. It has been reported that transition metals like Cu, Zn, and Ag are active for ethanol dehydrogenation; and rare-earth metals like Y, La, Ce, Pr, and Nd are active for C-C formation to produce 1,3-BD precursors.[13]

In recent years, multifunctional catalysts combining both transition metals and rare-earth metals have been explored for the conversion of ethanol to 1,3-BD.[13-18] In particular, Zn-DeAlBEA and Y-DeAlBEA were prepared by the dealumination of H-BEA and subsequent aqueous impregnation.[13, 19] Zn-DeAlBEA was found to be highly active for the dehydrogenation of ethanol to AcH and Y-DeAlBEA for the subsequent 1,3-BD formation. The highest 1,3-BD productivity has been reported to be 66.6 mmol·g^{-1}·h^{-1} with a 1,3-BD selectivity of 52% over 0.15Zn-0.225Y-DeAlBEA (Zn/Al=0.15, Y/Al=0.225) at 673 K.[19] Nevertheless, Li *et al.* reported a 2Zn-8Y/BEA (2 wt.%Zn and 8 wt.% Y) catalyst, which was prepared by mixing the dealuminated zeolite with metal nitrates followed by finely grounding and calcination, having a 1,3-BD productivity of 43.1 mmol·g^{-1}·h^{-1} with 63% selectivity.[16, 17] The preparation methods had a great influence on the catalytic performance of Zn- and Y-based zeolite catalysts. To the best of our knowledge, the application of Zn-BEA on ethanol conversion has not yet been reported. The current understanding of reaction mechanism coming from fragmentary evidence gathered by different research groups gives different possible reaction pathways, for example, the Prins condensation route and Aldol condensation route.[18] Fully elucidating the

mechanism will not only enable the rational design of catalysts with tailored performances but also assist in kinetic modeling.

In this work, Zn-BEA is chosen as the catalyst for one-step conversion of ethanol to 1,3-BD due to its high activity in dehydrogenation reaction from our previous study, which is the first step in ethanol conversion to 1,3-BD. Its few BAS can also play an important role in reducing severe coking side reactions. Further study on the reaction pathway provided clues to modify the catalyst to accelerate the RDS and obtain higher 1,3-BD productivity. Therefore, Y/Zn-BEA was applied and 1,3-BD productivity and selectivity were significantly improved.

4.3 Experimental

The catalysts were tested in a fixed bed plug flow reactor, consisting of a quartz glass tube with 4 mm inner diameter. In a typical experiment, 10 mg catalyst with particle size between 180-300 µm mixed with SiC (250-500 µm) were loaded in the middle of the quartz tube between two quartz wool plugs. Prior to the reaction, the catalyst was activated at 823 K (15 $K \cdot min^{-1}$) in synthetic air for 1 h and cooled with flowing N_2 for 0.5 h to the reaction temperature. The reaction was carried out at 543-633 K and 1 bar total pressure but with varying ethanol partial pressures using N_2 as a carrier gas. The performance of different catalysts was all compared with their catalytic activity at 0.5 h TOS due to the catalyst deactivation during the reaction. The products were detected with an online Agilent 6890 series GC equipped with an HP-PLOT/Q column (30 m × 0.320 mm) and a FID detector. The conversion, yield and selectivity are calculated as:

$$Conversion\ (\%) = 100\% \times \frac{n_{Ethanol} - n_{unreacted,\mathrm{Ethanol}}}{n_{Ethanol}}$$

$$Yield_i(\%) = 100\% \times \frac{n_{i,\ formed}}{n_{i,\ theoretically\ from\ ethanol}}$$

Yield of others (%)= Conversion (%) -Yield of (AcH + ethene + DEE + 1,3-BD) (%)

$$Selectivity_i(\%) = 100\% \times \frac{Yield_i}{Conversion_i}$$

4.4 Results and discussion

4.4.1 Catalytic performance of different catalysts

SiO_2, H-BEA-75 and γ-Al_2O_3 were tested for ethanol conversion to compare with zincosilicate based catalysts in Figure 4.1. SiO_2 showed no activity as it has no catalytically active acid sites.

With BAS as the main active sites, H-BEA-75 produced ethene and diethyl ether (DEE) instead of AcH and no 1,3-BD was observed. The yield of ethene was much higher than that of DEE (39% vs 16%), indicating a domination of intramolecular dehydration on H-BEA-75. BAS could also catalyze secondary reactions including cracking, oligomerization and aromatization,[20, 21] therefore, H-BEA-75 also gave the highest yield to these side products (as shown as the yield of "Others" in Figure 4.1). For γ-Al_2O_3, which contains mainly LAS, no dehydrogenation but mostly dehydration products were formed. However, the DEE yield was much higher than the ethene yield, indicating that intermolecular dehydration of ethanol was more significant on γ-Al_2O_3.

Ga/BEA-3.2 primarily catalyzed intermolecular dehydration of ethanol with DEE as the main product. It was more active for ethanol dehydrogenation compared to H-BEA-75 and γ-Al_2O_3 with the formation of a small amount of AcH. In contrast, Zn-BEA and Ga/Zn-BEA-1.4 were mainly active for the dehydrogenation reaction. The selectivity to AcH was 83% and 87% at corresponding ethanol conversions of 26% and 22%, respectively. The yield of ethene and DEE were 0.3% and 1.4% for Zn-BEA and 0.3% and 1.8% for Ga/Zn-BEA-1.4. The less favorable dehydration reactions can be attributed to few BAS on Zn-BEA and Ga/Zn-BEA-1.4. Additionally, Zn sites have been reported to be very active for ethanol dehydrogenation.[16, 17, 19] Using Zn-MFI also led to an increased AcH selectivity of 89%. Its smaller pore size could reduce the formation of larger secondary products from AcH condensation and oligomerization, and lead to higher AcH selectivity and less catalyst deactivation. However, the ethanol conversion was only 12%, which could be explained by the lower Zn content compared with Zn-BEA.

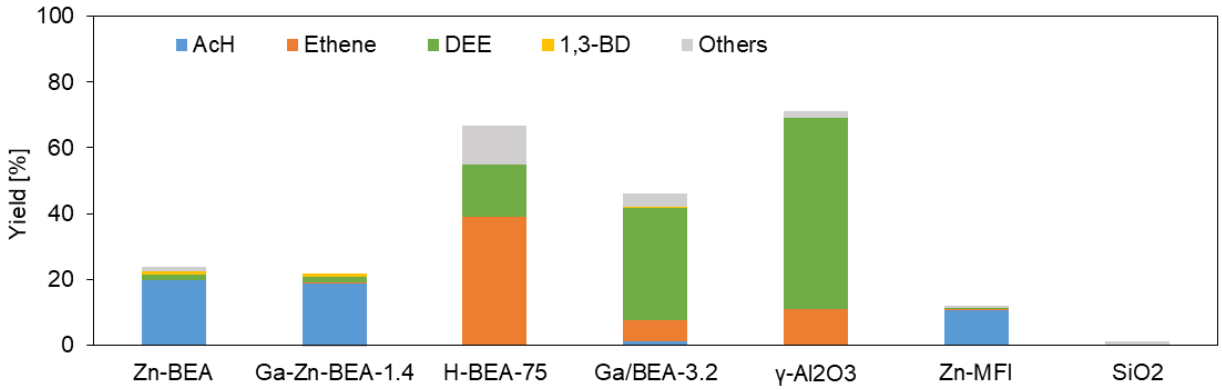

Figure 4.1 The yield of products from ethanol conversion on different catalysts. Reaction condition: 1 bar, 10 mg catalyst, total flowrate 32 ml·min^{-1}, 60 mbar ethanol, 573 K.

1,3-BD was formed with 1.0% and 1.2% yield on Ga/Zn-BEA-1.4 and Zn-BEA with a productivity of around 2.8 mmol·g^{-1}·h^{-1}. All other catalysts gave a 1,3-BD yield that was lower

than 0.1%. Therefore, Zn-BEA can catalyze both dehydrogenation and C-C formation reactions even though the 1,3-BD formation rate was one order of magnitude lower than that of AcH formation. The addition of Ga sites did not improve the production of both AcH and 1,3-BD.

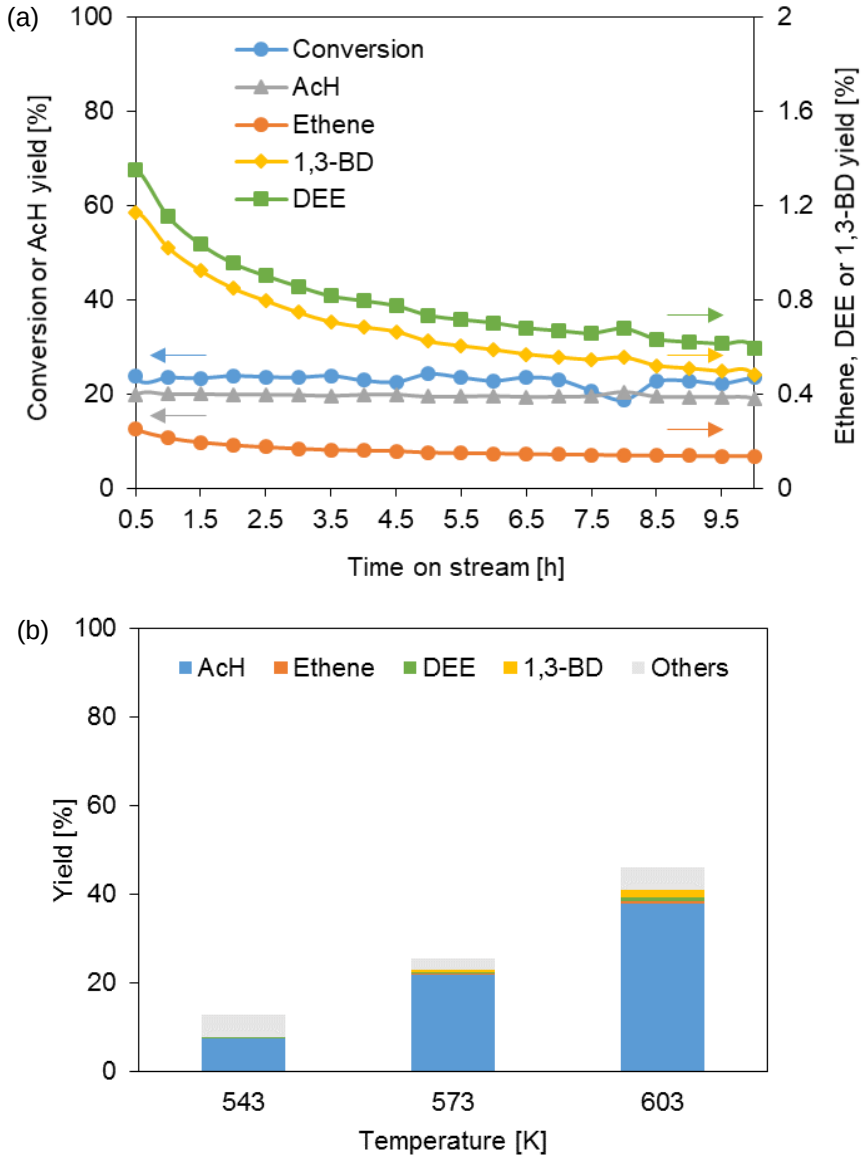

Figure 4.2 (a) The conversion and product yield as a function of TOS on Zn-BEA at 573 K; (b) The effect of temperature on ethanol conversion over Zn-BEA. Reaction condition: 1 bar, 10 mg catalyst, total flowrate 32 ml·min^{-1}, 60 mbar ethanol.

The catalytic behavior of Zn-BEA with TOS was monitored in Figure 4.2a. The yield of 1,3-BD, DEE and ethene decreased significantly from 1.2%, 1.4% and 0.3% to 0.5%, 0.6% and 0.1% from 0.5 h to 10 h TOS. However, the changes in ethanol conversion and AcH yield were negligible. Therefore, the active sites for ethanol dehydrogenation were stable during the reaction, while the sites for ethanol dehydration and 1,3-BD formation deactivated fast, which can be caused by more favorable oligomerization and aromatization side reactions from alkene and AcH on these sites. We attributed the BAS to be responsible for the dehydration and C-C

bond formation reactions and Lewis acidic Zn sites for the dehydrogenation reaction.[19] The same change of product yield with TOS was also observed with Ga/Zn-BEA-1.4 in Figure S4.1. The addition of Ga sites did not change the deactivation behavior of the catalyst. However, it has been reported that the yield of AcH and 1,3-BD both increased with TOS on Zn-deAlBEA and isolated Zn sites were proposed to be the active sites for the formation of AcH and 1,3-BD on Zn-deAlBEA.[19] We, therefore, hypothesize that Zn-deAlBEA and our Zn-BEA should have different reaction mechanisms. The variation of the reaction temperature was also studied on Zn-BEA (Figure 4.2b). When the temperature was low, ethene, DEE and 1,3-BD were not observed. With the increase of temperature, the conversion and all product yield increased, nevertheless, AcH still remained to be the main product and 1,3-BD yield was only 1.5%. The change of temperature is not effective to improve 1,3-BD production.

The effect of ethanol partial pressure on the dehydrogenation rate is illustrated in Figure 4.3. All the data were collected at 0.5 h TOS. The apparent reaction order in ethanol partial pressure decreased from 0.7 to 0.5 when ethanol partial pressure increased from 4 to 56 mbar. Furthermore, the activation energy of ethanol dehydrogenation determined from the Arrhenius plot was 57 ± 2 kJ·mol^{-1} at 4 mbar in the temperature range of 543 to 633 K. The dehydrogenation step is the fastest step during the conversion of ethanol, and the transformation of AcH to 1,3-BD limited the 1,3-BD production.

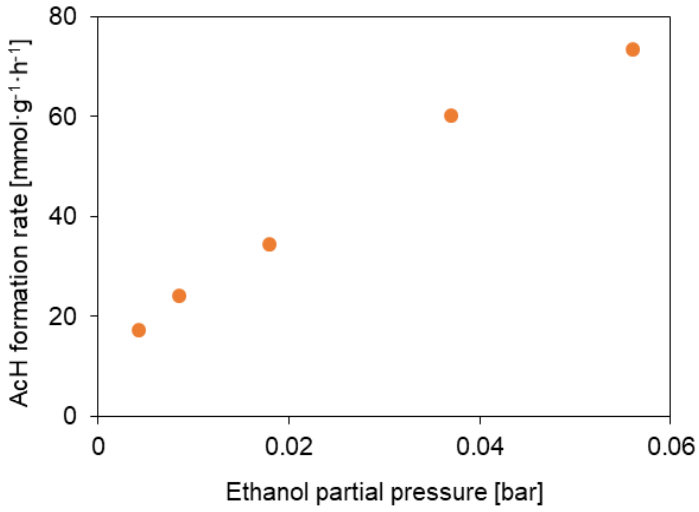

Figure 4.3 Effect of Ethanol partial pressure on the rate of AcH formation. Reaction condition: 1 bar, 10 mg Zn-BEA, total flowrate 30 mL·min^{-1}, 573 K.

4.4.2 Reaction pathways for 1,3-butadiene formation

The investigation of the RDS and reaction mechanism is helpful to adjust the reaction condition and modify the catalyst to improve 1,3-BD production. Therefore, the two widely discussed Prins reaction and Aldol condensation pathways were investigated.

In the Prins reaction pathway, an excess of ethene can favor the formation of unsaturated alcohol that is the precursor of 1,3-BD.[22] With Zn-BEA, the yield of ethene was below 0.5% and it might limit the Prins reaction between ethene and AcH to form C_4 products. Thus ethene was co-fed with ethanol as the reactants and the results are shown in Figure 4.4. We did not observe an increase of 1,3-BD yield on Zn-BEA or Ga/Zn-BEA-1.4. AcH remained to be the main product and more side products with longer carbon chains were observed due to the high reactivity of ethene via dimerization and further aromatization reactions (as shown as the yield of "Others"). The direct product from Prins reaction between ethene and AcH (*i.e.*, 3-buten-2-ol) was not detected via GC-FID analysis. We, therefore, concluded that Ga or Zn sites were not active for the Prins reaction pathway.

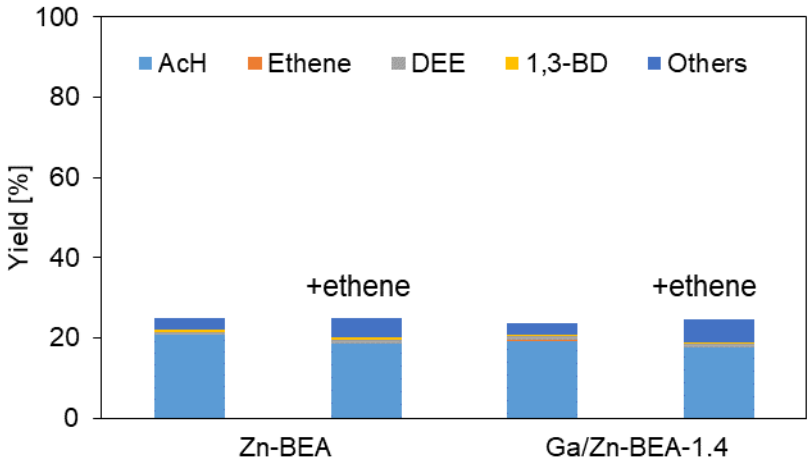

Figure 4.4 The effect of co-feed ethene with ethanol on the reaction on Zn-BEA and Ga/Zn-BEA-1.4. Reaction condition: 1 bar, 10 mg catalyst, Ethanol/ethene=4/1, 30 mL·min^{-1}, 60 mbar Ethanol, 573 K. The yields were calculated based on only ethanol conversion.

Apart from Zn-BEA and Ga/Zn-BEA-1.4, H-BEA-75 and H-BEA-5 were also tested for the reaction between ethene and AcH, since BAS can be more active for Prins reaction.[23] However, 3-buten-2-ol was not detected and very low conversions were observed for both catalysts at 573 K. In the temperature range of 323 K to 663 K, the conversion was always below 4% and propene was the only main product formed from the cracking of butene from ethene dimerization on H-BEA-75 (Figure S4.4).[24, 25] When using H-BEA-5 with high BAS concentration and stronger acid sites, almost no conversion of ethene and AcH (both <0.1%)

was observed at 0.5 h TOS at 573 K. It is possible that the catalyst already deactivated within 0.5 h. We took the catalysts out of the reactor after 5 min TOS, and expectedly H-BEA-5 turned dark. The concentration of BAS and LAS decreased from 1.5 and 1.2 to 0.9 and 0.5 mmol·g^{-1} respectively as measured by pyridine adsorbed IR spectroscopy (Table S4.1). H-BEA-75 turned dark after 5 min TOS as well. Therefore Brønsted acidic catalysts like H-BEA are not suitable for Prins reaction between AcH and ethene due to their fast deactivation.

Meanwhile, a small amount of crotonaldehyde and crotyl alcohol which are typical products from the Aldol condensation pathway were observed over all catalysts tested (*i.e.*, Zn-BEA, Ga/Zn-BEA-1.4, H-BEA-75, H-BEA-5). The Aldol condensation pathway was more favorable than the Prins reaction pathway under the same conditions, suggesting that 1,3-BD formed over Zn-BEA should be from the Aldol condensation pathway. With a co-feed of AcH (ethanol/AcH=3.5/1), 1,3-BD productivity increased to 3.4 mmol·g^{-1}·h^{-1} on Zn-BEA. The improvement was not significant as AcH was already formed (Scheme 4.1a) and accumulated during the reaction of ethanol on Zn-BEA. Therefore the other elementary steps of the Aldol condensation pathway, *i.e.*, Aldol condensation of two AcH (Scheme 4.1 b), conversion of crotonaldehyde to crotyl alcohol (Scheme 4.1 d), and crotyl alcohol dehydration (Scheme 4.1 e) were investigated.

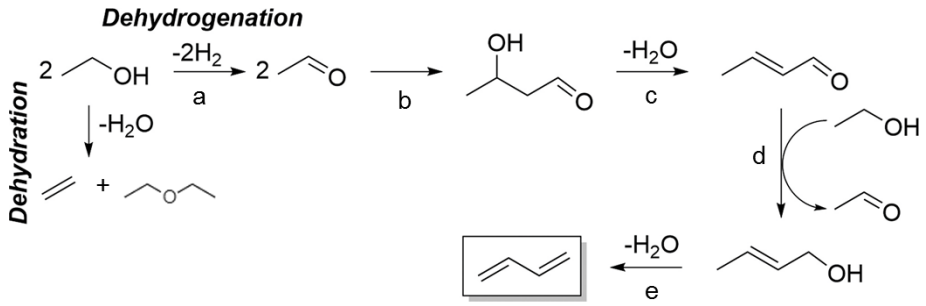

Scheme 4.1 The Aldol condensation pathway and the competing path to ethene and DEE. Adapted with permission from ref. [26]. Copyright (2020) American Chemical Society.

With AcH as the reactant, crotonaldehyde was the main product (84% selectivity at 15% conversion) on Zn-BEA at 0.5 h TOS at 573 K (Figure 4.5). 1,3-BD selectivity was below 0.1% and other byproducts were propene, crotyl alcohol (both yield lower than 0.1%) and some unknown heavier products. The conversion decreased to 7% and the selectivity remained almost constant within 5 h TOS. 3-hydroxybutanal, the direct product from Aldol condensation of two AcH, was reported to be unstable and dehydrated readily to crotonaldehyde once formed.[14, 27, 28] Crotonaldehyde was also the only product observed during Aldol condensation of AcH on TiO_2, hydroxyapatite, and MgO.[29] Nevertheless, Gao *et al.* studied the one-step process

using the pulse reaction technique with a mass spectrometry over MgO-SiO_2 catalyst, and sequential formation of AcH, 3-hydroxybutanal, crotonaldehyde and 1,3-BD were all observed.[30]

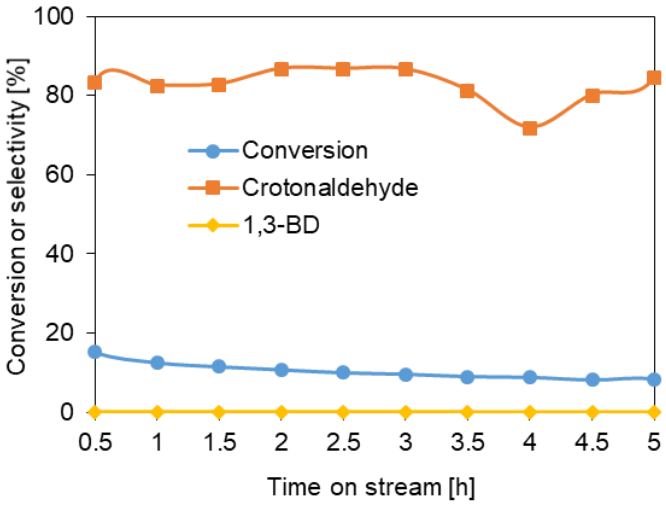

Figure 4.5 The conversion AcH on Zn-BEA with TOS. Reaction condition: 1 bar, 10 mg catalyst, 30 mL·min^{-1}, 573 K, 13 mbar AcH.

Subsequently, the dehydration of crotyl alcohol was also found to occur easily. Around 85% 1,3-BD selectivity was achieved at 94% conversion on Zn-BEA at 573 K at 0.5 h TOS (Figure 4.6). The other byproducts included propene, AcH, butenes, crotonaldehyde and some heavier products. It is in good agreement with the literature that the crotyl alcohol dehydration is highly thermodynamically favorable and occurs immediately after formation on most "ethanol to 1,3-BD" catalysts.[18] Within 5 h TOS, the conversion kept stable and the selectivity decreased slightly, indicating the good stability of Zn-BEA in this step.

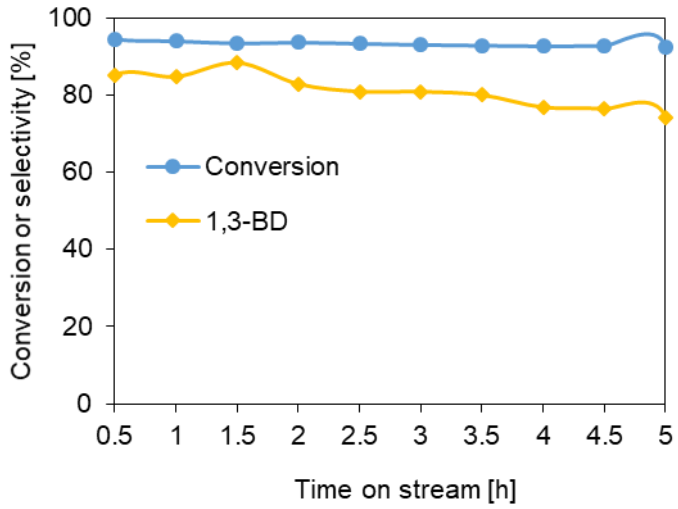

Figure 4.6 The conversion of crotyl alcohol on Zn-BEA with TOS. Reaction condition: 1 bar, 10 mg catalyst, total flowrate 30 mL·min^{-1}, 573 K, 7 mbar crotyl alcohol.

Finally, the last step in the route (*i.e.*, Scheme 4.1d) was studied. Ethanol was reported to be a better hydrogen donor than H_2 for the MPVO reaction of crotonaldehyde to crotyl alcohol.[11, 27, 31, 32] With the co-feed of crotonaldehyde and ethanol, the carbon conversion was 15% at 0.5 h TOS with low selectivity to crotyl alcohol (7%) and 1,3-BD (12%) (Figure 4.7, detailed calculation in Appendix 4.6). AcH was the main product with 27% selectivity and ethene, propene, butenes, and DEE all had selectivity below 0.5%. A significant number of heavier side products were formed (~53% selectivity). 1,3-BD productivity of 4.5 mmol·g^{-1}·h^{-1} was achieved. Compared with the other steps, this step is the most inefficient and unselective to target products. As ethanol itself can produce 1,3-BD, isopropanol which is more reactive in the MPVO reaction was used to react with crotonaldehyde to further prove the MPVO route on Zn-BEA. As expected, the 1,3-BD productivity increased to 26.8 mmol·g^{-1}·h^{-1}. In summary, the reaction between crotonaldehyde and ethanol is the RDS of the Aldol condensation pathway on Zn-BEA and it has to be enhanced to obtain higher 1,3-BD productivity.

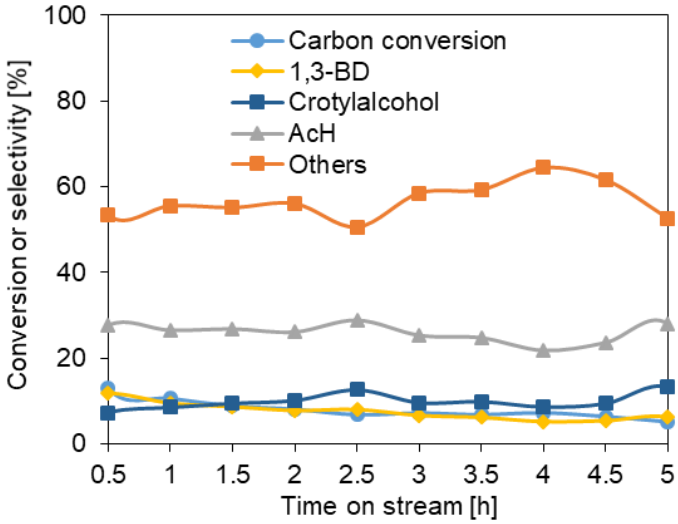

Figure 4.7 The conversion of crotonaldehyde and ethanol on Zn-BEA with TOS. Reaction condition: 1 bar, 10 mg catalyst, total flowrate 30 mL·min^{-1}, 573 K, 40 mbar ethanol, 20 mbar crotonaldehyde. "Others" refers to the products excluding 1,3-BD, crotyl alcohol and AcH.

4.4.3 1,3-Butadiene production with Y/Zn-BEA

Y sites have been reported to be highly efficient for C-C bond formation,[19] and Y/Zn-BEA with different Y loadings were prepared and used for this reaction. In Figure 4.8, the rate of ethanol conversion and product formation all reached a plateau until Y content is 2.2 wt.%. Except for the 1,3-BD formation rate, the other rates all decreased with Y content. The rate of 1,3-BD formation increased until a plateau of ~18 mmol·g^{-1}·h^{-1}. And it is one order of magnitude higher than that on parent Zn-BEA. Correspondingly, the 1,3-BD selectivity was

~40% at a conversion of ~20% on Y/Zn-BEA at the plateau. At the same time, the AcH formation rate decreased with Y content as more AcH was consumed to form C_4 products with more Y sites. However, AcH still remained to be the main product, suggesting that the formation of C_4 products still limited the production of 1,3-BD. The formation rates of ethene and DEE also decreased with increasing Y content. Therefore, ethanol dehydration was not catalyzed by Y sites. The addition of Y might cover some BAS which were active for dehydration reaction, and led to the decrease of the formation rates of ethene and DEE.

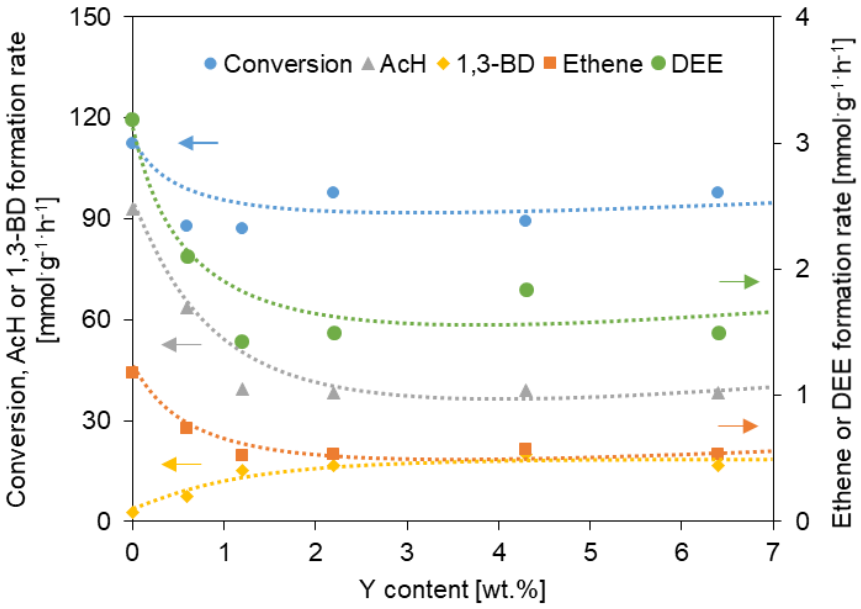

Figure 4.8 Effect of Y content in Y/Zn-BEA on ethanol conversion. Reaction condition: 1 bar, 10 mg catalyst, total flowrate 32 mL·min^{-1}, 573 K, 60 mbar ethanol.

The conversion of ethanol on Y/Zn-BEA-2.2 as a function of TOS is shown in Figure 4.9. The conversion of ethanol decreased with TOS, showing a catalytic deactivation during the reaction. The yield of ethene, DEE and 1,3-BD all decreased with the decrease of ethanol conversion. At the same time, the yield of AcH increased, which should be due to the decreasing consumption of AcH for 1,3-BD production with TOS. It also suggests that the active sites to catalyze ethanol dehydrogenation and C-C coupling reaction are different. Y sites that are active for the C-C bond coupling deactivated fast during the reaction, while Zn sites that are active for ethanol dehydrogenation were more stable during the reaction, which could be seen from the behavior of Zn-BEA with TOS in Figure 4.2a as well. In Figure 4.10, the TOF of 1,3-BD production normalized on Y sites was constant at Y content from 0.6 to 1.2 wt.% and decreased at higher Y content. Therefore we postulated that the active sites were isolated Y sites at low Y content while at higher Y contents, the dispersion and interaction with neighboring acid sites or silanol groups affected the activity of Y sites.

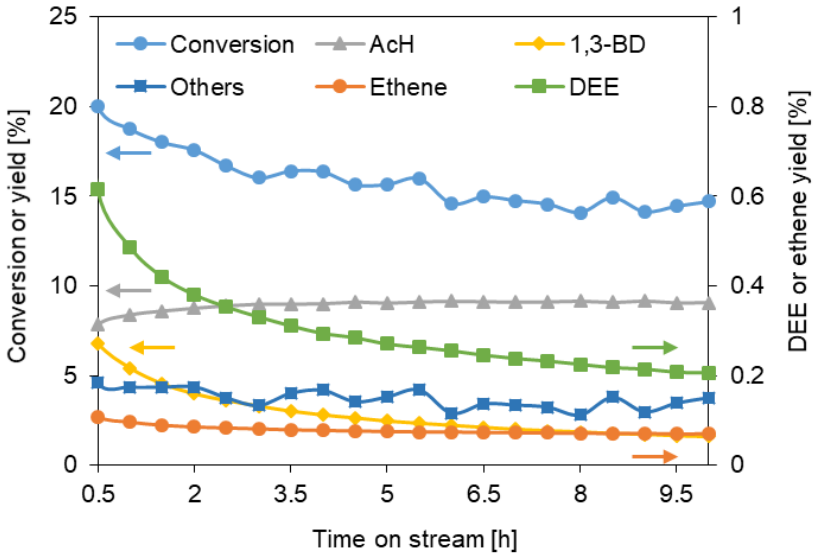

Figure 4.9 The conversion and product yield on Y/Zn-BEA-2.2 with TOS. Reaction condition: 1 bar, 10 mg catalyst, total flowrate 32 mL·min^{-1}, 573 K, 60 mbar ethanol.

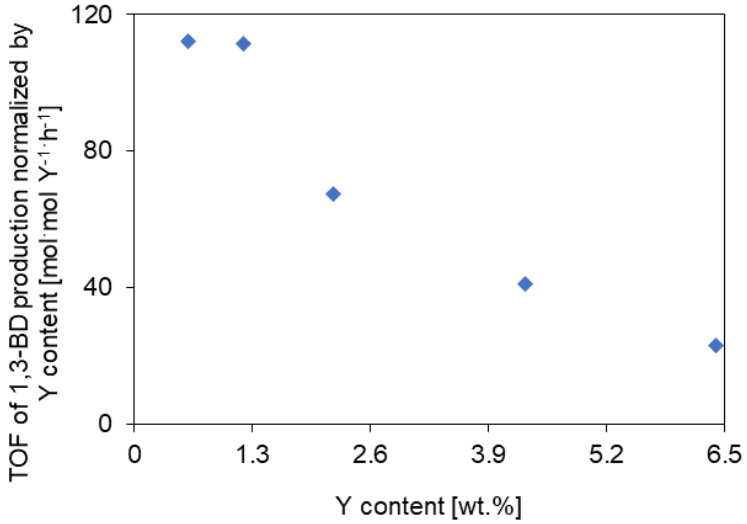

Figure 4.10 The TOF of 1,3-BD production as a function of Y content. Reaction condition: 1 bar, 10 mg catalyst, total flowrate 32 mL·min^{-1}, 573 K, 60 mbar ethanol.

4.5 Conclusion

Zn-BEA was found to be highly active and selective for ethanol dehydrogenation to AcH but not further C-C bond formation, leading to an AcH formation rate of 92.9 $mmol \cdot g^{-1} \cdot h^{-1}$ and a 1,3-BD formation rate of 2.8 $mmol \cdot g^{-1} \cdot h^{-1}$. With further investigation, the formation of 1,3-BD on Zn-BEA was found to proceed via the Aldol condensation pathway rather than the Prins reaction pathway. The three elementary steps involving Aldol condensation of two AcH molecules, crotyl alcohol dehydration and crotonaldehyde reduction via MPVO reaction with ethanol were studied. The former two steps can be catalyzed selectively (above 80% selectivity to 1,3-BD precursors) and efficiently with Zn-BEA, while the reduction of crotonaldehyde with ethanol was found to be the rate limiting step. With the addition of Y via incipient wetness impregnation, the 1,3-BD production rate increased until a plateau was reached with a Y content of 2.2 wt.%. The 1,3-BD productivity was significantly improved to 18 $mmol \cdot g^{-1} \cdot h^{-1}$ at the plateau (~40% selectivity at ~20% conversion of ethanol), which was one order of magnitude higher than that on Zn-BEA.

4.6 Appendix

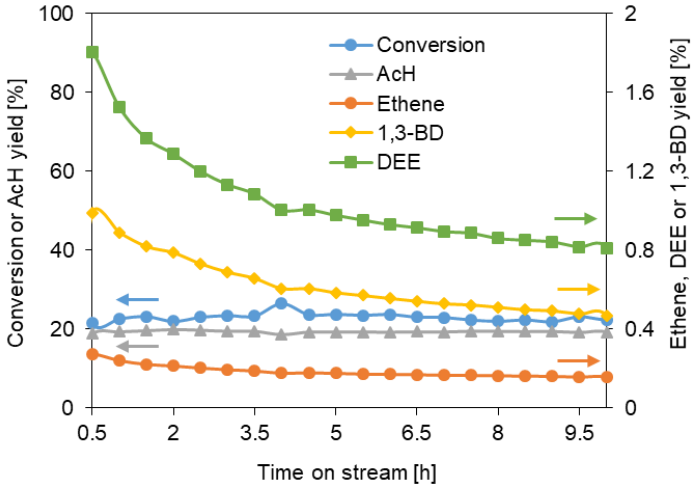

Figure S4.1 Ethanol conversion on Ga/Zn-BEA-1.4. Reaction condition: 1 bar, 10 mg catalyst, total flowrate 32 mL·min^{-1}, 573 K, 60 mbar.

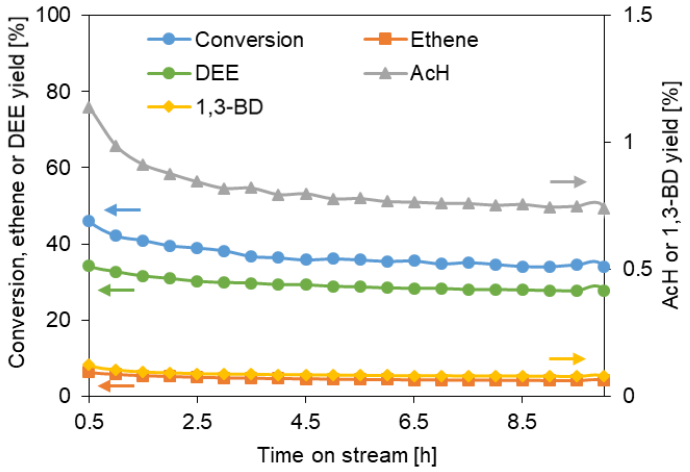

Figure S4.2 Ethanol conversion on Ga/BEA-3.2. Reaction condition: 1 bar, 10 mg catalyst, total flowrate 32 mL·min^{-1}, 573 K, 60 mbar.

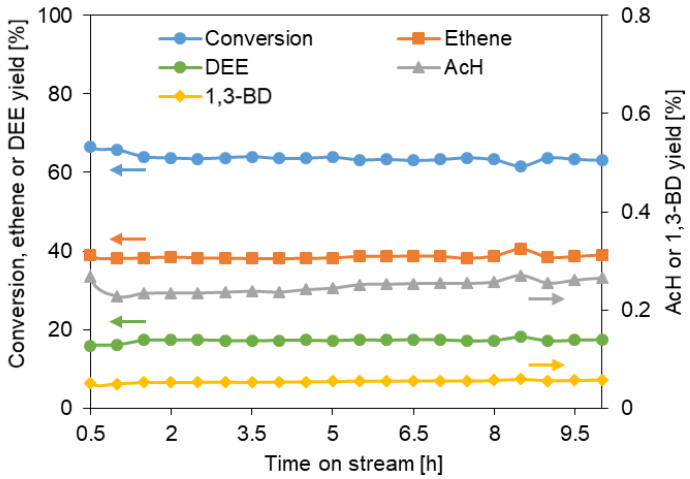

Figure S4.3 Ethanol conversion on H-BEA-75 with TOS. Reaction condition: 1 bar, 10 mg catalyst, total flowrate 32 mL·min^{-1}, 573 K, 60 mbar.

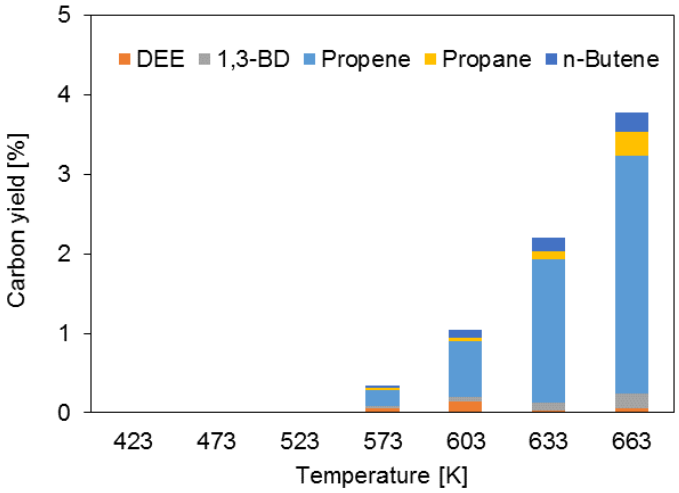

Figure S4.4 Reaction of ethene and AcH on H-BEA-75 at different temperatures. Reaction condition: 1 bar, 20 mg catalyst, ethene/AcH=1/1, total flowrate 15 mL·min^{-1}, 60 mbar ethanol.

When AcH and ethene were used as the reactants (Figure S4.4), the carbon conversion, carbon yield and are calculated as:

$$Carbon\ conversion\ (\%) = 100\% \times \frac{(n_{ethene} + n_{AcH}) - (n_{unreacted\ ethene} + n_{unreacted\ AcH})}{(n_{ethene} + n_{AcH})}$$

$$Carbon\ yield_i(\%) = 100\% \times \frac{n_{i,formed}}{n_{i,\ theoretically\ from\ total\ C_2}}$$

The loss of acid sites on H-BEA-5 after 5 minutes reaction

Table S4.1 Acid site concentration of H-BEA-5 determined from IR of pyridine adsorption

	BAS [mmol·g^{-1}]	LAS [mmol·g^{-1}]
Before reaction	1.50	1.15
After 5 min reaction	0.88	0.49

Reaction condition: H-BEA-5, 573 K, 1 bar, total flowrate 44 mL·min^{-1}, 84 mbar ethene, ethene/AcH=6/1

Calculation of carbon conversion and carbon yield

When ethanol and crotonaldehyde (CA) were used as the reactants (Figure 4.7), the carbon conversion and carbon yield were calculated as:

$$Carbon\ conversion\ (\%) = 100\% \times \frac{(2 \times n_{ethanol} + 4 \times n_{CA}) - (2 \times n_{unreacted\ ethanol} + 4 \times n_{unreacted\ CA})}{2 \times n_{ethanol} + 4 \times n_{CA}}$$

$$Carbon\ yield_i(\%) = 100\% \times \frac{n_{i,formed}}{n_{i,\ theoretically\ from\ ethanol\ and\ CA}}$$

$$Selectivity_i(\%) = 100\% \times \frac{Yield_i}{Conversion_i}$$

4.7 Reference

[1] Y. Sakamoto, H. Zhao, H. Gies, K. Yamamoto, U. Kolb, T. Ikeda, A new microporous 12-ring zincosilicate THK-2 with many terminal silanols characterized by automated electron diffraction tomography, Dalton Transactions, 49 (2020) 12960-12969.

[2] M. Orazov, M.E. Davis, Catalysis by framework zinc in silica-based molecular sieves, Chemical Science, 7 (2016) 2264-2274.

[3] P. Andy, M.E. Davis, Dehydrogenation of Propane over Platinum Containing CIT-6, Industrial & Engineering Chemistry Research, 43 (2004) 2922-2928.

[4] T. Inui, J.-B. Kim, T. Takeguchi, H. Nagata, Selective synthesis of aromatics from propene on platinum-modified zinco-silicate catalysts, Applied Catalysis A: General, 106 (1993) 83-95.

[5] N. Koike, K. Iyoki, S.H. Keoh, W. Chaikittisilp, T. Okubo, Synthesis of New Microporous Zincosilicates with CHA Zeolite Topology as Efficient Platforms for Ion-Exchange of Divalent Cations, Chemistry-A European Journal, 24 (2018) 808-812.

[6] M.A. Deimund, J. Labinger, M.E. Davis, Nickel-Exchanged Zincosilicate Catalysts for the Oligomerization of Propylene, ACS Catalysis, 4 (2014) 4189-4195.

[7] T. Iida, D. Zanchet, K. Ohara, T. Wakihara, Y. Román-Leshkov, Concerted Bimetallic Nanocluster Synthesis and Encapsulation via Induced Zeolite Framework Demetallation for Shape and Substrate Selective Heterogeneous Catalysis, Angewandte Chemie International Edition, 57 (2018) 6454-6458.

[8] A. Duque, C. Álvarez, P. Doménech, P. Manzanares, A.D. Moreno, Advanced Bioethanol Production: From Novel Raw Materials to Integrated Biorefineries, Processes, 9 (2021).

[9] C.N. Hamelinck, G.v. Hooijdonk, A.P.C. Faaij, Ethanol from lignocellulosic biomass: techno-economic performance in short-, middle- and long-term, Biomass and Bioenergy, 28 (2005) 384-410.

[10] Y. Qi, Z. Liu, S. Liu, L. Cui, Q. Dai, J. He, W. Dong, C. Bai, Synthesis of 1,3-Butadiene and Its 2-Substituted Monomers for Synthetic Rubbers, Catalysts, 9 (2019).

[11] C. Angelici, B.M. Weckhuysen, P.C.A. Bruijnincx, Chemocatalytic Conversion of Ethanol into Butadiene and Other Bulk Chemicals, ChemSusChem, 6 (2013) 1595-1614.

[12] S. Lebedev, British Patent 331402, 1929; b) SV Lebedev, British Patent 331482, 1930; c) SV Lebedev, French Patent 665917, 1929; d) SV Lebedev, Russian Journal of General Chemistry, 3 (1933) 698-708.

[13] W. Dai, S. Zhang, Z. Yu, T. Yan, G. Wu, N. Guan, L. Li, Zeolite Structural Confinement Effects Enhance One-Pot Catalytic Conversion of Ethanol to Butadiene, ACS Catalysis, 7 (2017) 3703-3706.

[14] V.L. Sushkevich, I.I. Ivanova, V.V. Ordomsky, E. Taarning, Design of a Metal-Promoted Oxide Catalyst for the Selective Synthesis of Butadiene from Ethanol, ChemSusChem, 7 (2014) 2527-2536.

[15] P.I. Kyriienko, O.V. Larina, S.O. Soloviev, S.M. Orlyk, C. Calers, S. Dzwigaj, Ethanol Conversion into 1,3-Butadiene by the Lebedev Method over MTaSiBEA Zeolites (M=Ag, Cu, Zn), ACS Sustainable Chemistry & Engineering, 5 (2017) 2075-2083.

[16] T. Yan, W. Dai, G. Wu, S. Lang, M. Hunger, N. Guan, L. Li, Mechanistic Insights into One-Step Catalytic Conversion of Ethanol to Butadiene over Bifunctional Zn-Y/Beta Zeolite, ACS Catalysis, 8 (2018) 2760-2773.

[17] T. Yan, L. Yang, W. Dai, C. Wang, G. Wu, N. Guan, M. Hunger, L. Li, On the deactivation mechanism of zeolite catalyst in ethanol to butadiene conversion, Journal of Catalysis, 367 (2018) 7-15.

[18] G. Pomalaza, P.A. Ponton, M. Capron, F. Dumeignil, Ethanol-to-butadiene: the reaction and its catalysts, Catalysis Science & Technology, 10 (2020) 4860-4911.

[19] L. Qi, Y.F. Zhang, M.A. Conrad, C.K. Russell, J. Miller, A.T. Bell, Ethanol Conversion to Butadiene over Isolated Zinc and Yttrium Sites Grafted onto Dealuminated Beta Zeolite, Journal of the American Chemical Society, 142 (2020) 14674-14687.

[20] M. Guisnet, N. Gnep, F. Alario, Aromatization of short chain alkanes on zeolite catalysts, Applied Catalysis A: General, 89 (1992) 1-30.

[21] E.A. Uslamin, H. Saito, N. Kosinov, E. Pidko, Y. Sekine, E.J. Hensen, Aromatization of ethylene over zeolite-based catalysts, Catalysis Science & Technology, 10 (2020) 2774-2785.

[22] I.M. Pastor, M. Yus, The Prins reaction: advances and applications, Current Organic Chemistry, 11 (2007) 925-957.

[23] S.P. Bedenko, K.I. Dement'ev, V.F. Tret'yakov, A.L. Maksimov, The Prins Reaction over Heterogeneous Catalysts (a Review), Petroleum Chemistry, 60 (2020) 723-730.

[24] X. Zhu, S. Liu, Y. Song, L. Xu, Catalytic cracking of C4 alkenes to propene and ethene: Influences of zeolites pore structures and Si/Al_2 ratios, Applied Catalysis A: General, 288 (2005) 134-142.

[25] D.S. Fernandes, C.O. Veloso, C.A. Henriques, Ethylene Conversion into Propylene and Aromatics on HZSM-5: Insights on Reaction Routes and Water Influence, Catalysis Letters, 150 (2020) 738-752.

[26] H.T. Abdulrazzaq, A. Rahmani Chokanlu, B.G. Frederick, T.J. Schwartz, Reaction Kinetics Analysis of Ethanol Dehydrogenation Catalyzed by MgO-SiO_2, ACS Catalysis, 10 (2020) 6318-6331.

[27] W.E. Taifan, T. Bucko, J. Baltrusaitis, Catalytic conversion of ethanol to 1,3-butadiene on MgO: A comprehensive mechanism elucidation using DFT calculations, Journal of Catalysis, 346 (2017) 78-91.

[28] T. De Baerdemaeker, M. Feyen, U. Muller, B. Yilmaz, F.S. Xiao, W.P. Zhang, T. Yokoi, X.H. Bao, H. Gies, D.E. De Vos, Bimetallic Zn and Hf on Silica Catalysts for the Conversion of Ethanol to 1,3-Butadiene, ACS Catalysis, 5 (2015) 3393-3397.

[29] Z.D. Young, S. Hanspal, R.J. Davis, Aldol Condensation of Acetaldehyde over Titania, Hydroxyapatite, and Magnesia, ACS Catalysis, 6 (2016) 3193-3202.

[30] M.X. Gao, Z.Z. Liu, M.H. Zhang, L. Tong, Study on the Mechanism of Butadiene Formation from Ethanol, Catalysis Letters, 144 (2014) 2071-2079.

[31] W.M. Quattlebaum, W.J. Toussaint, J.T. Dunn, Deoxygenation of Certain Aldehydes and Ketones - Preparation of Butadiene and Styrene, Journal of the American Chemical Society, 69 (1947) 593-599.

[32] H.E. Jones, E.E. Stahly, B.B. Corson, Butadiene from Ethanol - Reaction Mechanism, Journal of the American Chemical Society, 71 (1949) 1822-1828.

5. Conclusion

Zincosilicates have a chemical nature of acid sites different from the traditional aluminosilicates. Instead of two BAS generated theoretically to compensate the negative charges from a tetrahedrally incorporated Zn^{2+} in the zeolite framework, few BAS and a significant number of LAS were observed on Zn-BEA. It is promising to use Zn-BEA as supports or catalysts for chemical reactions that can be catalyzed by LAS and avoid the side reactions favored by BAS on traditional aluminosilicate zeolites.

In the first work, Ga^{3+} cations were introduced via incipient wetness impregnation on Zn-BEA. The substitution of Zn by Ga via reduction at elevated temperatures led to the complete leaching of Zn and a series of Ga/BEA zeolites with homotopic active sites for propane dehydrogenation. The propane conversion rate increased first with the concentration of Ga up to 3.2 wt.% and decreased at higher Ga concentration despite a monotonous increase of BAS and LAS with the concentration of Ga^{3+}. A very high propene selectivity at high conversion was obtained on Ga/BEA-3.2 and comparable to the results of benchmark Cr_2O_3/Al_2O_3 catalysts.

The PDH exhibited first-order kinetics with respect to propane and the KIE with C_3H_8 and C_3D_8 implied a RDS of the C-H bond cleavage at low propane pressure (2 mbar). As it increases (up to 100 mbar) the reaction order and the KIE decreased to 0.2 and 0.8, respectively. A high propane coverage was excluded under our experimental boundary conditions with *in situ* measurements. Therefore, a gradual shift of the RDS from C-H bond cleavage at low propane pressures to H_2 desorption at high propane pressure was proposed. This kinetic description and the mechanism are valid for all catalysts investigated showing an activation energy of C-H bond cleavage of 155 ± 8 and H_2 desorption of 123 ± 8 $kJ \cdot mol^{-1}$, respectively. The concentration of reversibly adsorbed and desorbed H_2 scales proportionally with the rate of reaction and the desorption enthalpy agrees well with the activation energy, when the desorption of H_2 is rate determining. The low concentration of these sites could either point that the active sites may be only a very small fraction of available Ga sites or that the adsorption of H_2 is kinetically or thermodynamically limited. The high selectivity and stability of the catalysts warrant further investigations into the nature and properties of the active sites.

In the second work, parent Zn-BEA showed high activity and selectivity to ethanol dehydrogenation to AcH, however, with a very low selectivity (7%) to 1,3-BD. The reaction pathway of 1,3-BD was proved to be via an Aldol condensation pathway involving 5 elementary steps of ethanol dehydrogenation, Aldol condensation of AcH, dehydration of 3-

hydroxybutanal to crotonaldehyde, reduction of crotonaldehyde, and dehydration of crotyl alcohol. The MPVO reduction of crotonaldehyde with ethanol was rate determining. Another reaction pathway via the Prins reaction of ethene and AcH was excluded with no 1,3-BD precursors from this route were observed, and severe catalyst deactivation occurred due to the favorable oligomerization and condensation reactions of ethene and AcH on acid sites in zeolites. With incorporating Y in Zn-BEA, the 1,3-BD productivity and selectivity were greatly improved.

In summary, the findings reported in this thesis provide further insights into the application of zincosilicates as supports and catalysts in heterogeneous catalysis, in particular for propane dehydrogenation and ethanol conversion.